

Abstract

Measurement of (π^- -Ar) and (K^+ -Ar) total hadronic cross sections in the LArIAT experiment

Elena Gramellini

2018

6 Abstract goes here. Limit 750 words.

7 **Measurement of (π^- -Ar) and (K^+ -Ar)**

8 **total hadronic cross sections in the**

9 **LArIAT experiment**

10 A Dissertation
11 Presented to the Faculty of the Graduate School
12 of
13 Yale University
14 in Candidacy for the Degree of
15 Doctor of Philosophy

16 by
17 Elena Gramellini

18 Dissertation Director: Bonnie T. Fleming

19 Date you'll receive your degree

²⁰

Copyright © 2018 by Elena Gramellini

²¹

All rights reserved.

22

A mia mamma e mio babbo,

23

grazie per le radici e grazie per le ali.

24

To my mom and dad,

25

thank you for the roots and thank you for the wings.

²⁶ Contents

²⁷	Acknowledgements	viii
²⁸	0 Introduction	1
²⁹	1 The theoretical framework	6
³⁰	1.1 The Standard Model	6
³¹	1.2 Neutrinos: tiny cracks in the Standard Model	9
³²	1.2.1 Neutrinos in the Standard Model	9
³³	1.2.2 Neutrino Oscillations	11
³⁴	1.2.3 Make up of Neutrino Interactions	12
³⁵	1.3 Beyond the Standard Model	14
³⁶	1.3.1 Open Questions in Neutrino Physics	16
³⁷	1.3.2 Towards a more fundamental theory: GUTs	20
³⁸	1.4 Motivations for Hadronic Cross Sections in Argon	23
³⁹	1.4.1 Pion-Argon Total Hadronic Cross Section	23
⁴⁰	1.4.2 Kaon-Argon Total Hadronic Cross Section	34
⁴¹	2 Liquid Argon Detectors at the Intensity Frontier	39
⁴²	2.1 The Liquid Argon Time Projection Chamber Technology	39
⁴³	2.1.1 TPCs, Neutrinos & Argon	40
⁴⁴	2.1.2 LArTPC: Principles of Operation	42

45	2.1.3	Liquid Argon: Ionization Charge	45
46	2.1.4	Liquid Argon: Scintillation Light	50
47	2.1.5	Signal Processing and Event Reconstruction	54
48	2.2	The Intensity Frontier Program	58
49	2.2.1	Prospects for LArTPCs in Neutrino Physics: SBN and DUNE	59
50	2.2.2	Prospects for LArTPCs in GUT Physics: DUNE	60
51	2.2.3	Enabling the next generation of discoveries: LArIAT	62
52	3	LArIAT: Liquid Argon In A Testbeam	65
53	3.1	The Particles' Path to LArIAT	65
54	3.2	LArIAT Tertiary Beam Instrumentation	67
55	3.2.1	Bending Magnets	68
56	3.2.2	Multi-Wire Proportional Chambers	70
57	3.2.3	Time-of-Flight System	72
58	3.2.4	Punch-Through and Muon Range Stack Instruments	73
59	3.2.5	LArIAT Cosmic Ray Paddle Detectors	75
60	3.3	In the Cryostat	76
61	3.3.1	Cryogenics and Argon Purity	76
62	3.3.2	LArTPC: Charge Collection	79
63	3.3.3	LArTPC: Light Collection System	82
64	3.4	Trigger and DAQ	85
65	3.5	Control Systems	86
66	4	Total Hadronic Cross Section Measurement Methodology	92
67	4.1	Event Selection	93
68	4.1.1	Selection of Beamline Events	93
69	4.1.2	Particle Identification in the Beamline	94
70	4.1.3	TPC Selection: Halo Mitigation	94

71	4.1.4	TPC Selection: Shower Removal	95
72	4.2	Beamline and TPC Handshake: the Wire Chamber to TPC Match . .	96
73	4.3	The Thin Slice Method	98
74	4.3.1	Cross Sections on Thin Target	98
75	4.3.2	Not-so-Thin Target: Slicing the Argon	99
76	4.3.3	Corrections to the Raw Cross Section	101
77	4.4	Procedure testing with truth quantities	102
78	5	Data and MC preparation for the Cross Section Measurements	105
79	5.1	Cross Section Analyses Data Sets	105
80	5.2	Construction of a Monte Carlo Simulation for LArIAT	107
81	5.2.1	G4Beamline	107
82	5.2.2	Data Driven MC	112
83	5.3	Estimate of Backgrounds in the Pion Cross Section	115
84	5.3.1	Background from Pion Capture and Decay	115
85	5.3.2	Contributions from the Beamline Background	118
86	5.4	Estimate of Energy Loss before the TPC	121
87	5.5	Tracking Studies	125
88	5.5.1	Angular Resolution	125
89	5.6	Calorimetry Studies	131
90	5.6.1	Kinetic Energy Measurement	131
91	6	Negative Pion Cross Section Measurement	134
92	6.1	Raw Cross Section	134
93	6.1.1	Statistical Uncertainty	136
94	6.1.2	Treatment of Systematics	138
95	6.2	Corrections to the Raw Cross Section	139
96	6.2.1	Background subtraction	139

97	6.2.2 Efficiency Correction	142
98	6.3 Results	146
99	7 Positive Kaon Cross Section Measurement	148
100	7.1 Raw Cross Section	148
101	7.2 Corrections to the Raw Cross Section	150
102	7.3 Results	152
103	8 Conclusions	155
104	A Additional Tracking Studies for LArIAT Cross Section Analyses	156
105	A.0.1 Study of WC to TPC Match	157
106	A.0.2 Tracking Optimization	159
107	B Energy Calibration	160

¹⁰⁸ Acknowledgements

¹⁰⁹ “*Dunque io ringrazio tutti quanti.*

¹¹⁰ *Specie la mia mamma che mi ha fatto così funky.”*

¹¹¹ – Articolo 31, Tanqi Funky, 1996 –

¹¹² “*At last, I thank everyone.*

¹¹³ *Especiallly my mom who made me so funky.”*

¹¹⁴ – Articolo 31, Tanqi Funky, 1996 –

¹¹⁵ A lot of people are awesome, especially you, since you probably agreed to read

¹¹⁶ this when it was a draft.

¹¹⁷ Chapter 0

¹¹⁸ Introduction

¹¹⁹ This thesis work concerns the first measurement of the (π^- -Ar) total hadronic cross
¹²⁰ section in the 100-1000 MeV kinetic energy range and the first measurement of the
¹²¹ (K^+ -Ar) total hadronic cross section in the 100-650 MeV kinetic energy range. We
¹²² performed these measurements at the LArIAT experiment, a small (0.25 ton) Liquid
¹²³ Argon Time Projection Chamber (LArTPC) on a beam of charge particles at the
¹²⁴ Fermilab Test Beam Facility. Albeit particle and nuclear physics has a long history of
¹²⁵ hadronic cross section measurements, the work outlined in this thesis presents a new
¹²⁶ methodology (the “thin slice method”) possible only thanks to the excellent tracking
¹²⁷ and calorimetry capabilities of the LArTPC technology.

¹²⁸ A renewed interest for precision measurements of hadronic cross sections in argon
¹²⁹ arises from the current panorama of experimental neutrino physics.

¹³⁰ The discovery of the Higgs boson in 2012 marked the triumph of the Standard
¹³¹ Model of Particle Physics; exploring what lays beyond is the real challenge in our field
¹³² today. Since their formulation in 1930, neutrinos have been a source of surprises (and
¹³³ Nobel Prizes) for particle physicists, tiny cracks in our understanding of Nature. In
¹³⁴ particular, the discovery of neutrino oscillation represents the first evidence of physics
¹³⁵ Beyond the Standard Model (BSM). From a theoretical point of view, the field is

136 developing new theories to account for the small but non-zero mass of neutrinos,
137 while trying to remain consistent with the rest of the Standard Model. From an
138 experimental point of view, we are developing technologies and huge collaborations to
139 probe these theories. Even today, neutrinos might hold the key to the next generation
140 of discoveries in particle physics.

141 According to the latest Particle Physics Project Prioritization Panel [107], the US
142 particle physics panorama is directing a substantial effort towards the exploration of
143 the Intensity Frontier. In particular, the near future will see the development of a
144 Short Baseline Neutrino Program (SBN) and long baseline neutrino program with
145 DUNE as far detector. Both these program are based on the Liquid Argon Time
146 Projection Chamber (LArTPC) detector technology. The US liquid argon program
147 has the potential to answer many of the fundamental open questions in particle physics
148 today, such as: is there a fourth generation neutrino? is CP violated in the lepton
149 sector? are there any additional symmetries? And, can we find an indication of
150 Grand Unified Theories?

151 The SBN program at Fermilab is tasked with conclusively addressing the existence
152 of a fourth neutrino generation in the $\Delta m^2 = \Delta m_{14}^2 \sim [0.1 - 10] \text{ eV}^2$ parameter space.
153 The SBN program entails three surface LArTPCs positioned on the Booster Neutrino
154 Beam at different distances from the neutrino production in oder to fully exploit the
155 L/E dependence of the oscillation pattern: SBND (100 m from the decay pipe),
156 MicroBooNE (450 m), and ICARUS (600 m). SBN will also perform an extensive
157 program of neutrino cross section measurements, fundamental to abate systematics
158 in the oscillation analyses in both SBN and DUNE.

159 The long baseline neutrino program and DUNE in particular has a wide physics
160 program. For what it concerns neutrino physics, DUNE has the capability of solving
161 the mass hierarchy and octant problem, and discovering CP violation in the neu-
162 trino sector. Besides its neutrino program, DUNE can open an experimental window

163 on Grand Unified Theories (GUTs). GUTs could potentially answer fundamental
164 questions such as the existence of non-zero neutrino masses and matter-antimatter
165 asymmetry, explaining some “accidents” in the Standard Models, such as the exact
166 cancellation of the proton and the electron charge. Probing GUTs at the unification
167 energy scale is impossible by any foreseeable collider experiment. An indirect proof
168 is thus needed such as baryon number violation, which is predicted by almost every
169 GUT in the form of proton decay, bounded nucleon decay or $n - \bar{n}$ oscillations on
170 long time-scales. Historically, the dominant technology used in these searches has
171 been water Cherenkov detectors, with Super-Kamiokande setting all the current ex-
172 perimental limits on the decay lifetimes at the order of $\sim 10^{34}$ years. The DUNE
173 far detector and its non-accelerator physics program is a interesting new actor on
174 this stage. LArTPCs can in fact complement nucleon decay searches in modes where
175 water Cherenkov detectors are less sensitive, especially $p \rightarrow K^+ \bar{\nu}$ [11].

176 **Brief history of nu detectors**

177 • Brief history of nu detectors

178 • Calibration : LArIAT

179 • The measurements

180 LArTPCs provide excellent electron/photon separation [9] lacking in Cherenkov
181 detectors which can be leveraged to abate the photon background from neutral current
182 interactions in ν_e searches. LArTPCs share superb tracking capability with bubble
183 chamber detectors, with several additional benefits. They are electronically read out
184 and self triggered detectors; they provide full 3D-imaging with millimeter resolution,
185 precise calorimetric reconstruction and excellent particle identification. Plus, female
186 physicists are actually writing code and running experiments, not (only) staring at
187 images – Too much? – [69].

188 The complexity of the LArTPC technology for neutrino detection is due to several
189 reasons. Argon is a fairly heavy element, which means that nuclear effects play an
190 important role in the looks of the interaction topology. Also, data on charged particle
191 interaction in argon is scarce; no measurement of hadronic cross sections for pions or
192 kaons is available for argon. Secondly,

193 LArIAT [38], a small (0.25 ton) LArTPC on a beam of charge particles at the
194 Fermilab Test Beam Facility, is performing precise cross section measurements of
195 charged particles in argon. The LArIAT suite of cross section measurements is a
196 critical set of results which will be employed by both the short- and long- baseline
197 neutrino programs. This work is a measurement of the negative pion argon and the
198 positive kaon-argon total hadronic differential cross sections.

199 The (π^- -Ar) hadronic cross section is a fundamental input for neutrino detectors
200 in liquid argon. In fact, reconstructing neutrino interactions at the GeV scale where
201 pion production is abundant.

202 The total hadronic differential cross sections is of particular interest for proton
203 decay searches in DUNE, whose most interesting proton decay channel is $p \rightarrow K^+ \bar{\nu}$.

204 The cross section analyses exploit the totality of LArIAT's experimental handles;
205 they rely on beam line detector information as well as both calorimetry and tracking
206 in the TPC. These analyses are LArIAT's first physics results.

207 The (K^+ -Ar) total hadronic differential cross section in LArIAT is particularly
208 relevant for a high identification efficiency in the context of proton decay searches in
209 DUNE in the $p \rightarrow K^+ \bar{\nu}$ channel. In fact, the kaon-argon cross section affects the
210 kaon topology by modifying the kaon tracking and energy reconstruction, impacting
211 the basis for kaon identification in a LArTPC.

212 A series of additional studies and calibrations were necessary to perform the cross
213 section analyses. Appendix ?? shows a measurement of the LArIAT LArTPC electric
214 field using cosmic data. Appendix ?? shows an optimization of the tracking algorithms

215 geared towards maximizing the efficiency of finding the hadronic interaction point.
216 Appendix ?? shows the calorimetry calibration of the LArIAT LArTPC, which is a
217 pivotal measurement to enable any physics analysis with TPC data.

218 In order to measure the kaon-argon differential cross section, several steps were
219 necessary. The analysis starts by identifying a sample of kaons in the beam line and
220 assessing the beam line contaminations. It proceeds with tracking the kaon candi-
221 dates in the TPC and measuring their calorimetry. Then, the hadronic interaction
222 point is identified and distinguished from weak interaction cases. The last step of the
223 analysis, which is the energy unfolding, is now ongoing. With this measurement, I ac-
224 quired extensive experience in tracking hadrons and measuring their energy inside the
225 TPC. This entailed both an in-depth study of the tracking algorithms performances
226 on data and a dive into the GEANT4 transportation models. Since no previous kaon
227 measurement has been performed on argon, simulation packages such as GEANT4
228 currently interpolate the kaon transportation on (scarce) data from lighter and heav-
229 ier nuclei. This is suboptimal for proton decay searches. In fact, an extremely high
230 signal detection efficiency, measured by testing identification algorithms on simula-
231 tion, is extremely difficult to obtain if the simulation is not reliable. By adding the
232 experimental data points for kaon-argon cross section to the simulation, my thesis
233 analysis will cover this gap of knowledge.

234 Chapters:1 Chapter 2 Chapter 3

²³⁵ **Chapter 1**

²³⁶ **The theoretical framework**



²³⁷ – J. S. Bach, 1720 ca. –

²³⁸ In this chapter, we set the (π^- - Ar) and (K^+ - Ar) total hadronic cross section
²³⁹ measurements into the greater theoretical and phenomenological framework. We start
²⁴⁰ by briefly describing the Standard Model (Section 1.1), with particular attention to
²⁴¹ neutrinos and neutrino interactions (Section 1.2). We then describe some of the
²⁴² open questions in neutrino physics today and Beyond Standard Model theories (1.3)
²⁴³ setting the stage for the measurements reported in this work (Section 1.4).

²⁴⁴ **1.1 The Standard Model**

²⁴⁵ The Standard Model (SM) of particle physics is the most accurate theoretical descrip-
²⁴⁶ tion of the subatomic world and, in general, one of the most precisely tested theories
²⁴⁷ in the history of physics. The SM describes the strong, electromagnetic and weak
²⁴⁸ interactions among elementary particles in the framework of quantum field theory,

249 accounting for the unification of electromagnetic and weak interactions for energies
250 above the vacuum expectation value (VEV) of the Higgs field. The SM does not
251 describe gravity or general relativity.

252 The Standard Model is a gauge theory based on the local symmetry group

$$G_{SM} = SU(3)_C \otimes SU(2)_L \otimes U(1)_Y \quad (1.1)$$

253 where the subscripts C indicates the conserved strong charge (color), and the
254 subscripts Y indicates the conserved hypercharge. If we indicated with T the weak
255 isospin T and with T3 its third component, hypercharge can be related to the electric
256 charge Q through the Gell-Mann-Nishijima relation:

$$Q = \frac{Y}{2} + T_3. \quad (1.2)$$

257 In the quantum field framework, the SM fields correspond to the irreducible rep-
258 resentations of the G_{SM} symmetry group. In particular, the particles are divided in
259 two categories, fermions and bosons, according to their spin-statistics. Described by
260 the Fermi-Dirac statistics, fermions have half-integer spin and are sometimes called
261 “matter-particles”. Bosons or “force carriers” have integer spin, follow the Bose-
262 Einstein statistics and mediate the interaction between fermions. The fundamental
263 fermions and their quantum numbers are listed in Tab 1.1.

264 Quarks can interact via all three the fundamental forces; they are triplets of
265 $SU(3)_C$, that is they can exist in three different colors. If one chooses a base where
266 u , c and t quarks are simultaneously eigenstates of both the strong and the weak
267 interactions, the remaining eigenstates are usually written as d , s and b for the strong
268 interaction and d' , s' and b' for the weak interaction, because the latter ones are
269 the result of a CKM rotation on the first ones. Charged leptons interact via the
270 weak and the electromagnetic forces, while neutrinos only interact via the weak force.

Generation	I	II	III	T	Y	Q
Leptons	$\begin{pmatrix} \nu_e \\ e \end{pmatrix}_L$	$\begin{pmatrix} \nu_\mu \\ \mu \end{pmatrix}_L$	$\begin{pmatrix} \nu_\tau \\ \tau \end{pmatrix}_L$	1/2 -1/2	-1 -1	0 -1
	e_R	μ_R	τ_R	0	-2	1
Quarks	$\begin{pmatrix} u \\ d' \end{pmatrix}_L$	$\begin{pmatrix} c \\ s' \end{pmatrix}_L$	$\begin{pmatrix} t \\ b' \end{pmatrix}_L$	1/2 -1/2	1/3 1/3	2/3 -1/3
	u_R d'_R	c_R s'_R	t_R b'_R	0 0	4/3 -2/3	2/3 -1/3

Table 1.1: SM elementary fermionic fields. The subscripts L and R indicate respectively the negative chirality (left-handed) and the positive chirality (right-handed).

- 271 The gauge group univocally determines the number of gauge bosons that carry the
 272 interaction; the gauge bosons correspond to the generators of the group: eight gluons
 273 (g) for the strong interaction, one photon (γ) and three bosons (W^\pm , Z^0) for the
 274 electroweak interaction. A gauge theory by itself cannot provide a description of
 275 massive particles, but it is experimentally well known that most of the elementary
 276 particles have non-zero masses. The introduction of massive fields in the Standard
 277 Model lagrangian would make the theory not gauge invariant, resulting ill-defined.
 278 This problem is solved in the SM by the introduction of a scalar iso-doublet $\Phi(x)$, the
 279 Higgs field, which gives mass to W^\pm and Z^0 gauge bosons through the electroweak
 280 symmetry breaking mechanism and to the fermions through Yukawa coupling [76, 77].
 281 The discovery of the Higgs boson in 2012 by the LHC experiments [41, 42] marked
 282 the ultimate confirmation of a long history of successful predictions by the SM.

283 1.2 Neutrinos: tiny cracks in the Standard Model

284 To our current knowledge, neutrinos are the most abundant fermion in the Universe.
285 And yet, they are maybe the most mysterious particle in the SM: they generate
286 theoretical puzzles and experimental challenges. In this section, we treat neutrinos
287 within and beyond the SM and describe the make up of their interaction with matter.

288 1.2.1 Neutrinos in the Standard Model

289 Neutrino can be introduced in the SM as left-handed massless Weyl spinors. The
290 Dirac equation of motion for a free field

$$(i\gamma^\mu \partial_\mu - m)\psi = 0 \quad (1.3)$$

291 for a fermionic field

$$\psi = \psi_L + \psi_R \quad (1.4)$$

292 is equivalent to the equations

$$i\gamma^\mu \partial_\mu \psi_L = m\psi_R \quad (1.5)$$

293

$$i\gamma^\mu \partial_\mu \psi_R = m\psi_L \quad (1.6)$$

294 for the chiral fields ψ_R and ψ_L , whose evolution in space and time is coupled
295 through the mass m . If the fermion is massless, the chiral fields decouple and the
296 fermion can be described by a single Weyl spinor with two independent compo-
297 nents [116]. Pauli initially rejected the description of a physical particle through
298 a single Weyl spinor because of its implication of parity violation. In fact, since
299 the spatial inversion operator throws $\psi_R \leftrightarrow \psi_L$, parity is conserved only if both chi-
300 ral components exist at the same time. For the neutrino introduction in the SM,
301 experiments came in help of the theoretical description. The constraint of parity

302 conservation weakened after Wu's experiment in 1957 [119]. Additionally, there was
 303 no experimental indication for massive neutrinos, nor evidence of interaction via the
 304 neutrino right-handed component.

305 The symmetry group $SU(2)_L \otimes U(1)_Y$ is the only group relevant for neutrino
 306 interactions. The SM electroweak lagrangian is the most general renormalizable la-
 307 grangian invariant under the local symmetry group $SU(2)_L \otimes U(1)_Y$. The lagrangian
 308 couples the weak isotopic spin doublets and singlets described in Table 1.1 with the
 309 gauge bosons A_a^μ ($a = 1,2,3$) and B^μ , and Higgs doublet $\Phi(x)$:

$$\begin{aligned} \mathcal{L} = & i \sum_{\alpha=e,\mu,\tau} \bar{L}'_{\alpha L} \not{D} L'_{\alpha L} + i \sum_{\alpha=1,2,3} \bar{Q}'_{\alpha L} \not{D} Q'_{\alpha L} \\ & + i \sum_{\alpha=e,\mu,\tau} \bar{l}'_{\alpha R} \not{D} l'_{\alpha R} + i \sum_{\alpha=d,s,b} \bar{q}'^D_{\alpha R} \not{D} q'^D_{\alpha R} + i \sum_{\alpha=u,c,t} \bar{q}'^U_{\alpha R} \not{D} q'^U_{\alpha R} \\ & - \frac{1}{4} A_{\mu\nu} A^{\mu\nu} - \frac{1}{4} B_{\mu\nu} B^{\mu\nu} \\ & + (D_\rho \Phi)^\dagger (D^\rho \Phi) - \mu^2 \Phi^\dagger \Phi - \lambda (\Phi^\dagger \Phi)^2 \\ & - \sum_{\alpha,\beta=e,\mu,\tau} \left(Y_{\alpha\beta}^l \bar{L}'_{\alpha L} \Phi l'_{\beta R} + Y_{\alpha\beta}^{l*} \bar{l}'_{\beta R} \Phi^\dagger L'_{\alpha L} \right) \\ & - \sum_{\alpha=1,2,3} \sum_{\beta=d,s,b} \left(Y_{\alpha\beta}^D \bar{Q}'_{\alpha L} \Phi q'^D_{\beta R} + Y_{\alpha\beta}^{D*} \bar{q}'^D_{\beta R} \Phi^\dagger Q'_{\alpha L} \right) \\ & - \sum_{\alpha=1,2,3} \sum_{\beta=u,c,t} \left(Y_{\alpha\beta}^U \bar{Q}'_{\alpha L} \tilde{\Phi} q'^U_{\beta R} + Y_{\alpha\beta}^{U*} \bar{q}'^U_{\beta R} \tilde{\Phi}^\dagger Q'_{\alpha L} \right). \end{aligned} \quad (1.7)$$

310 The first two lines of the lagrangian summarize the kinetic terms for the fermionic
 311 fields and their coupling to the gauge bosons $A_a^{\mu\nu}$, $B^{\mu\nu}$ ¹. The third line describes
 312 the kinetic terms and the self-coupling terms of the gauge bosons. The forth line is
 313 the Higgs lagrangian, which results in the spontaneous symmetry breaking. The last
 314 three lines describe the Yukawa coupling between fermions and the Higgs field, origin
 315 of the fermions' mass.

1. In gauge theories the ordinary derivative ∂_μ is substituted with the covariant derivative D_μ . Here $D_\mu = \partial_\mu + igA_\mu \cdot I + ig'B_\mu \frac{Y}{2}$, where I and Y are the $SU(2)_L$ and $U(1)_Y$ generators, respectively.

316 The coupling between left-handed and right-handed field generates the mass term
317 for fermions. The SM assumes only left-handed components for neutrinos, thus im-
318 plying zero neutrino mass. Since any linear combination of massless fields results in a
319 massless field, the flavor eigenstates are identical to the mass eigenstates in the SM.

320 1.2.2 Neutrino Oscillations

321 The determination of the flavor of a neutrino dynamically arises from the correspond-
322 ing charged lepton associated in a change current interaction; for example, a ν_e is a
323 neutrino which produces an e^- , a $\bar{\nu}_\mu$ is a neutrino which produces a μ^+ , etc. The
324 neutrino flavor eigenstates $|\nu_\alpha\rangle$, with $\alpha = e, \mu, \tau$, are orthogonal to each other and
325 form a base for the weak interaction matrix.

326 Overwhelming experimental data show that neutrinos change flavor during their
327 propagation [102]. This phenomenon, called “neutrino oscillations”, was predicted
328 first by Bruno Pontecorvo in 1957 [103]. Neutrino oscillations are possible only if
329 the neutrino flavor eigenstate are not identical to the mass eigenstates. Thus, the
330 observation of neutrino oscillation results in the first evidence of physics beyond the
331 Standard Model. A minimal extension of the SM introduces three mass eigenstates,
332 $|\nu_i\rangle$ ($i = 1, 2, 3$), whose mass m_i is well defined. The unitary Pontecorvo-Maki-
333 Nakagawa-Sakata matrix transforms the mass base into the flavor base as follows

$$|\nu_\alpha\rangle = U_{PMNS} |\nu_i\rangle, \quad (1.8)$$

334 with

$$U_{PMNS} = \begin{bmatrix} c_{12} & s_{12} & 0 \\ -s_{12} & c_{12} & 0 \\ 0 & 0 & 1 \end{bmatrix} \begin{bmatrix} c_{13} & 0 & s_{13}e^{-i\delta} \\ 0 & 1 & 0 \\ -s_{13}e^{-i\delta} & 0 & c_{13} \end{bmatrix} \begin{bmatrix} 1 & 0 & 0 \\ 0 & c_{23} & s_{23} \\ 0 & -s_{23} & c_{23} \end{bmatrix} \begin{bmatrix} e^{i\alpha_1} & 0 & 0 \\ 0 & e^{i\alpha_2} & 0 \\ 0 & 0 & 1 \end{bmatrix} \quad (1.9)$$

335 where c e s stand respectively for cosine and sine of the corresponding mixing
 336 angles (θ_{12} , θ_{23} and θ_{13}), δ is the Dirac CP violation phase, α_1 and α_2 are the eventual
 337 Majorana CP violation phases. Experimental results on neutrino oscillations are
 338 generally reported in terms of the mixing angles and of the squared mass splitting
 339 $\Delta m_{ab}^2 = m_a^2 - m_b^2$, where a and b represent the mass eigenstates. A summary of the
 340 current status of experimental results, albeit partial, is given in table 1.2.

Table 1.2: Summary of experimental results on neutrino oscillation parameters. **ADD CITATIONS**

	Value	Precision	Experiment
θ_{23}	45°	9.0%	Super Kamiokande, MINOS,
$-\Delta m_{32}^2$	$2.5 \cdot 10^{-3} \text{ eV}^2$	1.8%	Nova, MACRO
θ_{12}	34°	5.8%	SNO, Gallex,
$-\Delta m_{12}^2$	$7.4 \cdot 10^{-5} \text{ eV}^2$	2.8%	SAGE, KamLAND
θ_{13}	9°	4.7%	DAYA Bay,
$-\Delta m_{32}^2$	$2.5 \cdot 10^{-3} \text{ eV}^2$	1.8%	RENO

341 1.2.3 Make up of Neutrino Interactions

342 All neutrino experiments involving the detection of single neutrinos are concerned
 343 with neutrino interactions (and neutrino cross sections) on nuclei. Given the invisible
 344 nature of the neutrino, characterizing the products of its interaction is the only
 345 method to a) assess the neutrino presence, b) detect its flavor in case of a charge
 346 current interaction and c) eventually reconstruct its energy.

347 Historically, neutrino interactions with the nucleus in the GeV region are divided
 348 into three categories into three categories whose contributions change as a function

349 of increasing neutrino energy:: quasi elastic (QE), resonant (RES), and deep inelastic
350 (DIS) scattering. All current and forthcoming oscillation experiments on neutrino
351 beams live in the 0.1-10 GeV transition region, which encompasses the energy where
352 the QE neutrino-nucleus interaction transitions into RES and then into DIS. For
353 scattering off free nucleons, neutrino and antineutrino QE charge current scattering
354 refers to the process $\nu_l n \rightarrow l^- p$ and $\bar{\nu}_l p \rightarrow l^+ n$ where a charged lepton and single
355 nucleon are ejected in the elastic interaction. Resonant scattering refers to an inelas-
356 tic collision producing a nucleon excited state (Δ, N^*) – the resonance – which then
357 quickly decays, most often to a nucleon and single-pion final state. DIS refers to the
358 head-on collision between the neutrino and a parton inside the nucleon, producing
359 hadronization and subsequent abundant production of mesons and nucleons. In addi-
360 tion to such interactions between the neutrino and a single component of the nucleus,
361 neutrinos can also interact with the nucleus as a whole, albeit more rarely, a well
362 documented process called coherent meson production scattering [58]; the signature
363 of such process is the production of a distinctly forward-scattered single meson final
364 state, most often a pion. This simple picture of neutrino interactions works rather
365 well for scattering off of light nuclear targets, such as the H₂ and D₂ of bubble cham-
366 ber experiments [64], but the complexity of the nuclear structure for heavier nuclei
367 such as argon complicates this model.

368 As we will discuss in Chapter 2, the properties of argon make it a good candidate
369 for an interacting medium in neutrino experiments; in particular the density of its
370 interaction centers increases the yield of neutrino interactions and allows for relatively
371 compact detectors. Though, the choice of a relatively heavy nuclear target comes at
372 the cost of enhancing nuclear effects which modify the kinematic and final state of
373 the neutrino interaction products.

374 Nuclear effects can potentially affect neutrino event rates, final state particle emis-
375 sion, neutrino energy reconstruction, and the neutrino/antineutrino ratios, carrying

376 deep implications for oscillation experiments. Even in the case of “simple” QE scat-
377 tering, intra-nuclear hadron rescattering and correlation effects between the target
378 nucleons can cause the ejection of additional nucleons in the final state, modifying
379 the final state kinematics and topology. In the case of resonant and DIS scattering,
380 the hadronic interactions of meson and nucleons produced in the decay of the res-
381 onance or during hadronization complicate this picture even more. A large source
382 of uncertainty in modeling nuclear effects in neutrino interactions come from mesons
383 interactions (and re-interactions) in the nucleus, e.g., pion re-scattering, charge ex-
384 change, and absorption.

385 A renewed interest for neutrino cross section measurements surged in recent years,
386 along with a lively discussion on the data reporting; the historical method of reporting
387 the neutrino cross section as a function of the neutrino energy or momentum trans-
388 fered shakes under the weight of its dependency on the chosen nuclear model. On one
389 hand, correcting for nuclear effects in neutrino interaction can introduce unwanted
390 sources of uncertainty and model dependency especially due to the mis-modeling of
391 the meson interactions. On the other, avoiding this correction makes a comparison
392 between neutrino interactions on different target nuclei extremely difficult.

393 Data on neutrino scattering off many different nuclei are available for both charged
394 current (CC) and neutral current (NC) channels, as summarized in [64]. A summary
395 of the results on QE, resonant and DIS scattering for neutrinos and antineutrinos from
396 accelerators on different target is reported in Figure 1.1, where the (NUANCE) [37]
397 event generator is used as comparison with the theory.

398 1.3 Beyond the Standard Model

399 The discovery of neutrino oscillation and its implication of non-zero neutrino mass
400 mark the beginning of a new, exciting era in neutrino physics: the era of physics Be-

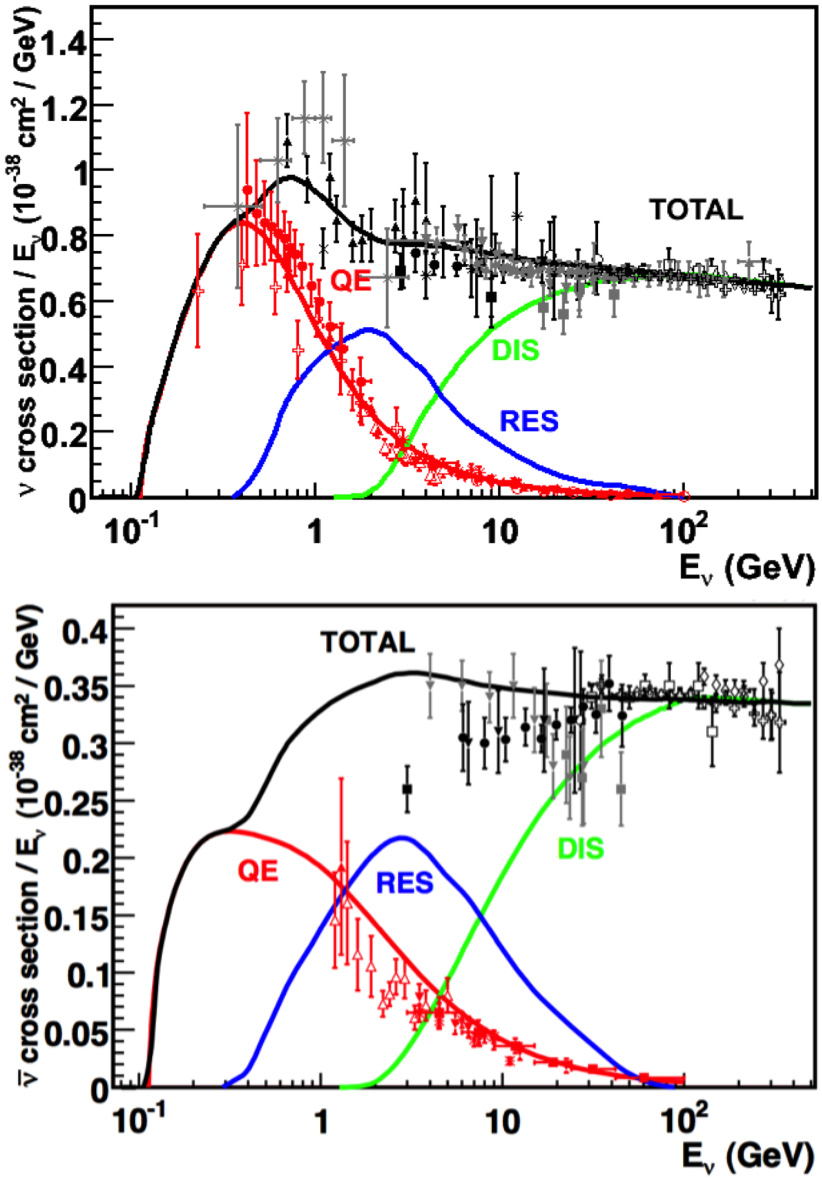


Figure 1.1: Total neutrino (top) and antineutrino (bottom) CC cross sections per nucleon divided by neutrino energy as a function of energy as reported in [64]. Predictions for the total (black), the QE (red), resonant (blue) and DIS (green) are provided by the NUANCE generator. The quasi-elastic scattering data and predictions have been averaged over neutron and proton targets (isoscalar target).

401 yond the Standard Model (BSM) at the intensity frontier. We are currently searching
402 for new, deeper theories that can accommodate neutrinos with tiny but non-zero
403 masses, while remaining consistent with the rest of the Standard Model.

404 **1.3.1 Open Questions in Neutrino Physics**

405 On one hand, the last three decades of experiments in neutrino oscillations brought
406 spectacular advancements in the understanding of the oscillations pattern, measuring
407 the neutrino mixing angles and mass splitting with a precision of less than 10%. On
408 the other, they opened the field for a series of questions needing experimental answers.

409 **Sterile neutrinos.** Hints to the existence of at least one additional neutrino,
410 in the form of various anomalies, have been puzzling physicists almost from the be-
411 ginning of neutrino oscillation searches. Originally designed to look for evidence of
412 neutrino oscillation, the Liquid Scintillator Neutrino Detector (LSND) [54] provided
413 a first conflicting result with the Standard Model expectation of only three neutrinos.

414 A second conflicting result has also been provided by the MiniBooNE experiment [50].
415 The LSND and MiniBooNE ν_e and $\bar{\nu}_e$ appearance results, known as the “LSND and
416 MiniBooNE anomalies” [14, 15, 23], may be interpreted under the assumption of a new
417 right-handed neutrino. The additional neutrino needs to be “sterile”, i.e needs not
418 to couple with the electroweak force carriers, in order to meet the constraint imposed
419 by the measurement of the width of the Z boson [2]. The new sterile neutrino would
420 mainly be composed of a heavy neutrino ν_4 with mass m_4 such that $m_1, m_2, m_3 \ll m_4$
421 and $\Delta m^2 = \Delta m_{14}^2 \sim [0.1 - 10]$ eV². The introduction of sterile neutrinos is an ap-
422 pealing line of thinking, since this renormalizable generalization of the SM has the
423 potential to impact long standing questions in high energy physics and cosmology:
424 light sterile neutrinos are candidates for dark matter particles and there are ideas
425 that the theory could be adjusted to explain the baryon asymmetry of the Universe
426 via leptogenesis [72].

427 **CP Violation In Lepton Sector.** The measurement of non-zero value for the
 428 oscillation parameter θ_{13} allows the exploration of low-energy CP violation in the lep-
 429 ton sector at neutrino long baseline oscillation experiments, enabling the possibility
 430 to measure the Dirac CP-violating phase δ . Exciting theoretical results tie δ directly
 431 to the generation of the baryon asymmetry of the Universe at the Grand Unified
 432 Theory scale **a couple of cit would be nice**. According to the theoretical model de-
 433 scribed in [101], for example, leptogenesis can be achieved if $|\sin \theta_{13} \sin \delta| > 0.11$, i.e.
 434 $\sin \delta > 0.7$.
 435 The asymmetry in the oscillation probability of neutrinos and antineutrinos is the ob-
 436 servable sensitive to the Dirac CP-violating phase δ leveraged in neutrino oscillation
 437 experiments. Using the parameterization of the PMNS matrix shown in Equation
 438 1.9, the difference between the probability of $\nu_e \rightarrow \nu_\mu$ oscillation and the probability
 439 of $\bar{\nu}_e \rightarrow \bar{\nu}_\mu$ oscillation can be parametrized as follows [39],

$$P_{\nu_e \rightarrow \nu_\mu} - P_{\bar{\nu}_e \rightarrow \bar{\nu}_\mu} = J \cos \left(\pm \delta - \frac{\Delta_{31} L}{2} \right) \sin \left(\frac{\Delta_{21} L}{2} \right) \sin \left(\frac{\Delta_{31} L}{2} \right) \quad (1.10)$$

440 where

$$J = \cos \theta_{13} \sin 2\theta_{13} \sin 2\theta_{12} \sin 2\theta_{23} \quad (1.11)$$

441 is the Jarlskog invariant [82], L the neutrino baseline, i.e. the distance between
 442 the neutrino production and detection points, and Δ_{ab} a factor proportional to the
 443 sign and magnitude of the mass splitting. From these equations, it is clear how the
 444 relative large value of θ_{13} is a happy accident necessary not to completely suppress
 445 the sensitivity to CP violation. The equations also show how the sensitivity to δ is
 446 tied to the measurement of the least precisely measured mixing angle, θ_{23} (via the
 447 $\sin 2\theta_{23}$ term) and to an other unknown quantity, the neutrino “mass hierarchy” (via
 448 the Δ_{ab} terms). The precise determination of θ_{23} is often referred as to “the octant
 449 problem”. Current experimental results [3, 12] are consistent with $\theta_{23} = 45^\circ$, which

450 would imply maximal mixing between ν_μ - ν_τ , hinting to an intriguing new symmetry.
451 Therefore, a precise measurement of θ_{23} is of great interest for theoretical models of
452 quark-lepton universality [75, 93, 106], whose quark and lepton mixing matrices are
453 proportional to the deviation of θ_{23} from 45°.

454 **Neutrino mass hierarchy.** The “mass hierarchy” problem refers to the unknown
455 ordering of the value of absolute mass of the neutrino mass eigenstates. Current
456 oscillation experiments are sensitive only to the magnitude of the mass splitting, and
457 not directly to its sign. In a framework where the lightest neutrino mass (arbitrarily)
458 corresponds to the first eigenstate m_1 , it is unknown whether $m_2 - m_1 < m_3 - m_1$
459 (Normal Hierarchy) or $m_2 - m_1 > m_3 - m_1$ (Inverted Hierarchy). The mass hierarchy
460 affects not only the sensitivity to CP violation searches in long baseline oscillation
461 experiments, but also the sensitivity to determine whether neutrinos are Majorana
462 particles in neutrinoless double beta decay experiments.

463 **Majorana or Dirac?** Evidence of neutrino oscillations demands the introduction
464 of a mechanism which can give mass to the neutrinos. This mechanism should possibly
465 also explain why neutrino masses are at least six orders of magnitude lower than the
466 electron mass (the second lightest SM fermion). In a description of neutrinos as Dirac
467 4-component spinors, the neutrino field acquires mass via the Higgs mechanism as
468 any other fermion of the SM. In this case, the neutrino mass is given by $m_a = \frac{y_a^\nu v}{\sqrt{2}}$,
469 where v is the Higgs VEV and y_a^ν is the Yukawa coupling between the Higgs and the
470 neutrino. The smallness of neutrino masses can only be pinned on a tiny Yukawa
471 coupling which is not justified by the theory.

472 In 1937, Majorana demonstrated that the introduction of a two components spinor is
473 sufficient to describe a massive fermion [92]. The Dirac equations of motion for the
474 chiral fields (equations 1.5 and 1.6) hold true in the case of two components spinor
475 under the assumption that the chiral components ψ_R and ψ_L are correlated through
476 the charge conjugation matrix \mathcal{C} , $\psi_R = \mathcal{C}\bar{\psi}_L$. Therefore the theory is applicable only

477 to neutral fermions. Neutrinos are the only neutral elementary particles in the SM
 478 – the only possible Majorana particle candidate. This theory constructs a neutrino
 479 Majorana mass term \mathcal{L}_5 of the following form in the Higgs unitary gauge

$$\mathcal{L}_5 = \frac{1}{2} \frac{gv^2}{\mathcal{M}} \nu_L^T \mathcal{C}^\dagger \nu_L, \quad (1.12)$$

480 where g is the coupling coefficient, v the Higgs VEV and \mathcal{M} a constant with the
 481 dimension of the mass proportional to the scale of new physics. The \mathcal{L}_5 term would
 482 introduce a non-renormalizable term in the lagrangian, since it has dimensions of
 483 energy to the fifth power. This is not allowed in the SM lagrangian; however, the
 484 existence of such terms is plausible if we consider the SM as an effective theory
 485 at low energy, manifestation of the symmetry breaking of a more general theory at
 486 higher energy, e.g. a Grand Unified Theory (GUT), and not the definitive theory.
 487 The mass term in eq 1.12 implies the neutrino mass to be $m = \frac{gv^2}{\mathcal{M}}$. The coupling
 488 coefficient can be of the order of any other fermion's coupling coefficient, since the
 489 smallness of neutrino masses is achieved by the big value of the new physics mass
 490 scale alone. This vanilla formulation is the conceptual basis for many flavors of *see-*
 491 *saw mechanism* [121], which we will not discuss here in any detail. However, it is
 492 fascinating how the puzzle of the neutrino mass hints to the existence of a deeper and
 493 more complete theory.

494 From a kinematic point of view, Dirac and Majorana neutrinos satisfy the same
 495 energy-momentum dispersion relationship. Thus, it is impossible to discern the neu-
 496 trino nature through kinematic effects such as neutrino oscillations. Neutrinoless
 497 double beta decay searches are the most promising way to understand the nature of
 498 the neutrino and are therefore subject of great theoretical and experimental interest.
 499 Observation of the lepton number violating process $0\nu\beta\beta$ would imply neutrinos have
 500 a Majorana component. Depending on the mass hierarchy, the theory also predicts

501 $0\nu\beta\beta$ exclusion regions and confirmation of the sole Dirac component for neutrinos [44].
502
503

504 1.3.2 Towards a more fundamental theory: GUTs

505 Despite its highly predictive power, a number of conceptual issues arise in the SM
506 which disfavor it to be a good candidate for a fundamental theory.

507 The SM does not include a suitable dark matter candidate and a mechanisms
508 that accounts for the baryon asymmetry of the universe. Additionally, up to a total
509 of 25 parameters remain seemingly arbitrary and need to be fitted to data: 3 gauge
510 couplings, 9 charged fermion masses, 3 mixing angles and one CP phase in the CKM
511 matrix, the Higgs mass and quartic coupling, θ_{QCD} , 3 neutrino mixing angles, 1 Dirac
512 phase and, eventually, 2 Majorana phases.

513 From a group theory perspective, the SM has a rather complex group structure,
514 where a gauge group is formed with the direct product of other three groups as shown
515 in eq. 1.1. Drawing a parallel with the electroweak symmetry breaking mechanism,
516 where the $SU(2)_L \otimes U(1)_Y$ is recovered from $U(1)_{EM}$, an interesting line of simplification
517 for the SM group structure would be to devise a similar mechanism where
518 $SU(3)_C \otimes SU(2)_L \otimes U(1)_Y$ is recovered from an hypothetical larger group. IS THIS
519 CORRECT? Just as the electroweak unification becomes evident at energies higher
520 than the Higgs VEV, a direct manifestation of Grand Unification Theories (GUTs)
521 would occur at even higher energies.

522 As the smallness of neutrino masses suggests the existence of a higher mass scale,
523 an other, even stronger, hint to Grand Unification comes from the slope of running
524 of the coupling constants. The coupling constants for the electromagnetic, weak and
525 strong interactions in the SM vary as a function of the interaction energy as shown
526 in figure 1.2; they do not exactly meet under the current experimental constraints,

⁵²⁷ but their trend is interesting enough to push for the construction of theories where
⁵²⁸ perfect unification is achieved through the addition of new particles.

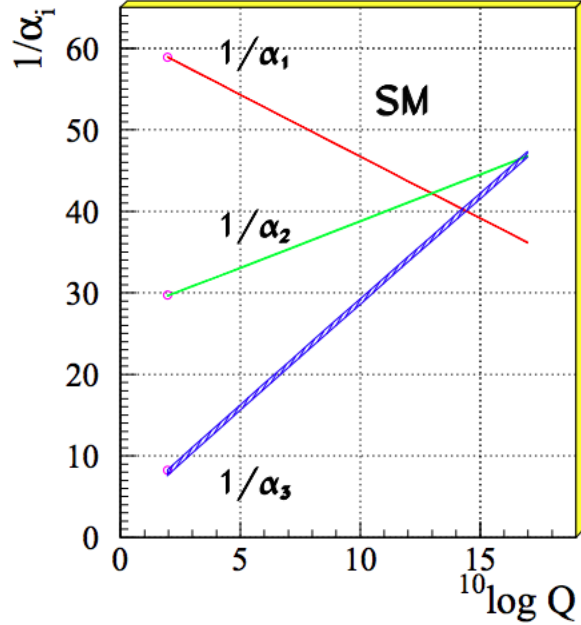


Figure 1.2: Evolution of the inverse of the three coupling constants in the Standard Model as a function of the momentum transferred, [86].

SU(5). The smallest simple group containing $SU(3)_C \otimes SU(2)_L \otimes U(1)_Y$ is SU(5), as shown first by Georgi and Glashow in [68]. Quarks and leptons in this group fit the $\bar{5}$ and 10 representations. The representation for left-handed fermions are the following

$$\bar{5} = (\nu_e, e^-)_L + \bar{d}_L \quad (1.13)$$

$$10 = e_L^+ + \bar{u}_L + (u, d)_L, \quad (1.14)$$

⁵²⁹ while the boson structure gains a new couple of super heavy bosons (X,Y)

$$24 = \underbrace{(8, 1)}_{\text{gluons}} + \underbrace{(1, 3) + (1, 1)}_{W^\pm, Z, \gamma} + \underbrace{(3, 2) + (\bar{3}, 2)}_{X, Y \text{ bosons}}. \quad (1.15)$$

⁵³⁰ Nice features such as charge quantization and the identity between the positron

and proton charge value come directly from the group structure. The new super heavy bosons are colored and form a weak doublet. Their are the mediator of the interaction that turns quarks into leptons, leading to predict the existence of processes that violate baryon number, such as $p \rightarrow \pi^0 + e^+$ (see fig 1.8, right). The prediction for proton decay lifetime, $\tau_p \sim \frac{M_X^4}{m_p^5} \sim 10^{30 \pm 1.5}$ years, is unfortunately experimentally disproved by IMB and Super-Kamiokande [4, 28].

SO(10). More complicated group structures, such as SO(10) are still viable candidates for GUT. SO(10) includes the same type of X and Y bosons as SU(5). Right-handed massive neutrinos are embedded in the construction of the irreducible representation of SO(10). Different patterns of SO(10) symmetry breaking to recover the SM are possible and lead to different predictions for the proton decay lifetime; some of these predictions are not excluded by the experiments [87].

SUSY GUTs. Supersymmetry theories allow for another family of GUTs. In SUSY, every fundamental particle in the SM has a “superpartner”, identical in each quantum number except for the spin-statistics: the fermion supersymmetric partners are bosons and vice versa. Collider experiments (mainly LHC) constrain the mass of the supersymmetric partners to be very heavy [?]. The SU(5), SU(10) groups with a SUSY twist are the basic groups for SUSY GUTs. From the phenomenology point of view, SUSY models tend to push the proton decay life time higher by a factor of four, they solve the “hierarchy problem”, and they also predict new channels for the proton decay. In particular they predict the presence of kaons in the final product, with a dominant mode of $p \rightarrow K^+ \bar{\nu}$. Predictions on the proton decay lifetime depend on the chosen SUSY model; again, some of the predictions are not excluded by the experiments [90, 91, 110].

555 **1.4 Motivations for Hadronic Cross Sections in Ar-**
556 **gon**

557 Critical challenges await the next decade of high energy physics at the intensity
558 frontier. Following the recommendation of the latest Particle Physics Project Priori-
559 tization Panel [107], the US is dedicating substantial resources to the development of
560 a short- and long- baseline neutrino program to address many of open questions in
561 neutrino physics today. This program pivots on the Liquid Argon Time Projection
562 Chamber (LArTPC) detector technology which will be described in Chapter 2.

563 The main goals of these research programs include:

- 564 - the assessment of the existence of right-handed sterile neutrinos via the study
565 of accelerator neutrinos on a short baseline (SBN),
- 566 - the determination of the sign of Δm_{13}^2 (or Δm_{23}^2), i.e., the neutrino mass hier-
567 archy via the study of accelerator neutrinos on a long baseline (DUNE),
- 568 - the determination of the octant, i.e. whether θ_{23} is maximal, via the study of
569 accelerator neutrinos on a long baseline (DUNE),
- 570 - the determination the status of CP symmetry in the lepton sector, via the study
571 of accelerator neutrinos on a long baseline (DUNE),
- 572 - the search for observables predicted by GUTs, such as proton decay via the
573 study of non accelerator physics in massive underground detectors (DUNE).

574 **1.4.1 Pion-Argon Total Hadronic Cross Section**

575 This section outlines the importance of the pion-argon total hadronic cross section in
576 the context of the current and upcoming liquid argon neutrino experiments, SBN and
577 DUNE. We describe the signal signature and historic measurements of pion-nucleus

578 cross section, as well as the implementation of these cross sections in the current
579 version of the simulation package used by LArIAT.

580 **π^- Ar Cross Section in the Context of Neutrino Searches**

581 As outlined in 1.2.3, neutrino experiments use the products of neutrino interactions
582 to identify the energy and flavor of the incoming neutrino. Pions are a common
583 product of neutrino interaction, especially in resonant scattering, DIS and coherent
584 pion production. For neutrino experiments in argon, there are two main reasons
585 why understanding pion hadronic interactions with argon is important: to model the
586 behavior of the pion inside the target nucleus and to model the behavior of the pion
587 during its propagation inside the detector medium.

588 Assumptions on the nuclear modeling and on the interaction of hadrons inside the
589 nucleus performed at the level of the neutrino event generator bridge the measure-
590 ment of the products of a neutrino interaction to the reconstruction of the neutrino
591 energy and flavor. Thus, understanding pion hadronic interactions with the nucleus is
592 particularly important to model correctly resonant, DIS and coherent pion production
593 in neutrino interactions. For example, in case of resonant scattering,

$$\nu_l + N \rightarrow l + \Delta/N^* \rightarrow l + \pi + N', \quad (1.16)$$

594 the Δ and N^* and excited states will decay hadronically in matters of $\sim 10^{-24}$ s
595 inside the nucleus producing pions which will have many chances to re-interact
596 as they exit the target medium. The decay modes for the lower mass Δ (1232) and
597 $N^*(1440)$ are listed in table 1.3.

598 The key elements of a neutrino event generators for resonance and DIS events
599 are the nuclear model and the hadron treatment (both production and transporta-
600 tion). We illustrate here the conceptual basis of the GENIE Neutrino Generator [18]

601 as an example, since GENIE is one the most popular event generators for liquid ar-
602 gon experiments. For example, the nuclear model used by GENIE for all processes
603 is a Relativistic Fermi Gas (RFG) model modified to incorporate nucleon-nucleon
604 correlations [30]. This means that the initial momentum and binding energy of the
605 struck nucleon is determined by assuming nucleons inside the nucleus are quasi-free,
606 acting independently in the mean field of the nucleus. For $A > 20$ such as argon, the
607 2-parameter Woods-Saxon shell model for density function is used. The GENIE mod-
608 ule INTRANUKE [85] is used to simulate final-state interactions (FSI) which model
609 hadron re-interactions inside the nucleus. This module places the outgoing parti-
610 cles in the nucleus and propagates them using the “hA model”. In the INTRANUKE
611 hA model, hadrons can undergo at most one FSI per event. When possible, external
612 hadron-nucleus scattering data are used to tune INTRANUKE. Since no data is avail-
613 able for Argon, GENIE uses an interpolation of data from heavier and lighter nuclei
614 for the pion-argon cross section leading to large (10?s of %) resultant uncertainties in
615 the INTRANUKE module.

616 Once the pion has left the target nucleus, the pion-argon hadronic cross section also
617 plays an important role in the pion transportation inside the argon medium: processes
618 such as pion absorption or pion charge exchange can greatly modify the topology of
619 a neutrino interactions in the detector and lead to significant modifications in the
620 event classification. Being able to reconstruct the details of pions inside the detector
621 is an imperative for modern liquid argon neutrino experiment to achieve the design
622 resolution for their key physics measurements.

623 π^- -Ar Hadronic Interaction: Signal Signatures

624 Strong hadronic interaction models [49, 70] predict the pion interaction processes with
625 argon in the [100 - 1200] MeV energy range. The total hadronic π^- -Ar interaction
626 cross section is defined as the one related to the single process driven only by the

627 strong interaction which is dominant in the considered energy range. In measuring
628 the “total” cross section, we include both the elastic and reaction channels, regardless
629 of the final state,

$$\sigma_{Tot} = \sigma_{Elastic} + \sigma_{Reaction}; \quad (1.17)$$

630 the reaction channel is further characterized by several exclusive channels with defined
631 topologies,

$$\sigma_{Reaction} = \sigma_{Inelastic} + \sigma_{abs} + \sigma_{chex} + \sigma_{\pi prod}. \quad (1.18)$$

632 A summary of the pion final states in order of pion multiplicity for the reaction
633 channel is given in table 1.4. Pion capture and pion decay at rest dominate the
634 cross section under 100 MeV. We define pion capture as the process determining the
635 formation of a pionic atom and the subsequent pion’s end of life. Stopping negative
636 pions can form pionic argon, where the negative pion plays the role of an orbital
637 electron. Since the pion mass is two orders of magnitude greater than the electron
638 mass, the spatial wave form of the pion will overlap more with the nucleus compared
639 to the electron case. After the electromagnetic formation of the pionic atom, the
640 pion will get quickly absorbed by the nucleus, which is put in an excited state. The
641 nucleus then de-excites with the emission of low energy nucleons and photons. Pion
642 capture is dominant compared to pion decay, the other important process for very
643 low energy pions. The decay of a pion is governed by the weak force; the pion decay
644 life time is $\tau_\pi = 2.6 \times 10^{-8}$ s and the main decay mode is $\pi^- \rightarrow \mu^- + \bar{\nu}_\mu$ (BR 99.98%).
645 Since pion capture can be considered an electromagnetic process and pion decay is a
646 weak process, this energy region is purposely excluded from the hadronic cross section
647 measurement.

648 **Previous measurements: Lighter and Heavier Nuclei**

649 Many experiments with pion beams have studied the hadronic interaction of pions on
650 light and heavy materials, such as He, Li, C, Fe, Pb [36]. However, data on argon are
651 rare: the total differential hadronic cross section has never been measured before on
652 argon. Simulation packages such as Geant4 base their pion transportation for argon
653 on data from lighter and heavier nuclei: the goal of LArIAT’s dedicated measurement
654 on argon is to bridge this gap in data, thus reducing the uncertainties related to pion
655 interactions in argon in both neutrino event generators and in simulation packages of
656 pion transportation.

657 The shape of the pion-nucleus interaction cross section in the energy range con-
658 sidered shows the distinct features indicating the presence of a resonance. In fact, the
659 mean free path of a pion of kinetic energy between 100 and 400 MeV is much shorter
660 than the average distance between nucleons (which is of the order of 1 fm). There-
661 fore, the pion interacts with surface nucleons. A Δ resonance is often produced in
662 the interaction, which subsequently decays inside the nucleus. Experimental results
663 on several nuclei as reported in [36] are shown in Figure 1.3; it is interesting to notice
664 here how the shape of the Δ resonance becomes less pronounced as a function of the
665 mass number of the target nucleus. Pion interactions with heavier nuclei also shift the
666 peak of the resonance at lower energy; this effect is due to kinematic considerations
667 and to the difference in propagation of the Δ inside the nucleus. Multiple scattering
668 effect modify the resonance width, which is larger than the natural-decay width. As
669 an example of a fairly well studied target, Figure 1.4 reports the negative pion cross
670 section on Carbon for the elastic and reaction² channels, and their sum [55].

2. This paper calls “inelastic interaction” what we refer as to “reaction channel”.

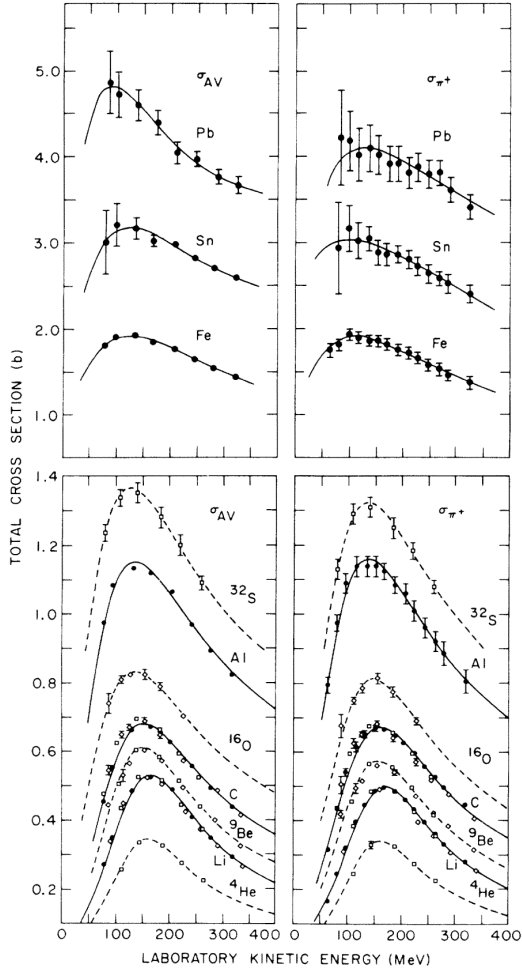


Figure 1.3: Pion-nucleus total cross sections: σ_{π^+} for positive pions (right) and σ_{AV} (left) for the average between positive and negative pions $\sigma_{AV} = \frac{\sigma_{\pi^+} + \sigma_{\pi^-}}{2}$ in the Δ resonance region. The error bars include estimates of systematic uncertainties. The curves are the results of fits to the data assuming a Breit-Wigner shape. This summary plot is reported in [36] and uses data from [52, 117].

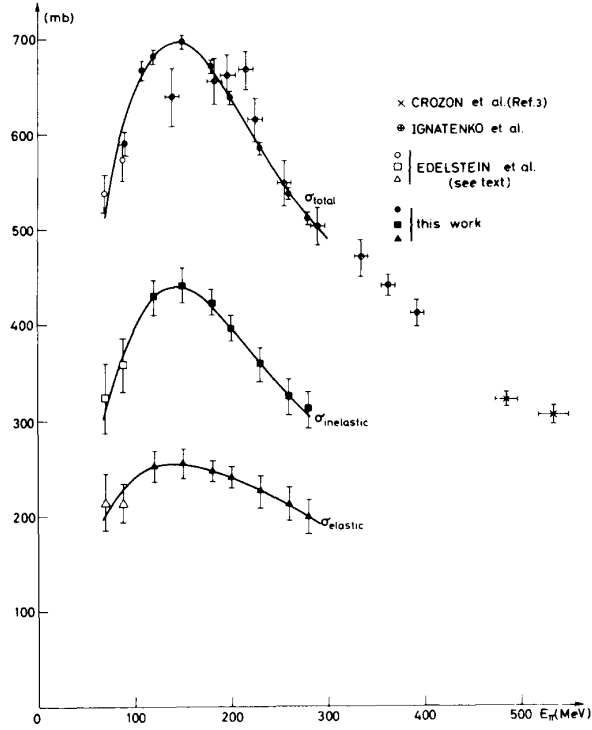


Figure 1.4: Negative pion nucleus total, elastic and reaction cross sections on ^{12}C as from [55].

671 Negative Pion Interaction Cross Section in Simulation Packages

672 LArIAT uses Geant4 as the default simulation package. In particular, pions (and
 673 kaons) transportation is achieved through the Geant4 FTFP_BERT physics list. In
 674 this physics list, Geant4 uses the Bertini cascade model [118] to simulate the products
 675 of the pion-nucleus interaction as well as secondary hadronic re-interactions inside
 676 the target nucleus (intra-nuclear cascade). The target nucleus is represented as a
 677 continuous gas where the nuclear potential follows concentrical shells whose depths
 678 approximate the Woods-Saxon shape. The CERN-HERA compilations [114, 115] of
 679 hadron-nucleon interaction data is the data base used for the decision making process
 680 after the cascade is invoked. The cross section model determines if the pion inter-
 681 acts, the eventual type of interaction and the interaction multiplicity. For hadron
 682 projectiles with energy less than 20 GeV, Geant4 reports the uncertainty on the cross

683 section model to be about the size of the error bars on the data used, or about 10%,
684 increasing to 20-30% in energy regions where data is sparse.

685 The relevance of the GENIE generator for neutrino physics and its basic working
686 principles have been outlined earlier in this section. Given GENIE’s modularity,
687 information on hadron-nucleus interactions can be extracted from the INTRANUKE
688 module and directly compared against the Geant4 predictions. The work in [98]
689 reviews the current status of negative and positive pion simulation in Geant4 and
690 GENIE for ^{12}C , ^{56}Fe , and ^{40}Ca . From that work, we report the results for ^{12}C in
691 Figure 1.5 as it allows a direct comparison between Geant4, GENIE and and pion
692 re-scattering data. Geant4 predictions for π^- on Carbon are in good agreement with
693 data over the entire spectrum spectrum, while GENIE predictions seem to show some
694 features at around 500 MeV and 900 MeV, maybe due to higher resonances in the hA
695 model. From the same work, we also report the negative pion cross section on ^{40}Ca
696 in Figure 1.6, since this is the nuclear medium closest to argon. The predictions from
697 both Geant4 and GENIE agree with data in the high energy region; the Geant4 and
698 GENIE predictions diverge in the resonance region, where data is not available. These
699 few examples highlight how cross section data for the specific nucleus considered in
700 the neutrino experiments is fundamental to inform the Monte Carlo simulation.

701 For the LArIAT simulation of the MC sample used in the π^- argon total hadronic
702 cross section measurement we use the Geant4 Bertini Cascade model, whose predic-
703 tions for the total, elastic and reaction hadronic cross sections are show in Figure
704 1.7.

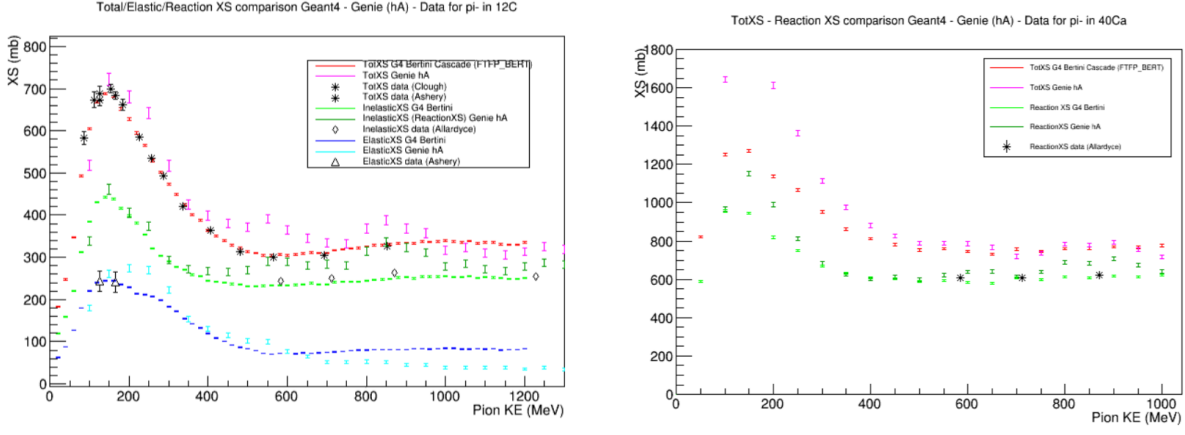


Figure 1.5: Total, elastic and reaction cross section for π^- on ^{12}C . Comparison between results from Geant4 simulation (Bertini cascade model), Genie simulation (hA model), and experimental data [22, 52, 53, 109].

Figure 1.6: Total, elastic and reaction cross section for π^- on ^{40}Ca . Comparison between results from Geant4 simulation (Bertini cascade model), Genie simulation (hA model), and experimental data [53].

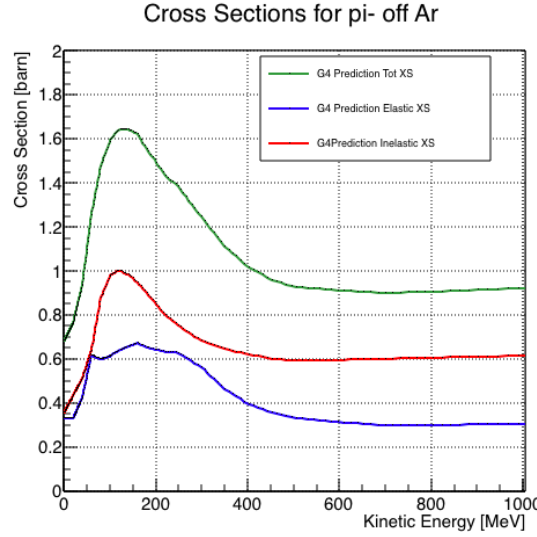


Figure 1.7: Total, elastic and reaction hadronic cross section for π^- -argon implemented in Geant4 10.01.p3.

Resonance	Decay Mode	Lifetime (s)
Δ (1232) $3/2^+$	$\Delta^{++}(\text{uuu}) \rightarrow p\pi^+$ $\Delta^+(\text{uud}) \rightarrow n\pi^+$ $\Delta^+(\text{uud}) \rightarrow p\pi^0$ $\Delta^0(\text{udd}) \rightarrow n\pi^0$ $\Delta^0(\text{udd}) \rightarrow p\pi^-$ $\Delta^-(\text{ddd}) \rightarrow n\pi^-$	$\sim 5.6 \times 10^{-24}$
N^* (1440) $1/2^+$	$N^* \rightarrow N\pi$ $N^* \rightarrow N\pi\pi$	$\sim 2.2 \times 10^{-24}$

Table 1.3: Main decay modes of the lightest Delta resonance and Nucleon excited state.

N π in FS	Channel Name	Reaction	Notes
0	Pion Absorption, σ_{abs}	$\pi^-(np) \rightarrow nn$ (2-body abs) $\pi^-(nnp) \rightarrow nnn$ (3-body abs) $\pi^-(npp) \rightarrow pnn$ (3-body abs) $\pi^-(nnpp) \rightarrow pmn$ (Multi-body abs)	Suppressed on single nucleon by energy conservation: the process occurs on at least two nucleons system.
1	Elastic Scattering, σ_{el}	$\pi^- + N \rightarrow \pi^- + N$	Scattering on nucleon or nucleus, the target is left in ground state
1	Charge Exchange, σ_{chea}	$\pi^- + p \rightarrow \Delta^0 \rightarrow \pi^0 + n$ $\pi^- + N \rightarrow \pi^+ +$ nucleons	Single charge exchange: charged pion converts into neutral pion Double charge exchange: charged pion converts into opposite charge pion
1	Inelastic Scattering, σ_{inel}	$\pi^- + p \rightarrow \Delta^0 \rightarrow \pi^- + p$ (knock-out) $\pi^- + n \rightarrow \Delta^- \rightarrow \pi^- + n$ (knock-out)	Other possible reactions: Pure Inelastic scattering: population of low energy bound excited states Nuclear break-up with nucleons or fragments knock-out
2+	Pion Production, $\sigma_{\pi prod}$	$\pi^- + N \rightarrow \geq 2\pi +$ nucleons	Possible if pion K.E ≥ 500 MeV/c

Table 1.4: Summary of negative pion hadronic interactions of the reaction channel as a function of the pion multiplicity in the final state in the energy range [100-1200] MeV.

705 **1.4.2 Kaon-Argon Total Hadronic Cross Section**

706 This section outlines the importance of the kaon-argon total hadronic cross section.
707 We start by discussing the measurement in the context of nucleon decay searches. We
708 then describe the signal signature and historical measurements of kaon-nucleus cross
709 section, as well as the implementation of this cross sections in the current version of
710 the simulation package used by LArIAT.

711 **K⁺Ar Cross section in the Context of Nucleon Decay Searches**

712 Baryon number is accidentally conserved in the Standard Model. Even though no
713 baryon number violation has been experimentally observed thus far, no underlying
714 symmetry in line with the Noether paradigm [97] explains its conservation. As shown
715 in section 1.3.2, almost all Grand Unified Theories predict at some level baryon num-
716 ber violation in the form of nucleon decay on long time-scales. Given the impossibil-
717 ity to reach grand unification energy scales with collider experiments (Energy Scale
718 $> 10^{15}$ GeV), an indirect proof of GUTs is needed. The experimental observation of
719 nucleon decay may be the only viable way to explore these theories.

720 In case of nucleon decay discovery, the dominant decay mode may uncover addi-
721 tional information about the GUT type. Supersymmetric GUTs [24, 46] prefer the
722 presence of kaons in the products of the decay, e.g. $p \rightarrow K^+ \bar{\nu}$ (see fig 1.8, left).
723 Gauge mediated GUTs, in which new gauge bosons are introduced that allow for the
724 transformation of quarks into leptons, and vice versa, prefer the mode $p \rightarrow e^+ \pi^0$ (see
725 fig 1.8, right).

726 LArIAT tiny active volume makes it impossible for the experiment to place com-
727 petitive limits on nucleon decay searches. However, LArIAT provides excellent data
728 to characterize kaons in liquid argon for the ‘‘LAr golden mode’’, $p \rightarrow K^+ \bar{\nu}$. The
729 result of these studies will affect future proton decay searches in LArTPCs. Previous
730 work has been done to assess the potential identification efficiency for different decay

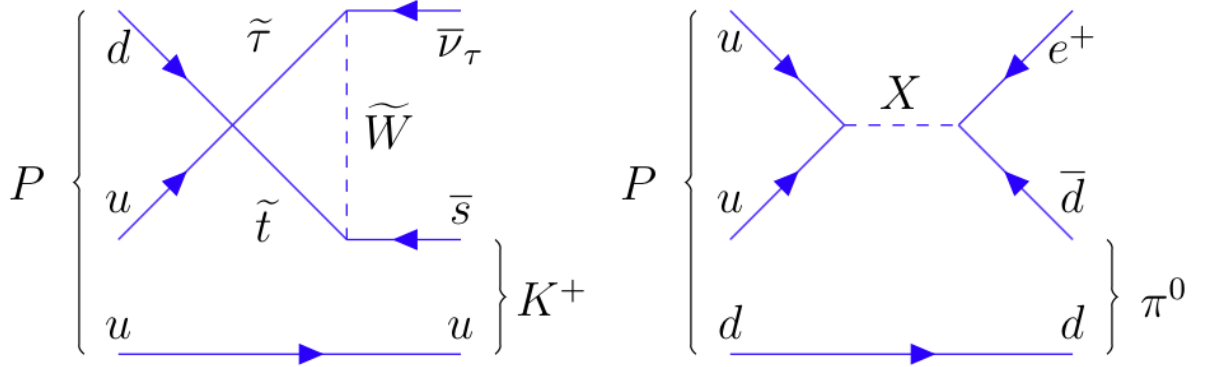


Figure 1.8: Feynman diagrams for proton decay “golden modes”: $p \rightarrow K^+\bar{\nu}$ for supersymmetric GUTs on the left and $p \rightarrow e^+\pi^0$ for gauge-mediated GUTs on the right.

731 modes in a LArTPC [51], but, as the time of this writing, no study of kaon selection
 732 efficiency in LArTPCs has been performed on data. The K^+ -Ar interaction cross
 733 section has never been measured before and can affect the possibility of detecting
 734 and measuring kaons when produced in a proton decay event. Kaon interactions with
 735 argon can distort the kaon energy spectrum as well as change the topology of single
 736 kaon events. In a LArTPC, non-interacting kaons appear as straight tracks with a
 737 high ionization depositions at the end (Bragg peak). The topology of interacting
 738 kaons can be quite different. In case of elastic scattering, a distinct kink will be
 739 present in the track. In case of inelastic scattering the Bragg peak will not be present
 740 and additional tracks will populate the event. Performing the total hadronic K^+ -Ar
 741 cross section measurement on data serves the double purpose of identifying the rate
 742 of “unusual” topologies (kinks and additional tracks) and of developing tools for kaon
 743 tracking in LAr.

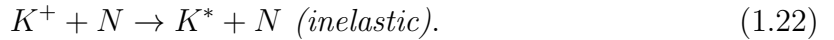
744 **K^+ Ar Hadronic Interaction: Signal Signatures**

The interaction of a mildly relativistic charged kaon with an argon nucleus is determined largely by the strong force. The total hadronic K^+ -Ar interaction cross section

is defined as the one related to the single (hadronic) process driven only by the strong interaction. In this case, “total” indicates all strong interactions regardless of the final state. This condition purposefully includes both elastic and inelastic (reaction) channels. Indeed, the total cross section section can be then decomposed into

$$\sigma_{Tot} = \sigma_{Elastic} + \sigma_{Reaction}.$$

745 For the LArIAT cross section analysis, the kaons considered span a momentum
746 inside the TPC from 100 MeV/c to 800 MeV/c. In this energy range, the relevant
747 K-Nucleon interactions are according to [63]:



748 **Previous Measurements: Lighter and Heavier Nuclei**

749 In general, measurements on kaon cross sections are extremely scarce. The mea-
750 surement of the kaon interaction cross section would bring the additional benefit
751 of reducing the uncertainties associated with hadron interaction models adopted in
752 MC simulations for argon targets, beneficial for both proton decay studies and kaon
753 production from neutrino interaction studies, where the uncertainties for final state
754 interaction models are big [47].

755 Figure 1.9 shows a 1997 measurement on several elements as performed by Fried-
756 mann et al. [65]. As a reference, this paper measures a σ_{Tot} for Si of 366.5 ± 4.8
757 mb and a σ_{Tot} for Ca of 494.6 ± 7.7 mb at 488 MeV/c. The cross section for argon

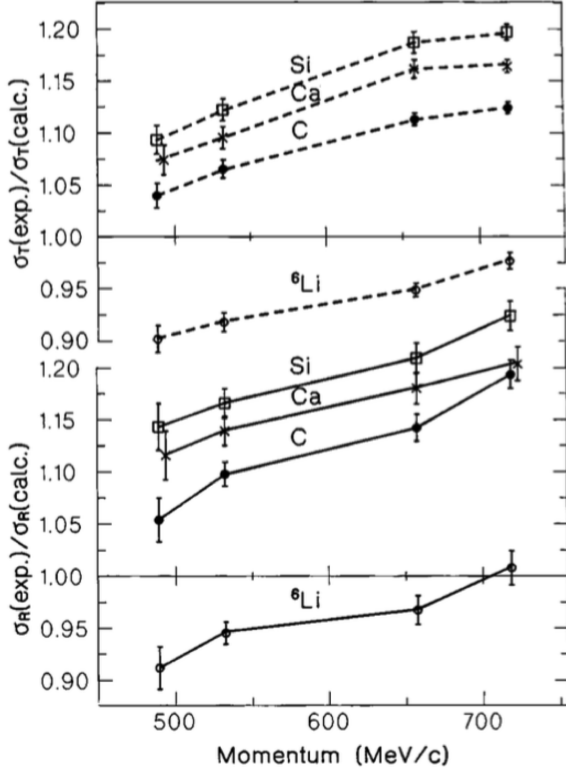


Figure 1.9: Ratios between experimental and calculated cross sections as from [65].
Top: Total cross sections.
Bottom: reaction cross sections.

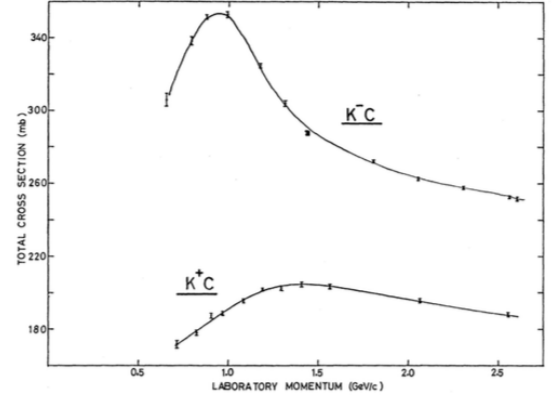


Figure 1.10: Total K^+ and K^- cross sections on carbon as from [32].

is expected to lie in between these two measurements. Additional data on the kaon cross section are provided by Bugg et al. [32]. Bugg performs a measurement of the total K^+ and K^- cross sections on protons and deuterons over the range of 0.6-2.65 GeV/c, as well as a measurement of the total K^+ and K^- cross sections on carbon for a number of momenta; the results of this paper on carbon are reported in Figure 1.10.

764 Kaon Interaction Cross Section for thin target in Geant4

Since the kaon cross section in argon has never been measured before, simulation packages tune kaon transportation in argon by extrapolation from lighter and heavier nuclei. LArIAT uses the Geant4 suite for particle transportation. Since kaon data on

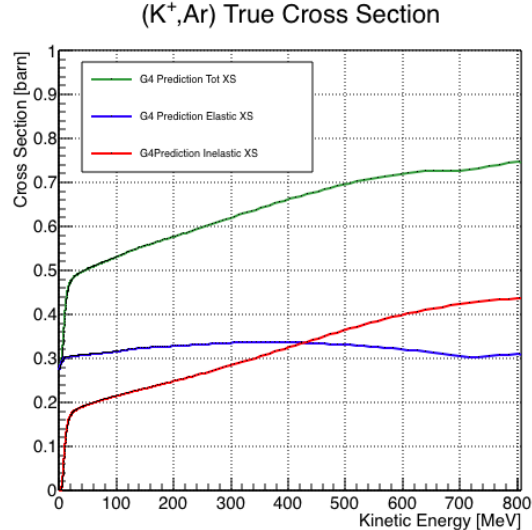
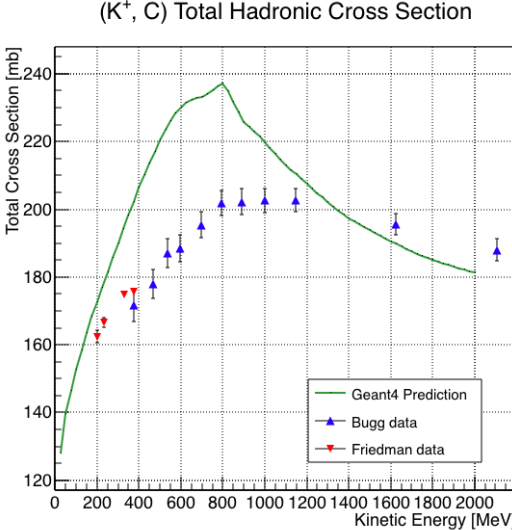


Figure 1.11: Total hadronic cross section for carbon implemented in Geant4 10.01.p3 with overlaid with the Bugg and Frideman data.

Figure 1.12: Total, elastic and reaction hadronic cross section for K^+ -argon implemented in Geant4 10.01.p3.

carbon are available, we used it as a metric to evaluate the Geant4 prediction performances. Figure 1.11 shows the total hadronic cross section for carbon implemented in Geant4 10.01.p3 overlaid with the Bugg and Friedman data. Unfortunately, version 10.01.p3³ of Geant4, which is the version used for the simulation in this work, does not reproduce the data for carbon closely. On one hand, this evidence makes us even more wary when using the Monte Carlo in simulating the kaon-argon interactions. On the other, it further highlights the importance of the kaon measurement. For the LArIAT simulation of the MC sample used in the K^+ argon total hadronic cross section measurement we use the Geant4 Bertini Cascade model, whose predictions for the total, elastic and reaction hadronic cross sections are show in Figure 1.12.

3. It should be noted that the latest Geant4 version, 10.03.p3, uses a different parametrization for the kaon cross section and retrieves a better agreement with data.

778 Chapter 2

779 **Liquid Argon Detectors at the** 780 **Intensity Frontier**

781 “*Don’t you know, honey,*
782 *Ain’t nobody ever gonna love you, the way I try to do?*”
783 – Janis Joplin, 1971 –

784 In the next few years, LArTPCs will be the tools to answer some of the burning
785 questions in neutrino physics today. This chapter illustrates the operational principles
786 of this detector technology, as well as the scope of the key detectors in the US liquid
787 argon program – SBN, DUNE and LArIAT.

788 **2.1 The Liquid Argon Time Projection Chamber** 789 **Technology**

790 In this section, we outline an extremely brief history of Time Projection Chambers
791 as particle detectors, focusing on their incarnation as Argon detectors for neutrino
792 physics. We further describe the working principles of Liquid Argon Time Projection

793 Chambers, leading to the description of the event reconstruction in LArTPC.

794 2.1.1 TPCs, Neutrinos & Argon

795 David Nygren designed the first Time Projection Chamber (TPC) in the late 1970s [99]
796 for the PEP-4 experiment, a detector apt to study electron-positron collisions at the
797 PEP storage ring at the SLAC National Accelerator Laboratory. From the original
798 design in the seventies – a cylindrical chamber filled with methane gas – the TPC
799 detector concept has seen many incarnations, the employment of several different
800 active media and a variety of different particle physics applications, including, but
801 not limited to the study of electron/positron storage rings (e.g. PEP4, TOPAZ,
802 ALEPH and DELPHI), heavy ions collisions in fixed target and collider experiments
803 (e.g. EOS/HISSL and ALICE), dark matter (ArDM), rare decays and capture (e.g.
804 TRIUMF, MuCap), neutrino detectors and nucleon decay (ICARUS, SBN, DUNE),
805 and neutrino less double beta decay (Next). A nice review of the history of TPCs
806 and working principles is provided in [78].

807 Several features of the TPC technology make these detectors a more versatile tool
808 compared to other ionization detectors and explain such a wide popularity. TPCs are
809 the only electronically read detector which deliver simultaneous three-dimensional
810 track information and a measurement of the particle energy loss. Leveraging on both
811 tracking and calorimetry, particle identification (PID) capabilities are enhanced over
812 a wide momentum range.

813 Historically, the active medium in ionization detectors has been in the gaseous
814 form. Carlo Rubbia first proposed the use of a Liquid Argon TPC for a neutrino
815 experiment, ICARUS [108], in 1977. Using nobles elements in the liquid form for
816 neutrino detectors is advantageous for several reasons. The density of liquids is \sim 1000
817 times greater than gases, augmenting the number of targets for neutrino's interaction
818 in the same volume, in a effort to balance the smallness of neutrino cross section. Since

Element	LAr	LXe
Atomic Number	18	54
Atomic weight A	40	131
Boiling Point Tb at 1 atm	87.3 K	165.0 K
Density	1.4 g/cm ³	3.0 g/cm ³
Radiation length	14.0 cm	2.8 cm
Moliere Radius	10.0 cm	5.7 cm
Work function	23.6 eV	15.6 eV
Electron Mobility at $E_{field} = 10^4$ V/m	0.047 m ² /Vs	0.22 m ² /Vs
Average dE/dx MIP	2.1 MeV/cm	3.8 MeV/cm
Average Scintillation Light Yield	40000 γ /MeV	42000 γ /MeV
Scintillation λ	128 nm	175 nm

Table 2.1: LAr, LXe summary of properties relevant for neutrino detectors.

the energy loss of charged particle is proportional to the target material density, as shown in the Bethe-Block equation (eq. 2.1), the increased density reflects into a proportionally higher energy loss, enhancing the calorimetry capability of detectors with a liquid active medium. Additionally, the ionization energy of liquids is smaller than gasses by the order of tens of eV. Thus, at the passage of charged particles, liquids generally produce more ionization electrons than gases for the same deposited energy, forcing the particles to deposit more energy in a shorter range. The downside of using noble liquid elements in experiments is that they require expensive cryogenic systems to cool the gas until it transitions to its the liquid form. The properties of liquid argon in comparison liquid xenon – a popular choice for dark matter and neutrinoless double beta decay detectors – are summarized in table 2.1. Albeit xenon would be more desirable than argon given some superior properties such as lower ionization energy and higher density and light yield, argon relative abundance abates the cost of argon compared to xenon, making argon a more viable choice for the construction of ton (and kilo-ton) scale neutrino detectors.

LArTPCs are some times referred as to “electronic” bubble-chambers, for the similarity in the tracking and energy resolution which is coupled with an electronic readout of the imaging information in LArTPCs. Compared to these historic detectors

837 however, LArTPC bestow tridimensional tracking and a self triggering mechanism
838 provided by the scintillation light in the liquid argon. An event display of a ν_μ CC
839 interaction candidate in the MicroBooNE detector is shown in picture 2.1 to display
840 the level of spatial details these detectors are capable of; the color scale of the image
841 is proportional to the energy deposited, hinting to these calorimetry capabilities of
the detectors.

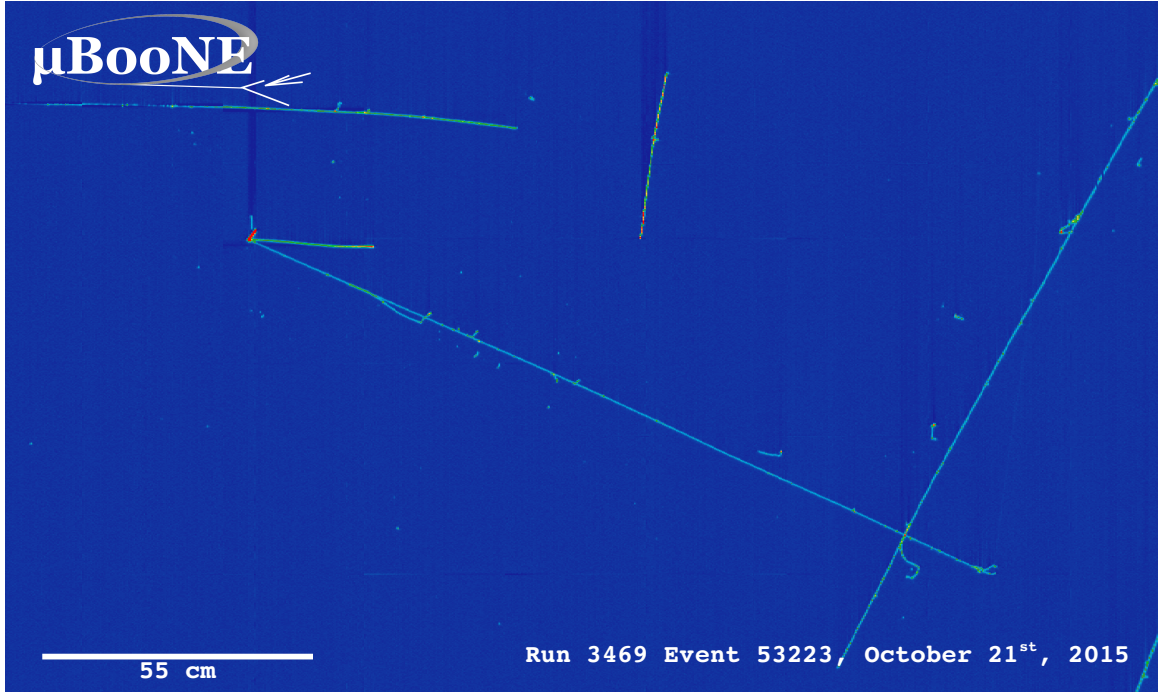


Figure 2.1: Event display of a ν_μ CC interaction candidate in the MicroBooNE detector.

842

843 2.1.2 LArTPC: Principles of Operation

844 To the bare bones, a LArTPC is a bulk of liquid argon sandwiched in a flat capacitor,
845 equipped with a light collection system, as the cartoon in 2.2 shows. A uniform
846 electric field of the order of 500 V/cm is maintained constant between the faces of the
847 capacitor. The anode is sensitive to ionization charge and it is usually made of two
848 or more planes segmented into several hundreds parallel sense wires a few millimeters
849 apart; different geometries for the anode segmentation are under study [48].

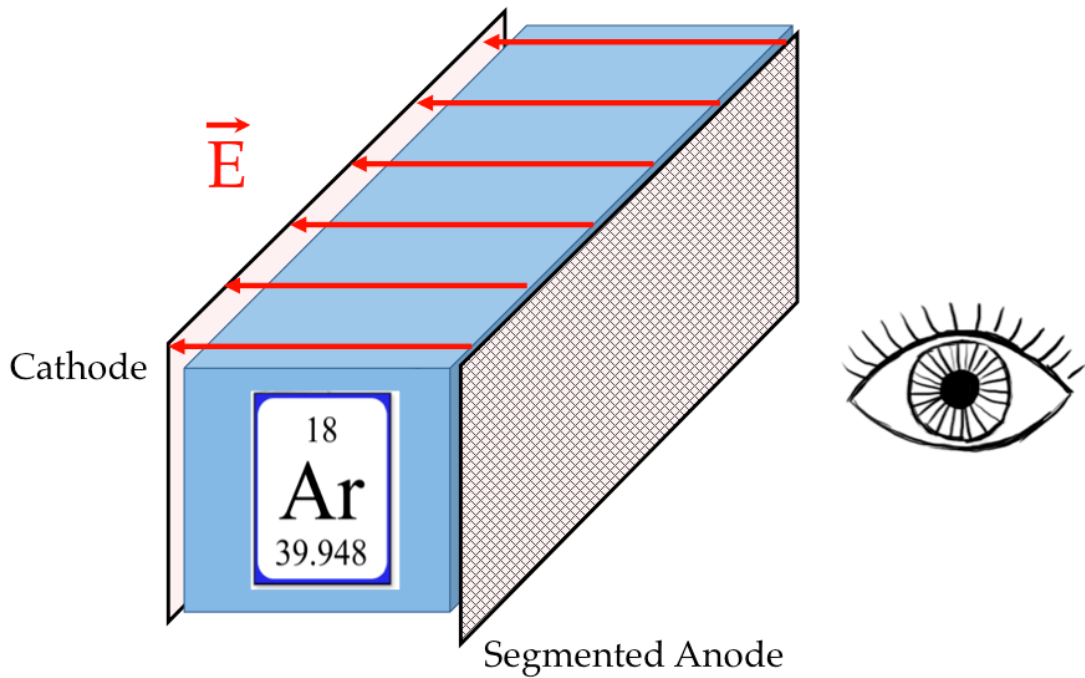


Figure 2.2: A cartoonish sketch of a LArTPC.

Argon ionization and scintillation are the processes leveraged to detect particles in the LArTPC active volume. When a ionizing radiation traverses the argon active volume it leaves a trail of ionization electrons along its trajectory and it excites the argon producing scintillation light – details on the production and detection of ionization charge and scintillation light are provided in 2.1.4 and 2.1.4 respectively. The optical detector sees the argon scintillation light in matters of nanoseconds. This flash of light determines the start time of an event in the chamber, t_0 . The uniform electric field drifts the ionization electrons from the production point towards the anode in order of hundreds of microseconds or more depending on the chamber dimensions¹. The anode sense wires see either an induced current by the drifting ionization charge (on induction planes) or an injection of such charge (collection

1. The ionized argon also drifts, but in the opposite directions compared to the electrons. Since the drift time is proportional to the particle mass, the ions' drift time is much longer than the electrons'. Ionized argon is collected on the cathode which is not instrumented, so it is not used to infer information about the interactions in the chamber.

861 plane). An appropriate choice of the voltage bias on each wire plane assures ideal
862 charge transparency, so that all the ionization charge is collected on the collection
863 plane and none on the induction planes.

864 The arrival time of the charge on the anode sense wires is used to measure the
865 position of the original ionizing radiation in the drift direction. In fact, since the
866 constant electric field implies that the drift velocity is also constant, the position of
867 the original ionization is simply given by the multiplication of the drift velocity by the
868 drift time, where the “drift time” is the difference between t_0 and the charge arrival
869 time on the wire planes. The spacial resolution on this dimension is limited by the
870 time resolution of the electronics or by longitudinal diffusion of the electrons. The
871 spatial information on the different wire planes maps a bi-dimensional projection of
872 the interaction pattern in the plane perpendicular to the drift direction. The spacial
873 resolution on this dimension is limited by the transverse electron diffusion in argon
874 and by the grain of the anode segmentation, i.e. the spacing between the wires in
875 the sense planes [45]. The off-line combination of the 2-D information on the wire
876 planes with the timing information allows for the 3D reconstruction of the event in
877 the chamber.

878 Since the charge deposited by the ionizing radiation is proportional to the de-
879 posited energy and the charge collected on the sense plane is a function of the de-
880 posited charge, LArTPCs allow the measurement of the energy deposit in the active
881 volume. Effects due to the presence of free charge and impurities in the active vol-
882 ume, such as a finite electron lifetime, recombination and space charge, complicate
883 the relationship between deposited and collected charge affecting the measurement of
884 the particle’s energy, as described in the next section.

885 **2.1.3 Liquid Argon: Ionization Charge**

886 The mean rate of energy loss by moderately relativistic elementary charge particles
 887 heavier than electrons is well described by the modified Bethe-Bloch [102] equation

$$-\frac{dE}{dx} = K z^2 \frac{Z}{A} \varrho \frac{1}{\beta^2} \left[\frac{1}{2} \ln \frac{2m_e c^2 \beta^2 \gamma^2 T_{max}}{I^2} - \beta^2 - \frac{\delta}{2} \right], \quad (2.1)$$

888 where z is the number of unit charge of the ionizing radiation, Z , A and ϱ are the
 889 atomic number, mass number and density of the medium, m_e is the electron mass,
 890 $\gamma = \frac{\beta}{\sqrt{1-\beta^2}}$ is the Lorentz factor of the ionizing radiation, T_{max} is the maximum kinetic
 891 energy which can be imparted to a free electron in a single collision, I is the mean
 892 excitation energy on eV, δ is the density correction and $K = 0.307075 \text{ MeV g}^{-1} \text{ cm}^2$ is
 893 a numerical conversion factor. The Bethe-Bloch treats the energy loss by an ionizing
 894 radiation via quantum-mechanical collisions producing ionization or an excitation in
 895 the medium as an uniform and continuous process. The density correction terms
 896 becomes relevant for incident particle with high energy, where screening effects due
 897 to the polarization of the medium by high energy particles occur.

898 Excitation and ionization of the detector medium occur in similar amounts. Since
 899 the ionizing collisions occur randomly, we can parametrize their number k in a segment
 900 of length s along the track with a Poissonian function

$$P(k) = \frac{s^k}{k! \lambda^k} e^{-s/\lambda}, \quad (2.2)$$

901 where $\lambda = 1/N_e \sigma_i$, with N_e being the electron density of σ_i the ionization cross-
 902 section per electron. About 66% of the ionizing collisions in Argon produce only
 903 a single electron/ion pair [78]; in the other cases, the transferred kinetic energy is
 904 enough for the primary electron to liberate one or more secondary electrons, which
 905 usually stay close to the original pair. Occasionally, electrons can receive enough

906 energy to be ejected with high energy, forming a so-called “ δ -ray”: a detectable short
907 track off the particle trajectory, as shown in figure 2.3. The average number of δ -ray
908 with energy $E > E_0$ per cm follows the empirical form

$$P(E > E_0) \sim \frac{y}{\beta^2 E_0}, \quad (2.3)$$

909 where y is an empirical factor depending on the medium (0.114 for gaseous Ar), and
910 β is v/c .

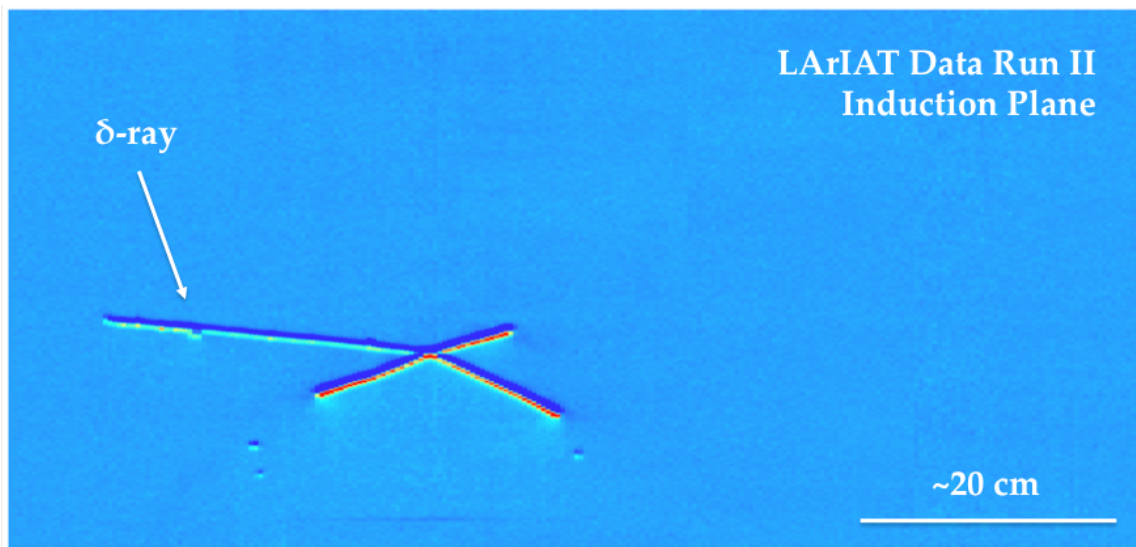


Figure 2.3: Events display for a LArIAT pion absorption candidate on the induction plane, with highlighted delta ray.

911 Purity & Electron Life Time

912 The presence of electronegative contaminants in liquid argon, such as oxygen O_2
913 and water H_2O , is particularly pernicious, since these molecules quench the charge
914 produced by the ionizing radiation. Thus, amount of charge per unit of length dQ/dx
915 collected on the collection plane depends on the charge's production point in the
916 detector: ionization produced close to the cathode will see more impurities along its
917 journey to the collection plane than ionization produced close to the anode, resulting

in greater attenuation of its charge. As a result, the amount of charge collected on
 the sense wires as a function of the traveled distance follows an exponential decay
 trend. The traveled distance is generally measured in terms of drift time and the
 characteristic time constant of the exponential decay is called electron lifetime τ_e .
 Figure 2.4 shows the typical life time for LArIAT data. The procedure to measure
 the electron lifetime in LArIAT is outlined in [105]. LArIAT small drift distance (47
 cm) allows for a relatively short electron life time. The life time for bigger detectors
 such as MicroBooNE, whose drift distance is 2.6 m, needs to be of the order of
 tens of milliseconds to allow a charge collection usable for physics analyses. Energy
 reconstruction in LArTPC applies a correction for the finite lifetime to calibrate the
 detector calorimetric response; details for LArIAT are provided in Section B.

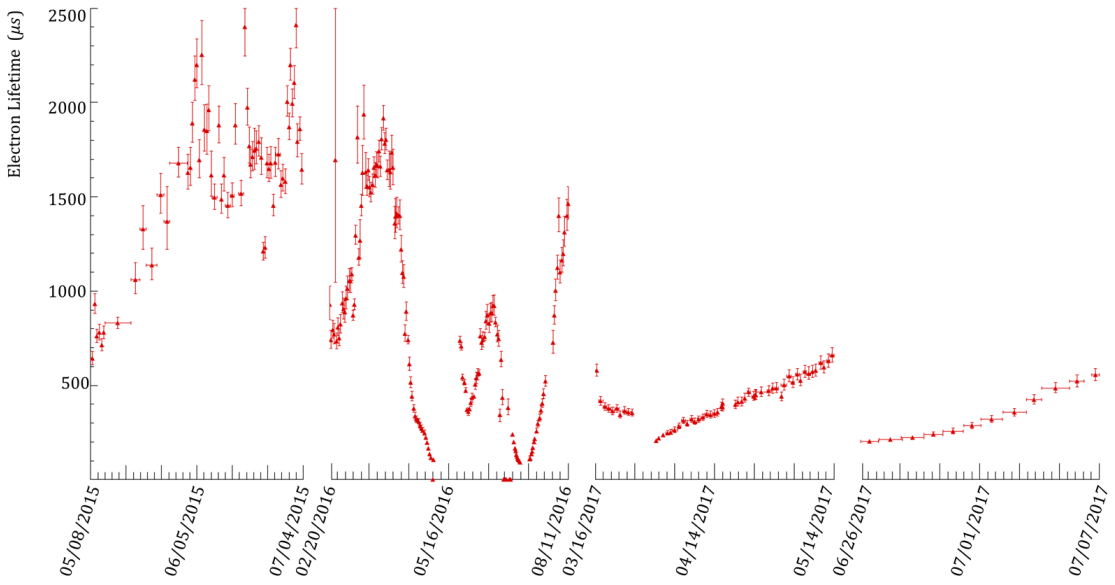


Figure 2.4: Electron lifetime during the LArIAT run period [43].

929 LArTPCs use hermetically sealed and leak-checked vessels to abate the leakage
930 and diffusion of contaminants into the system. The liquid argon filling of the volume
931 occurs after the vessel is evacuated or purged with gaseous argon [10] to reduce re-
932 maining gases in the volume. Even so, the construction of a pure tank of argon is
933 unviable, as several sources of impurity remain. In particular, impurities can come
934 from the raw argon supply, the argon filtration system and from the outgassing from
935 internal surfaces. Outgassing is a continuous diffusive process producing contami-
936 nants, especially water, even after the vessel is sealed, particularly from materials in
937 the ullage region². Since research-grade argon comes from the industrial distillation
938 of air, the impurities with the highest concentration are nitrogen, oxygen and water,
939 generally maintained under the 1 part per million level by the vendor. Even so, a
940 higher level of purity is necessary to achieve a free electron life time usable in meter
941 scale detectors. Thus, argon is constantly filtered in the cryogenic system, which
942 reduce the oxygen and water contamination to less than 100 parts per trillion. The
943 filtration system depends on the size and drift distance of the experiment and, for
944 experiments on several meters scale, it includes an argon recirculation system.

945 Recombination Effect

946 After production, ionization electrons thermalize with the surrounding medium and
947 may recombine with nearby ions. Recombination might occur either between the
948 electron and the parent ion through Coulomb attraction, as described in the geminate
949 theory [100], or thanks to the collective charge density of electrons and ions from
950 multiple ionizations in a cylindrical volume surrounding the particle trajectory, as
951 described in the columnar model [81]. Consideration on the average electron-ion
952 distance and the average ion-ion distance for argon show that the probability of

2. While the liquid argon low temperature reduces outgassing in the liquid, this process remains significant for absorptive material (such as plastic) above the surface of the liquid phase.

953 geminate recombination is low; thus recombination in argon is mainly due to collective
954 effects [5]. Since protons, kaons and stopping particles present a higher ionization
955 compared to MIPs, recombination effects are more prominent when considering the
956 reconstruction of energy deposited by these particles.

957 Theoretical descriptions of recombination based on the Birks model and the Box
958 model are provided in [29] and [113], respectively. The Birks model assumes a gaus-
959 sian spatial distribution around the particle trajectory during the entire recombina-
960 tion phase and identical charge mobility for ions and electrons. The Box model also
961 assumes that electron diffusion and ion mobility are negligible in liquid argon during
962 recombination. In these models, the fraction of ionization electrons surviving recom-
963 bination is a function of the number of ion-electron pairs per unit length, the electric
964 field, the average ion-electron separation distance after thermalization and the angle
965 of the particle with respect to the direction of the electric field – plus the diffusion
966 coefficient in the Birks model. Given the stringent assumptions, it is perhaps not sur-
967 prising that these models are in accordance to data only in specific regimes: the Birks
968 model is generally used to describe recombination for low dE/dx , the Box model for
969 high dE/dX . In LArTPC, the ICARUS and ArgoNeut experiments have measured
970 recombination in [16] and [5] respectively. Since LArIAT uses the refurbished Ar-
971 goNeut TPC and cryostat at the same electric field, LArIAT currently corrects for
972 recombination using the ArgoNeut measured recombination parameters in [5].

973 Space Charge Effect

974 Slow-moving positive argon ions created during ionization can build-up in LArTPC,
975 causing the distortion of the electric field within the detector. This effect, called
976 “space charge effect” leads to a displacement in the reconstructed position of the
977 signal ionization electrons. In surface LArTPCs the space charge effect is primarily
978 due to the rate of ionization produced by cosmic rays which is slowly drifting in the

979 chamber at all times. Surface LArTPC of the size of several meters are expected
980 to be modestly impacted from the space charge effect, where charge build-up create
981 anisotropy of the electric field magnitude of the order of 5% at a drift field of 500
982 V/cm [94]. The smallness of the LArIAT drift volume and its relatively high electric
983 field are such that the effect of space charge is expected to be negligible.

984 2.1.4 Liquid Argon: Scintillation Light

985 Liquid argon emits scintillation light at the passage of charged particles. LArTPCs
986 leverage this property to determine when the ionization charge begins to drift towards
987 the anode plane.

988 Scintillation Process

989 Scintillation light in argon peaks in the ultraviolet at a 128 nm, shown in comparison
990 to Xenon and Kypton in Figure 2.5, from [95]. The light yield collected by the optical
991 detector depends on the argon purity, the electric field, the dE/dx and particle type,
992 averaging at the tens of thousands of photons per MeV.

993 The de-excitation of Rydberg dimers in the argon is responsible for the scintillation
994 light. Rydberg dimers exist in two states: singlets and a triplets. The time constant
995 for the singlet radiative decay is 6 ns, resulting in a prompt component for the scin-
996 tillation light. The decay of the triplet is delayed by intersystem crossing, producing
997 a slow component with a time constant of ~ 1500 ns. “Self-trapped exciton lumines-
998 cence” and “recombination luminescence” are the two processes responsible for the
999 creation of the Rydberg dimers [84]. In the first process, a charged particle excites an
1000 argon atom which becomes self-trapped in the surrounding bulk of argon, forming a
1001 dimer; the dimer is in the singlet state 65% of the times and in the triplet state 35%
1002 of the times. In case of recombination luminescence, the charged particle transfers
1003 enough energy to ionize the argon. The argon ion forms a charged argon dimer state,

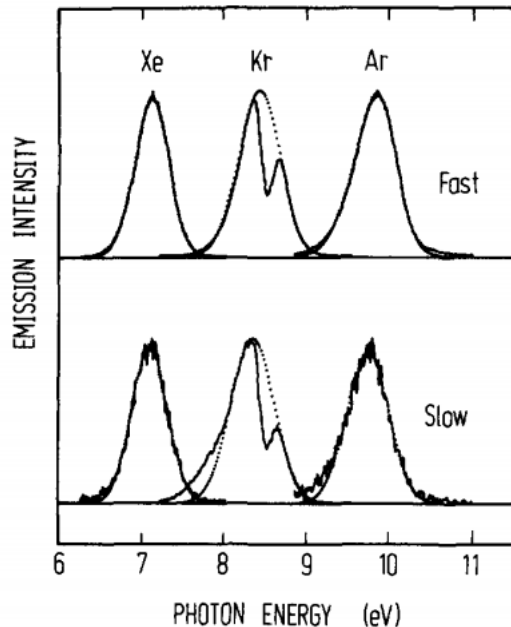


Figure 2.5: Emission spectra of the fast and slow emission components in Xenon, Krypton and Argon according to [95]. The dotted lines correspond to the Gaussian fits.

which quickly recombines with the thermalized free electron cloud. Excimer states are produced in the recombination, roughly half in the singlet and half in the triplet state. The light yield dependency on the electric field, on the dE/dx and particle type derives from the role of free charge in the recombination luminescence process. The spacial separation between the argon ions and the free electron cloud depends on the electric field. On one hand, a strong electric field diminishes the recombination probability, leading to a smaller light yield; on the other, it increases the free charge drifting towards the anode plane. Hence, the amount of measurable charge and light anti-correlates as a function of the electric field. Ionizing particles in the argon modify the local density of both free electrons and ions depending on their dE/dx . Since the recombination rate is proportional to the square of the local ionization density, highly ionizing particles boost recombination and the subsequent light yield compared to MIPs. The possibility to leverage this dependency for pulseshape-based particle identification has been shown in [31, 89].

1018 **Effects Modifying the Light Yield**

1019 The production mechanism through emission from bound excimer states implies that
1020 argon is transparent to its own scintillation light. In fact, the photons emitted from
1021 these metastable states are not energetic enough to re-excite the argon bulk, greatly
1022 suppressing absorption mechanisms. In a LArTPC however, several processes modify
1023 the light yield in between the location where light is produced and the optical detector.
1024 In a hypothetical pure tank of argon, Rayleigh scattering would be the most important
1025 processes modifying the light yield. Rayleigh scattering changes the path of light
1026 propagation in argon, prolonging the time between light production and detection.
1027 The scattering length has been measured to be 66 cm [79] , shorter than the theoretical
1028 prediction of ~ 90 cm [112]; this value is short enough to be relevant for the current
1029 size of LArTPCs detectors. In fact, Rayleigh scattering worsen the resolution on t_0 ,
1030 the start time for charge drifting, and alters the light directionality, complicating the
1031 matching between light and charge coming from the same object in case of multiple
1032 charged particles in the detector.

1033 Traces of impurities in argon such as oxygen, water and nitrogen also affect the
1034 light yield, mainly via absorption and quenching mechanisms. Absorption occurs as
1035 the interaction of a 128 nm photon directly with the impurity dissolved in the liquid
1036 argon. Differently, quenching occurs as the interaction of an argon excimer and an
1037 impurity, where the excimer transfers its excitation to the impurity and dissociates
1038 non-radiatively. Given this mechanism, it is evident how quenching is both a function
1039 of the impurity concentrations and the excimer lifetime. Since the triplet states
1040 live much longer than the singlet states, quenching occurs mainly on triplet states,
1041 affecting primarily the slow component of the light, reducing the scintillation yield
1042 and a shortening of the scintillation time constants.

1043 The stringent constraints for the electron life time limit the presence of oxygen and
1044 water to such a low level that both absorption and quenching on these impurity is not

1045 expected to be significant. Contrarily, the nitrogen level is not bound by the electron
1046 life time constraints – nitrogen being an inert gas, expensive to filter. Thus, nitrogen
1047 is often present at the level provided by the vendor. The effects of nitrogen on argon
1048 scintillation light have been studied in the WArP R&D program and at several test
1049 stands. The quenching process induced by nitrogen in liquid Ar has been measured
1050 to be proportional to the nitrogen concentration, with a rate constant of ~ 0.11
1051 μs^{-1} ppm $^{-1}$; appreciable decreasing in lifetime and relative amplitude of the slow
1052 component have been shown for contamination as high as a few ppm of nitrogen [6].
1053 For a nitrogen concentration of 2 parts per million, typical of the current generation
1054 of LArTPC, the attenuation length due to nitrogen has been measured to be ~ 30
1055 meters [83].

1056 **Wavelength Shifting of LAr Scintillation Light**

1057 Liquid argon scintillation light is invisible for most optical detectors deployed in a
1058 LArTPC, such as cryogenic PMTs and SiPMs, since a wavelength of 128 nm is gen-
1059 erally too short to be absorbed from most in glasses, polymers and semiconductor
1060 materials. Research on prototype SiPMs absorbing directly VUV light and their
1061 deployment in noble gasses experiment is ongoing but not mature [120]. Thus, ex-
1062 periments need to shift the wavelength of scintillation light to be able to detect it.
1063 Albeit deployed in different ways, neutrinos and dark matter experiments commonly
1064 use 1,1,4,4-tetraphenyl-butadiene (TPB) to shift the scintillation light. TPB absorbs
1065 the vacuum ultraviolet (VUV) light and emits in the visible at ~ 425 nm [33], with
1066 a ratio of visible photon emitted per VUV photon absorbed of $\sim 1.2:1$ [66].

1067 Neutrino experiments typically coat their optical detector system evaporating a
1068 layer of TPB either directly on the PMTs glass surface or on acrylic plates mounted in
1069 front of the PMTs [60]; this technique allows the fast detection light coming directly
1070 from the neutrino interaction. Dark matter experiments typically evaporate TPB on

1071 reflective foils mounted on the inside walls of the sensitive volume and detect the
1072 light after it has been reflected; this technique leads to a higher and more uniform
1073 light yield, though scattering effects for both the visible and VUV light augment
1074 the propagation time and hinder directionality information [61]. In order to take
1075 advantage of both these techniques, hybrid systems with PMT coating and foils are
1076 being considered for the next generation of large neutrino detectors.

1077 2.1.5 Signal Processing and Event Reconstruction

1078 In this section we illustrate the processing and reconstruction chain of the TPC sig-
1079 nals, from the pulses on the sense wire to the construction of three dimensional objects
1080 with associated calorimetry. Different experiments can chose different software pack-
1081 ages for their off line signal processing and event reconstruction, but a popular choice
1082 for US based LArTPCs is LArSoft [40]. Based on the Art framework [73], LArSoft is
1083 an event-based toolkit to perform simulation, analysis and reconstruction of LArT-
1084 PCs events.

1085

1086 LArTPC signal processing develops in several consecutive stages that we summa-
1087 rize here in the following categories: *Deconvolution, Hit Reconstruction, 2D Cluster-*
1088 *ing, 3D Tracking, Calorimetry Reconstruction*. A visualization of the signal processing
1089 workflow is shown in figure 2.6.

1090

1091 **Deconvolution.** Induction and collection planes have different field responses,
1092 given the different nature of the signals on these planes: the wires on the induction
1093 planes see the inductive signal of the drifting charge, while the wires on the collection
1094 planes see the current derived from the charge entering the conductor. Thus, signals
1095 on the induction plane are bi-polar pulse and signal on the collection plane are unipo-
1096 lar pulses, see Figure 2.6 panel a). The first step in signal processing is deconvolution,

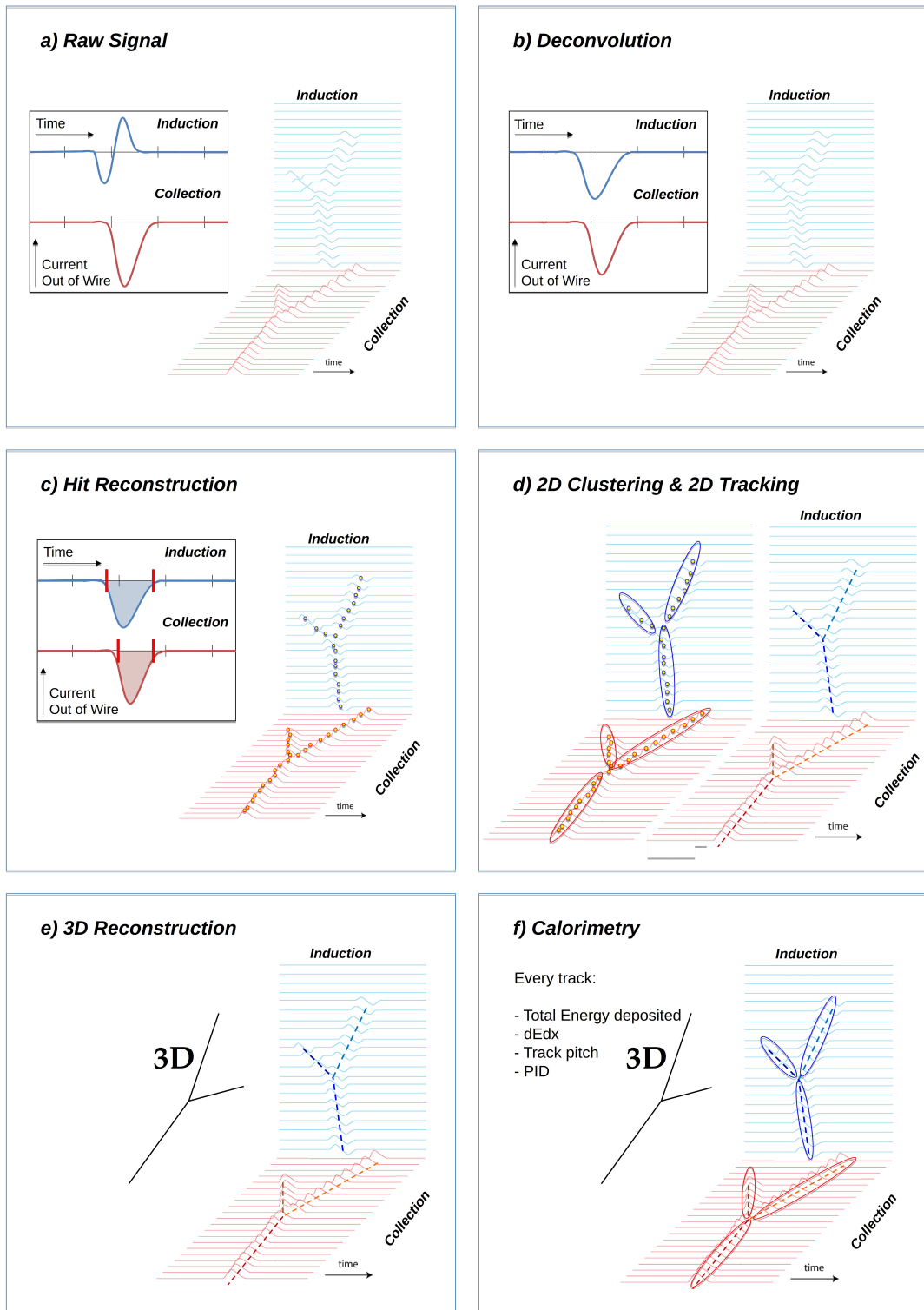


Figure 2.6: A scheme of a typical signal processing workflow in LArSoft.

1097 that is a series of off-line algorithms geared towards undoing the detector effects. The
1098 result of the deconvolution step is the production of a comparable set waveforms on
1099 all planes presenting unipolar, approximately gaussian-like pulses (Figure 2.6 panel
1100 b). Signal from all planes are treated on equal footage beyond this point. Some
1101 LArTPC apply noise filtering in the frequency domain just after the deconvolution
1102 to clean up wire cross talk. Since signals from the LArIAT TPC are extremely clean,
1103 noise filtering is not necessary.

1104

1105 **Hit Reconstruction.** The second stage of the signal processing is the recon-
1106 struction of hits, indicating an energy deposition in the detector. A peak finder scans
1107 the deconvolved TPC waveforms for each wire on the whole readout time looking for
1108 spikes above the waveform’s baseline. It then fits these peaks with gaussian shapes
1109 and stores the fit parameters such as the quality of the fit, the peak time, height and
1110 area under the gaussian fit. The information resulting from this process on a single
1111 spike form a single reconstructed “hit”, see Figure 2.6 panel c). The next steps in
1112 the event reconstruction chain will then decide if rejecting hits with poor fits. It is
1113 important to notice how the height and width of the hit depend on the topology of
1114 the event: for example, a particle running parallel to the wire planes will leave a series
1115 of sharp hits on many consecutive wires, while a particle traveling towards the planes
1116 will leave a long, wide hit on very few wires. The height of the hits and their integral
1117 is proportional to the charge collected on the wire, so it depends on the particle type.

1118

1119 The event reconstruction chain uses collection of hits to form more complex objects
1120 associated with the particles in the detector. The development of different approaches
1121 to accomplish this task is an extremely hot topic in LArTPC event reconstruction
1122 which spans from more traditional approaches such as line-clustering [26] to the use of
1123 machine learning tools [59]. Generally speaking, the scope of hit clustering and event

1124 reconstruction to provide shower-like or track like-objects with an associated energy
1125 reconstruction. This is because different particles have different topology in the de-
1126 tector – electrons and photon create electromagnetic showers, resulting in shower-like
1127 topologies, while muons and hadrons leave track-like signals. For the scope of these
1128 thesis, we will describe only LArIAT’s approach to track reconstruction even if we
1129 recognize the breath of LArTPC event reconstruction is much wider. We are inter-
1130 ested in the reconstruction of pions and kaons in the active volume, whose topology
1131 is track-like.

1132

1133 **2D Clustering Reconstruction.** The LArIAT reconstruction of track-like ob-
1134 jects starts by clustering hits on the collection and induction planes separately with
1135 the use of the TrajCluster clustering package [25]. TrajCluster looks for a collection
1136 of hits in the wire-time 2D space which can be described with a line-like 2D trajec-
1137 tory. TrajCluster reconstructs trajectories by adding trajectory points to the leading
1138 edge of the trajectory while stepping through the 2D space of hits. Several factors
1139 determine whether a hit is added to the trajectory, including but not limited to

- 1140 1. the goodness of the fit of the single hit,
- 1141 2. the charge of the hit compared to the average charge and RMS of the hits
1142 already forming the trajectory,
- 1143 3. the goodness of trajectory fit with and without the hit addition,
- 1144 4. the angle between the two lines formed by the collection of hits before and after
1145 the considered hit in the trajectory.

1146 The final product of this reconstruction stage is the collection of bidimensional clusters
1147 on each wire plane, see Figure 2.6 panel d).

1148 **3D Tracking.** The 3D tracking set of algorithms uses clusters close in time on
1149 the induction and collection planes as starting point to form a 3D track. Firstly, it

1150 construct a tentative 3D trajectory using the edges of the clusters. Then, it projected
1151 back the tentative trajectory on to the planes and adjusts the parameters of the 3D
1152 track fit such that they minimize the distance between the fit projections and the
1153 track hits in all wire planes simultaneously. Tridimensional tracking can use multiple
1154 clusters in one plane, but it can never break them in smaller groups of hits. This
1155 algorithm was first developed for the ICARUS collaboration [20]. The final product
1156 of this reconstruction stage is the formation of tridimensional objects in the TPC
1157 active volume, see Figure 2.6 panel e).

1158

1159 **Calorimetry.** The last step in the event reconstruction chain is to assign calorimetric
1160 information to the track (or shower) objects. Calorimetry is performed separately
1161 on the different planes. A multi-step procedure is needed to retrieve the energy
1162 deposited in the TPC from the charge seen by the wires. For each hit associated with
1163 the track object, the calorimetry algorithms calculate the charge seen on every wire
1164 using the area underneath the gaussian fit; then, they correct this raw charge by the
1165 electron life time, the electronic noise on the considered wire and the recombination
1166 effect. Lastly an overall calibration of the energy, explained in detail in section B,
1167 is applied and the calorimetric information for the given track is assigned. Even if
1168 calorimetry is done in 2D, it benefits from the 3D tracking information; typical information
1169 available after the calorimetric reconstruction are the total energy deposited
1170 by the particle and its stopping power dE/dx at each “track pitch”, i.e. at each 2D
1171 projection on the wire plane of the 3D trajectory.

1172 2.2 The Intensity Frontier Program

1173 This section highlights the role of Liquid Argon Time Projection Chambers at the
1174 Intensity frontier. In particular, we show the prospects for the exploration of neutrino

1175 physics (Section 2.2.1) and GUT models (Section 2.2.2) in current and forthcoming
1176 LAr experiments. In Section , we introduce LArIAT and its role in the Intensity
1177 Frontier panorama.

1178 **2.2.1 Prospects for LArTPCs in Neutrino Physics: SBN and**
1179 **DUNE**

1180 The ArgoNeut experiment [17] together the LAr R&D experiments TallBo and the
1181 Yale TPC initiated the US LArTPC neutrino program. Following the success of the
1182 ArgoNeut small TPC on the NuMI beam, a wide program of LArTPCs on neutrino
1183 beams has flourished. The construction of LArTPCs as near and far detectors at
1184 different baseline allows for the exploration of some of the fundamental questions in
1185 neutrino physics today illustrated in section 1.3.1.

1186 The Short-Baseline Neutrino (SBN) [21] program at Fermilab is tasked with con-
1187 clusively assess the nature of the “LSND and MiniBooNE anomalies” [14, 15, 23],
1188 resolving the mystery of sterile neutrinos at the eV² scale. The SBN program entails
1189 three surface LArTPCs positioned on the Booster Neutrino Beam at different dis-
1190 tances from the neutrino production in oder to fully exploit the L/E dependence of
1191 the oscillation pattern: SBND (100 m from the decay pipe), MicroBooNE (450 m),
1192 and ICARUS (600 m). Within the oscillation context, the choice of the LArTPC tech-
1193 nology for the SBN detectors changes the set of systematics with respect to LSND
1194 and MiniBooNE, whose detection techniques were both based on Cherenkov light.
1195 In particular, LArTPCs provide excellent electron/photon separation [9] lacking in
1196 Cherenkov detectors which can be leveraged to abate the photon background from
1197 neutral current interactions in ν_e searches. MicroBooNE [8], the first detector of the
1198 SBN program to be fully operational, started its first neutrino run in October 2015.
1199 MicroBooNE is a 89 ton active volume LArTPC, single drift chamber with TPC di-
1200 mensions of 2.6 m (drift) x 2.3 m (heigh) x 10.4 m (depth). MicroBooNE is positioned

at a very similar L/E on the Booster neutrino beam as MiniBooNE has the scope to directly cross check the MiniBooNE oscillation measurement. In case MicroBooNE confirms the presence of the “low energy excess” anomaly, SBND and ICARUS will provide the full measurement of the oscillation parameters. SBND and ICARUS are both dual drift chambers, whose active volume is respectively 112 ton and 600 ton. ICARUS is scheduled to become operational by the end of 2018 and SBND shortly after. Besides the oscillation analysis, the second main goals of SBN is to perform an extensive campaign of neutrino cross section measurements in argon. Given the importance of nuclear effects in (relatively) heavy materials, as discussed in section 1.2.3, both the oscillation analysis of the SBN program and the measurements of neutrino properties in DUNE will benefit from such a campaign.

On a different neutrino beam and baseline, the DUNE experiment, née LBNE [11], is the flagship experiment on the medium-long term of US-based neutrino physics, scheduled to start data taking in 2026. Shooting neutrinos from Fermilab for 800 miles to the SURF laboratory in South Dakota, DUNE is tasked with performing conclusive measurements of CP violation in the lepton sector, the neutrino mass ordering and the θ_{23} octant. The DUNE far detector will count four 10 kton LArTPCs, roughly of dimensions of 19 m (horizontally) x 18 m (vertically) x 66 m (depth).

2.2.2 Prospects for LArTPCs in GUT Physics: DUNE

The experimental exploration of a manifestation of Grand Unified Theory is possible in DUNE thanks to its sheer mass. In particular, proton decay searches are a capital topic of DUNE’s wide non-accelerator physics program. The key elements for a rare decay experiment are: massive active volume, long exposure, high identification efficiency and low background. Figure 2.7 shows the current best experimental limits on nucleon decay lifetime over branching ratio (dots). Historically, the dominant technology used in these searches has been water Cherenkov detectors: all the best

1227 experimental limits on every decay mode are indeed set by Super-Kamiokande [?, ?].
 1228 As shown in section 1.3.2, different family of GUTs predict the proton to decay in
 1229 different modes. In particular, SUSY flavored GUTs prefer the presence of kaons
 1230 in the decay products, e.g. $p \rightarrow K^+ \bar{\nu}$. It is particularly important to notice that
 1231 the kaon energy for the proton decay mode $p \rightarrow K^+ \bar{\nu}$ is under Cherenkov threshold
 1232 in water. Thus, Super-Kamiokande set the limit on the lifetime for the $p \rightarrow K^+ \bar{\nu}$
 1233 mode by relying on photons from nuclear de-excitation and on the muon tagging in
 1234 the kaon decay leptonic mode. For this reason, an attractive alternative approach to
 1235 identifying nucleon decay is the use of a LArTPCs, where the kaon is directly visible
 1236 in the detector. According to [11], DUNE will have an active volume large enough,
 1237 have sufficient shielding from the surface, and will run for lengths of time sufficient
 1238 to compete with Hyper-K, opening up the opportunity for the discovery of nucleon
 1239 decay.

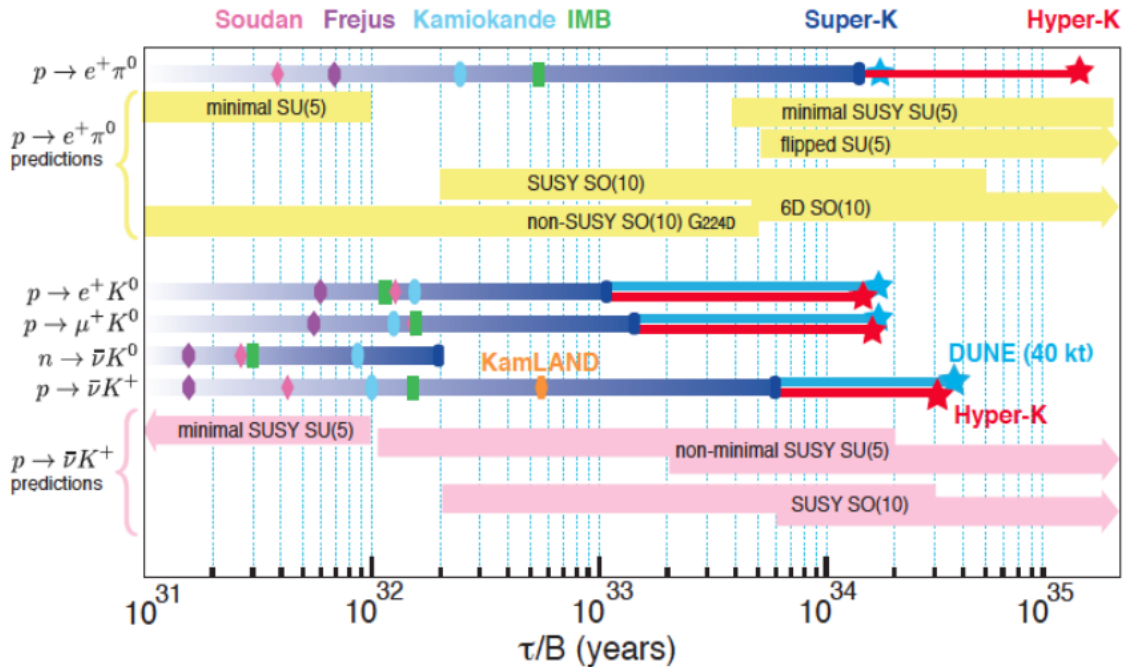


Figure 2.7: Proton decay lifetime limits from passed and future experiments.

1240 2.2.3 Enabling the next generation of discoveries: LArIAT

1241 LArIAT, a small LArTPC in a test beam, is designed to perform an extensive physics
1242 campaign centered on charged particle cross section measurements while characteriz-
1243 ing the detector performance for future LArTPCs. Since LArTPCs represent the most
1244 advanced experiments for physics at the Intensity Frontier, their complex technology
1245 needs a thorough calibration and dedicated measurements of some key quantities to
1246 achieve the precision required for the next generation of discoveries. LArIAT’s goal
1247 is to provide such calibration and dedicated measurements. The LArIAT LArTPC is
1248 deployed in a dedicated calibration test beamline at Fermilab. We use the LArIAT
1249 beamline to characterize the charge particles before they enter the TPC: the particle
1250 type and initial momentum is known from beamline information. The precise calori-
1251 metric energy reconstruction of the LArTPC technology enables the measurement of
1252 the total differential cross section for tagged hadrons. The Pion-Nucleus and Kaon-
1253 Nucleus total hadronic interaction cross section have never been measured before in
1254 argon and they are a fundamental step to shed light on light meson interaction in nu-
1255 clei per se, while providing a key input to neutrino physics and proton decay studies
1256 in future LArTPC experiments like SBN and DUNE.

1257 In order to showcase LArIAT’s utility to SBN and DUNE, we illustrate briefly
1258 two comparisons as examples: one regarding neutrino interactions and the second
1259 regarding proton decay studies.

1260 The left side of figure 2.8 shows the distribution of products in momentum spectrum
1261 and particle type as simulated in a ν_e CC interaction in DUNE (according to [88]);
1262 the range of these distribution is to compare with the momentum distribution of
1263 light particles in the LArIAT beamline – shown on the right side of figure 2.8. The
1264 momentum spectrum in the LArIAT beamline for electrons, muons and pions – the
1265 most abundant particles produced in a ν_e CC interaction – covers a wide range of the
1266 expected momentum distribution in a neutrino event.

1267 The signature of a proton decay event in the “LAr golden mode” is the presence of
 1268 a single kaon of about 400 MeV in the detector; the momentum spectrum of the kaon
 1269 pre and post FSI in such an event as simulated by GENIE is shown on the left side
 1270 of figure 2.9. The right side of figure 2.9 shows the momentum spectrum of kaons in
 1271 the LArIAT beamline. Kaons arriving to the LArIAT TPC are ideal for proton decay
 1272 studies, since their momentum in the beamline is just above the typical momentum
 1273 for kaons in a proton decay event: the majority of LArIAT kaons slow down in the
 1274 TPC enough to enter the desired momentum window.

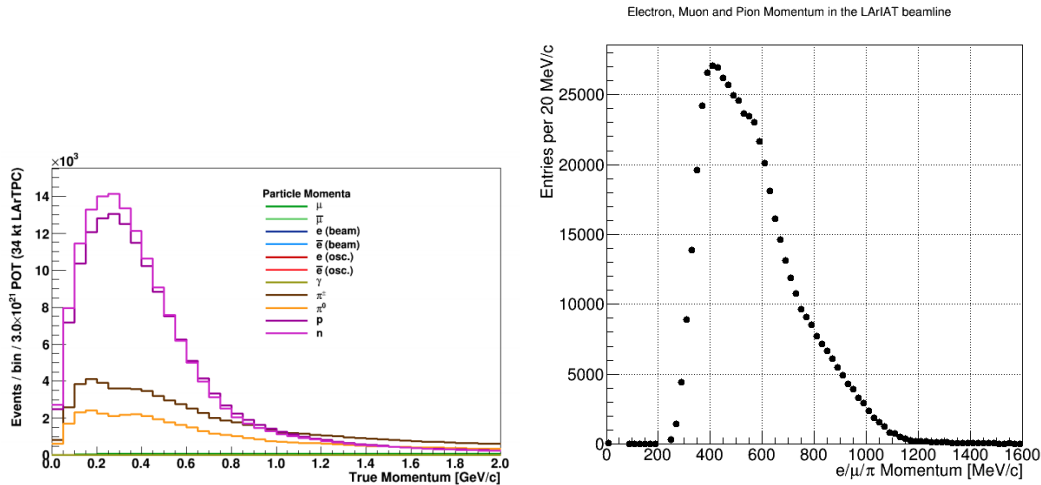


Figure 2.8: *Left.* Simulation of the products of a ν_e CC interaction in DUNE, both in particles type and momentum.
Right. Momentum spectrum for low mass particles (e, μ, π) in the LArIAT beamline, negative tune, Run II, Picky Tracks see section 3.2.2.

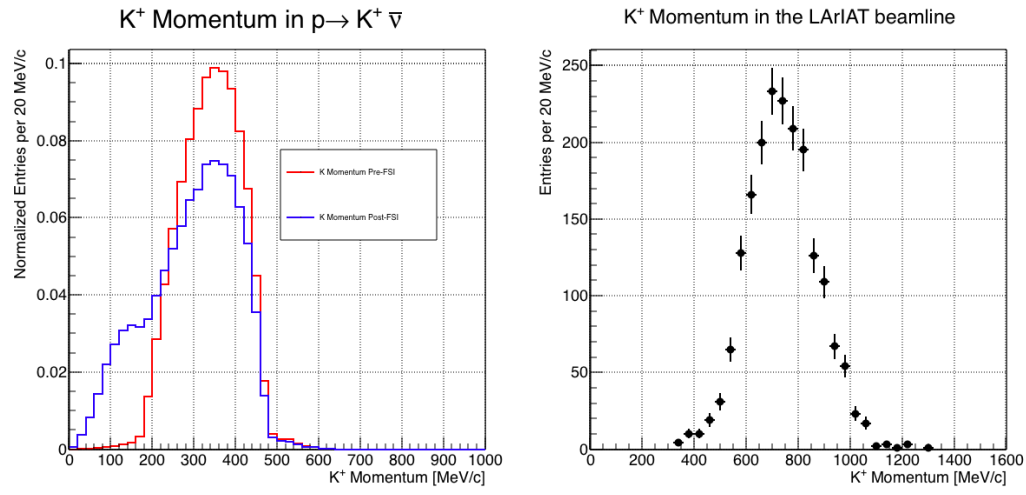


Figure 2.9: *Left.* Momentum of the kaon outgoing a proton decay $p \rightarrow K^+ \bar{\nu}$ event as simulated by the Genie 2.8.10 event generator in argon. The red line represents the kaon momentum distribution before undergoing the simulated final state interaction inside the argon nucleus, while the blue line represents the momentum distribution after FSI.

Right. Positive Kaon momentum spectrum in the LArIAT beamline, positive tune, Run II, Picky Tracks see section 3.2.2.

₁₂₇₅ **Chapter 3**

₁₂₇₆ **LArIAT: Liquid Argon In A
₁₂₇₇ Testbeam**

₁₂₇₈ “*But, hey we need to be somewhat foolish...*”
₁₂₇₉ – Agnes Obel, 2010 –

₁₂₈₀ In this chapter, we describe the LArIAT experimental setup. We start by illus-
₁₂₈₁ trating the journey of the charged particles in the Fermilab accelerator complex, from
₁₂₈₂ the gaseous thermal hydrogen at the Fermilab ion source to the delivery of the LAr-
₁₂₈₃ IAT tertiary beam at MC7. We then describe the LArIAT beamline detectors, the
₁₂₈₄ LArTPC, the DAQ and the monitoring system.

₁₂₈₅ **3.1 The Particles’ Path to LArIAT**

₁₂₈₆ LArIAT’s particle history begins in the Fermilab accelerator complex with a beam of
₁₂₈₇ protons. The process of proton acceleration develops in gradual stages (see picture
₁₂₈₈ 3.1): gaseous hydrogen is ionized in order to form H^- ions; these ions are boosted
₁₂₈₉ to 750 keV by a Cockcroft-Walton accelerator and injected into the linear accelerator
₁₂₉₀ (Linac) that increases their energy up to 400 MeV; then, H^- ions pass through a

1291 carbon foil and lose the two electrons; the resulting protons are then injected into a
1292 rapid cycling synchrotron, called the Booster; at this stage, protons reach 8 GeV of
1293 energy and are compacted into bunches; the next stage of acceleration is the Main
1294 Injector, a synchrotron which accelerates the bunches up to 120 GeV; in the Main
1295 Injector, several bunches are merged into one and are ready for delivery.

1296 The Fermilab accelerator complex works in supercycles of 60 seconds in duration.
1297 A 120 GeV primary proton beam with variable intensity is extracted in four-second
1298 “spills” and sent to the Meson Center beam line.

1299 LArIAT’s home at Fermilab is the Fermilab Test Beam Facility (FTBF), where
1300 the experiment characterizes a beam of charged particles in the Meson Center beam
1301 line. At FTBF, the primary beam is focused onto a tungsten target to create LAr-
1302 IAT’s secondary beam. The secondary beamline is set such that the composition of
1303 the secondary particle beam is mainly positive pions. The momentum peak of the
1304 secondary beam was fixed at 64 GeV/c for the LArIAT data considered in this work,
1305 although the beam is tunable in momentum between 8-80 GeV/c; this configuration
1306 of the secondary beamline assured a stable beam delivery at the LArIAT experimental
1307 hall.

1308 The secondary beam impinges then on a copper target within a steel collimator
1309 inside the LArIAT experimental hall (MC7) to create the LArIAT tertiary beam,
1310 (shown in Fig. 3.2). The steel collimator selects particles produced with a 13° pro-
1311 duction angle. The particles are then bent by roughly 10° through a pair of dipole
1312 magnets. By configuring the field intensity of the magnets we allow the particles of
1313 LArIAT’s tertiary beam to span a momentum range from 0.2 to 1.4 GeV/c. The
1314 polarity of the magnet is also configurable and determines the sign of the beamline
1315 particles which are focused on the LArTPC. If the magnet polarity is positive the
1316 tertiary beam composition is mostly pions and protons with a small fraction of elec-
1317 trons, muons, and kaons. It is the job of the LArIAT beamline equipment to select the

Fermilab Accelerator Complex

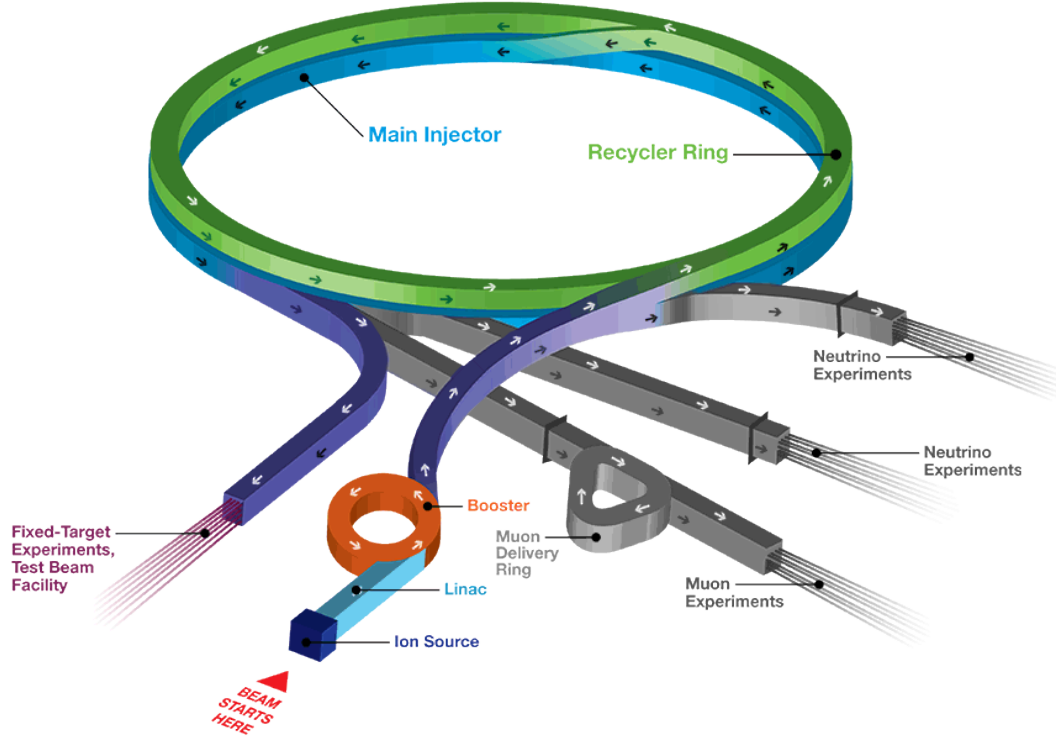


Figure 3.1: Layout of Fermilab Accelerator complex.

1318 particles polarity, to perform particle identification in the beamline and to measure
1319 the momentum of the tertiary beam particles before they get to the LArTPC. The
1320 LArIAT detectors are described in the following paragraphs.

1321 3.2 LArIAT Tertiary Beam Instrumentation

1322 The instrumentation of LArIAT tertiary beam and the TPC components have changed
1323 several times during the three years of LArIAT data taking. The following paragraphs
1324 describe the components operational during “Run II”, the data taking period relevant
1325 to the hadron cross section measurements considered in this thesis.

1326 The key components of the tertiary beamline instrumentation for the hadron cross
1327 section analyses are the two bending magnets, a set of four wire chambers (WCs)

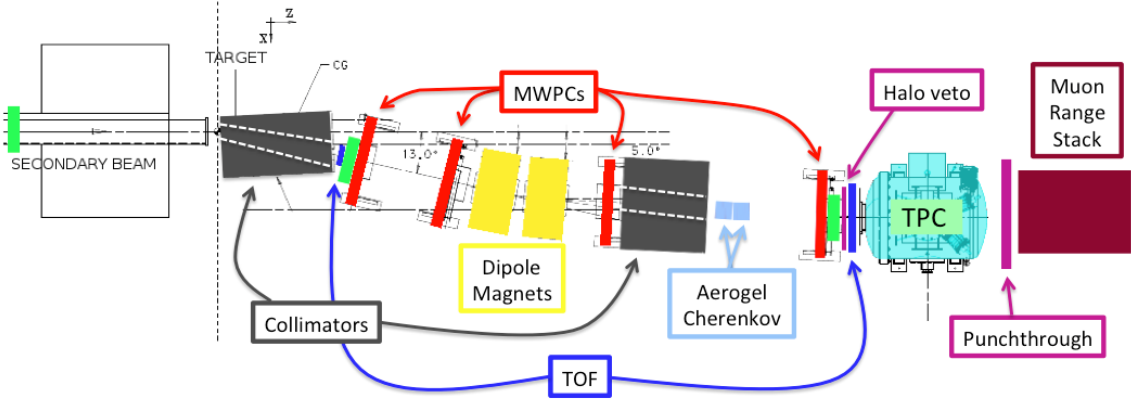


Figure 3.2: Bird’s eye view of the LArIAT tertiary beamline. In grey: upstream and downstream collimators; in yellow: bending magnets; in red: multi wire proportional chambers; in blue: time of flight; in green: liquid argon TPC volume; in maroon: muon range stack.

and two time-of-flight scintillating paddles (TOF) and, of course, the LArTPC. The magnets determine the polarity of the particles in the tertiary beam; the combination of magnets and wire chambers determines the particles’ momenta, which is used to determine the particle species in conjunction with the TOF. A muon range stack downstream from the TPC and two sets of cosmic paddles configured as a telescope surrounding the TPC are also used for calibration purposes. A couple of Aerogel Cherenkov counters, which we will not describe here as they are not used in the hadron cross section measurements, completes the beamline instrumentation.

3.2.1 Bending Magnets

LArIAT uses a pair of identical Fermilab type “NDB” electromagnets, recycled from the Tevatron’s anti-proton ring, in a similar configuration used for the MINERvA T-977 test beam calibration [56]. The magnets are a fundamental piece of the LArIAT beamline equipment, as they are used for the selection of the particle polarity and for the momentum measurement before the LArTPC. The sign of the current in the magnets allows us to select either positively or negatively charged particles; the value

1343 of the magnetic field is used in the momentum determination and in the subsequent
1344 particle identification.

1345 We describe here the characteristics and response of one magnet, as the second one
1346 has a similar response, given its identical shape and history. Each magnet is a box with
1347 a rectangular aperture gap in the center to allow for the particle passage. The magnet
1348 aperture measures 14.22 cm in height, 31.75 cm in width, and 46.67 cm in length.
1349 Since the wire chambers aperture ($\sim 12.8 \text{ cm}^2$) is smaller than the magnet aperture,
1350 only the central part of the magnet gap is utilized. The field is extremely uniform
1351 over this limited aperture and was measured with two hall probes, both calibrated
1352 with nuclear magnetic resonance probes. The probes measured the excitation curve
1353 shown in Figure 3.3.

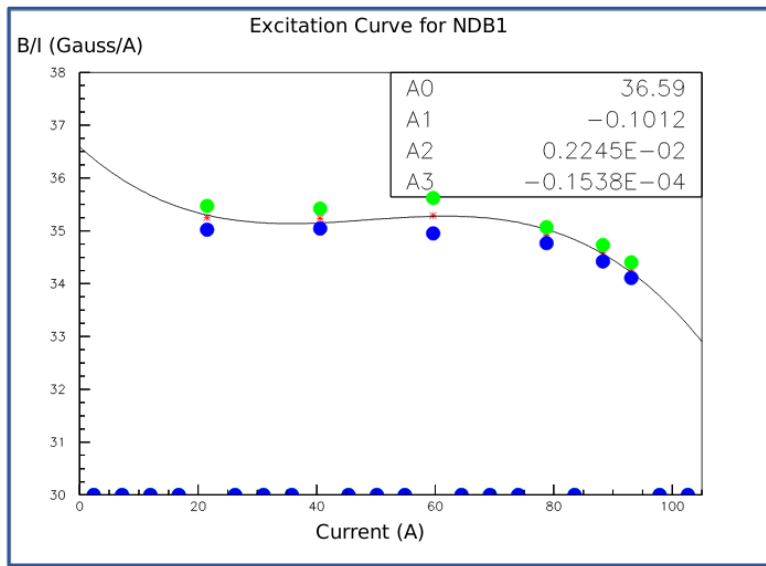


Figure 3.3: Magnetic field over current as a function of the current, for one NDB magnet (excitation curve). The data was collected using two hall probes (blue and green). We fit the readings with a cubic function (black) to average of measurements (red) given in the legend [43].

1354 The current through the magnets at a given time is identical in both magnets.
1355 For the Run II data taking period, the current settings explored were 60A ($B \sim 0.21$
1356 T) and 100A ($B \sim 0.35$ T) in both polarities. Albeit advantageous to enrich the
1357 tertiary beam composition with high mass particles such as kaons, we never pushed

1358 the magnets current over 100 A, not to incur in overheating. During operation, we
1359 operated an air and water cooling system on the magnets and we remotely monitored
1360 the magnet temperatures.

1361 **3.2.2 Multi-Wire Proportional Chambers**

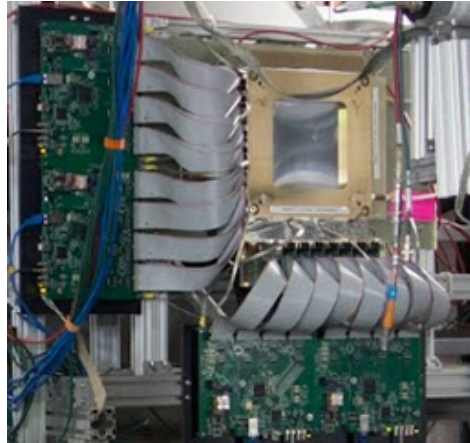


Figure 3.4: One of the four Multi Wire Proportional Chambers (WC) used in the LArIAT tertiary beamline and related read-out electronics.

1362 LArIAT uses four multi-wire proportional chambers, or wire chambers (WC) for
1363 short, two upstream and two downstream from the bending magnets. The geometry of
1364 one chamber is shown in Figure 3.4: the WC effective aperture is a square of 12.8 cm
1365 perpendicular to the beam direction. Inside the chamber, the 128 horizontal and 128
1366 vertical wires strung at a distance of 1 mm from each other in a mixture of 85% Argon
1367 and 15% isobutane gas. The WC operating voltage is between 2400 V and 2500 V.
1368 The LArIAT wire chambers are an upgraded version of the Fenker Chambers [62],
1369 where an extra grounding improves the signal to noise ratio of the electronic readout.

1370 Two ASDQ chips [96] mounted on a mother board plugged into the chamber serve
1371 as front end amplifier/discriminator. The chips are connected to a multi-hit TDC [74]
1372 which provides a fast OR output used as first level trigger. The TDC time resolution
1373 is 1.18 ns/bin and can accept 2 edges per 9 ns. The maximum event rate acceptable
1374 by the chamber system is 1 MHz: this rate is not a limiting factor considering that

1375 the rate of the tertiary particle beam at the first wire chamber is estimated to be less
1376 than 15 kHz. A full spill of data occurring once per supercycle is stored on the TDC
1377 board memory at once and read out by a specially designed controller. We use LVDS
1378 cables to carry both power and data between the controller and the TDCs and from
1379 the controller to the rest of the DAQ.

1380 Multi-Wire Proportional Chambers functionality

1381 We use the wire chamber system together with the bending magnets to measure the
1382 particle's momentum.

1383 In the simplest scenario, only one hit on each and every of the four wire chambers
1384 is recorded during a single readout of the detector systems. Thus, we use the hit
1385 positions in the two wire chambers upstream of the magnets to form a trajectory
1386 before the bend, and the hit positions in the two wire chambers downstream of the
1387 magnets to form a trajectory after the bend. We use the angles in the XZ plane
1388 between the upstream and downstream trajectories to calculate the Z component of
1389 the momentum as follows:

$$P_z = \frac{B_{eff}L_{eff}}{3.3(\sin(\theta_{DS}) - \sin(\theta_{US}))}, \quad (3.1)$$

1390 where B_{eff} is the effective maximum field in a square field approximation, L_{eff}
1391 is the effective length of both magnets (twice the effective length of one magnet),
1392 θ_{US} is the angle off the z axis of the upstream trajectory, θ_{DS} is the angle off the
1393 z axis of the downstream trajectory and $3.3 c^{-1}$ is the conversion factor from [T·m]
1394 to [MeV/c]. By using the hit positions on the third and fourth wire chamber, we
1395 estimate the azimuthal and polar angles of the particle trajectory, and we are able to
1396 calculate the other components of the momentum.

1397 The presence of multiple hits in a single wire chamber or the absence of hits in one
1398 (or more) wire chambers can complicate this simple scenario. The first complication

1399 is due to beam pile up, while the latter is due to wire chamber inefficiency. In the
1400 case of multiple hits on a single WC, at most one wire chamber track is reconstructed
1401 per event. Since the magnets bend particles only in the X direction, we assume
1402 the particle trajectory to be roughly constant in the YZ plane, thus we keep the
1403 combination of hits which fit best with a straight line. It is still possible to reconstruct
1404 the particle’s momentum even if the information is missing in either of the two middle
1405 wire chambers (WC2 or WC3), by constraining the particle trajectory to cross the
1406 plane in between the magnets.

1407 Events satisfying the simplest scenario of one single hit in each of the four wire
1408 chambers form the “Picky Track” sample. We construct another, higher statistics
1409 sample, where we loosen the requirements on single hit and wire chamber efficiency:
1410 the “High Yield” sample. For LArIAT Run II, the High Yield sample is about three
1411 times the Picky Tracks statistics. We assume an uncertainty of 2% for four-point WC
1412 track, momentum uncertainty as reported for the same beamline in [56].

1413 3.2.3 Time-of-Flight System

1414 Two scintillator paddles, one upstream of the first set of WCs and one downstream
1415 of the second set of WCs form LArIAT time-of-flight (TOF) detector system.

1416 The upstream paddle is made of a 10 x 6 x 1 cm scintillator piece, read out by
1417 two PMTs mounted on the beam left side which collect the light from light guides
1418 mounted on all four edges of the scintillator. The downstream paddle is a 14 x 14 x
1419 1 cm scintillator piece read out by two PMTs on the opposite ends of the scintillator,
1420 as shown in figure 3.5. The relatively thin width in the beamline direction minimizes
1421 energy loss of beam particles traveling through the scintillator material.

1422 The CAEN 1751 digitizer is used to digitize the TOF PMTs signals at a sampling
1423 rate of 1 GHz. The 12 bit samples are stored in a circular memory buffer. At trigger
1424 time, data from the TOF PMTs are recorded to output in a 28.7 μ s windows starting

1425 approximately 8.4 μ s before the trigger time.

1426 **TOF functionality**

1427 The TOF signals rise time (10-90%) is 4 ns and a full width, half-maximum of 9 ns
1428 consistent in time. The signal amplitudes from the upstream TOF and downstream
1429 TOF are slightly different: 200 mV for the upstream PMTs but only 50 mV for
1430 downstream PMTs. The time of the pulses was calculated utilizing an oversampled
1431 template derived from the data itself. We take the pulse pedestal from samples
1432 far from the pulse and subtract it from the pulse amplitude. We then vertically
1433 stretch a template to match the pedestal-subtracted pulse amplitude and we move
1434 it horizontally to find the time. With this technique, we find a pulse time-pickoff
1435 resolution better than 100 ps. The pulse pile up is not a significant problem given
1436 the TOF timing resolution and the rate of the particle beam. Leveraging on the
1437 pulses width uniformity of any given PMT, we flag events where two pulses overlap
1438 as closely in time as 4 ns with a 90% efficiency according to simulation.

1439 We combine the pulses from the two PMTs on each paddle to determine the
1440 particles' arrival time by averaging the time measured from the single PMT, so to
1441 minimize errors due to optical path differences in the scintillator. However, a time
1442 spread of approximately 300 ps is present in both the upstream and downstream
1443 detectors, likely due to transit time jitter in the PMTs themselves.

1444 **3.2.4 Punch-Through and Muon Range Stack Instruments**

1445 The punch-through and the muon range stack (MuRS) detectors are located down-
1446 stream of the TPC. These detectors provide a sample of TPC crossing tracks without
1447 relying on TPC information and can be used to improve particle ID for muons and
1448 pions with momentum higher than 450 MeV/c.

1449 The punch-through is simple sheet of scintillator material, read out by two PMTs.



Figure 3.5: Image of the down stream time of flight paddle, PMTs and relative support structure before mounting.

1450 The MuRS is a segmented block of steel with four slots instrumented with scintillation
1451 bars. The four steel layers in front of each instrumented slot are 2 cm, 2 cm, 14 cm
1452 and 16 cm deep in the beam direction. Each instrumented slot is equipped with
1453 four scintillation bars each, positioned horizontally in the direction orthogonal to the
1454 beam. Each scintillator bar measures $\textcolor{red}{? \times ? \times 2}$ cm and it is read out by one PMT.

1455 The signals from both the punch-thorough and the MuRS PMTs are sent to a
1456 NIM discriminator. If the signal crosses the discriminator threshold, it is digitized in
1457 the CAEN V1740, same as the TPC. The sampling time of the CAEN V1740 is slow
1458 (of the order of 128 ns) and that the pulse shape information from the PMT is lost.
1459 A Punch-thorough and MuRS signal will then be simply a “hit” at a given time in
1460 the beamline event.

1461 It is worth mentioning here the presence of an additional scintillation paddle
1462 between WC4 and the downstream paddle of the TOF system, called halo. The
1463 halo is a $39 \times 38 \times 1$ cm 3 paddle with a 6.5 cm radius hole in the center, whose original
1464 function was to reject beam particles slightly offset from the beamline center. Data

1465 from this paddle turned out to be unusable, so our data events include both particle
1466 going through the halo scintillation material or through the halo hole.

1467 3.2.5 LArIAT Cosmic Ray Paddle Detectors

1468 LArIAT triggers both on beam events and on cosmic rays events. We perform this
1469 latter trigger by using two sets of cosmic ray paddle detectors (a.k.a. “cosmic towers”.)
1470 The cosmic towers frame the LArIAT cryostat, as one sits in the downstream left
1471 corner and the other sits in the upstream right corner of the cryostat. Two paddle
1472 sets of four scintillators pieces each make up each cosmic tower, an upper set and a
1473 lower set per tower. Of the four paddles, a couple of two matched paddles stands
1474 upright while the a second matched pair lies across the top of the assembly in the top
1475 sets (or across the bottom of the assembly in the bottom sets). The horizontal couple
1476 is used as a veto for particles traveling from inside the TPC out. The four signals
1477 from the vertical paddles along one of the body diagonals of the TPC are combined
1478 in a logical “AND”. This allows to select track due to cosmic muons at the ground
1479 level crossing the TPC along one of its diagonals. Cosmic ray muons whose average
1480 energy is in the few GeV range crossing both anode and cathode populate the events
1481 triggered this way. This particularly useful sample of tracks is associated can be used
1482 for many tasks; for example, we use anode-cathode piercing tracks to cross check the
1483 TPC electric field on data (see Appendix ??), to calibrate the charge response of
1484 the TPC wires for the full TPC volume and to measure the electron lifetime in the
1485 chamber [105].

1486 We retrieved the scintillation paddles from the decommissioning of the CDF de-
1487 tector at Fermilab and we used only the paddles with a counting efficiency greater
1488 than 95% and low noise at working voltage. The measured trigger rate of the whole
1489 system is 0.032 Hz, corresponding to ~ 2 muons per minute.



Figure 3.6: Photograph of one of the scintillation counters used in the cosmic towers.

1490 3.3 In the Cryostat

1491 The heart of the LArIAT experiment lives in the LArIAT cryostat. In this section,
1492 we describe the cryogenic system and the argon purity (Section 3.3.1), the LArIAT
1493 TPC (Section 3.3.2) and light collection system (3.3.3).

1494 3.3.1 Cryogenics and Argon Purity

1495 LArIAT repurposed the ArgoNeuT cryostat [17] in order to use it in a beam of charged
1496 particles, and added a new process piping and a new liquid argon filtration system in
1497 FTBF. Inside the LArIAT experimental hall, the cryostat sits in the beam of charged
1498 particles with its horizontal main axis oriented parallel to the secondary beam, 3°
1499 off axis from the tertiary beam

1500 Two volumes make up LArIAT cryostat, shown in Figure 3.7: the inner vessel and
1501 the outer vessel. Purified liquid argon fills the inner vessel, while the outer volume
1502 provides insulation through a vacuum jacket equipped with layers of aluminized mylar
1503 superinsulation. The inner vessel is a cylinder of 130 cm length and 76.2 cm diameter,
1504 containing about 550 L of LAr, corresponding to a mass of 0.77 ton. We run the signal
1505 cables for the LArTPC and the high voltage feedthrough through a “chimney” at the
1506 top and mid-length of the cryostat.

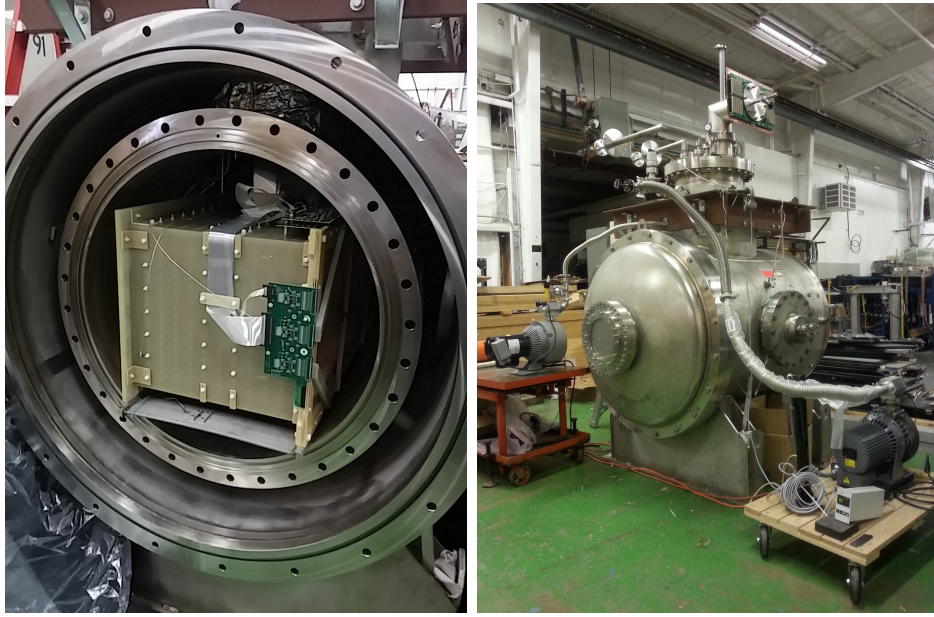


Figure 3.7: Left: the LArIAT TPC in the inner volume of the open cryostat. Right: cryostat fully sealed ready to be transported to FTBF.

Given the different scopes of the ArgoNeuT and LArIAT detectors, we made several modifications to the ArgoNeuT cryostat in order to use it in LArIAT. In particular, the modifications shown in Figure 3.8 were necessary to account for the beam of charged particles entering the TPC and to employ the new FTBF liquid argon purification system. We added a “beam window” on the front outer end cap and an “excluder” on the inner endcap, with the purpose of minimizing the amount of non-instrumented material upstream of the TPC’s active volume. The amount of non-instrumented material in front of the TPC for LArIAT corresponds to ~ 0.3 electron radiation lengths (X_0), to compare against the $\sim 1.6X_0$ of ArgoNeuT. To allow studies of the scintillation light, we added a side port feedthrough which enables the mounting of the light collection system, as well as the connections for the corresponding signal and high-voltage cables (see Section 3.3.3). We modified the bottom of the cryostat adding Conflat and ISO flange sealing to connect the liquid argon transfer line to the new argon cooling and purification system.

As in any other LArTPC, argon purity is a crucial parameter for LArIAT. Indeed,

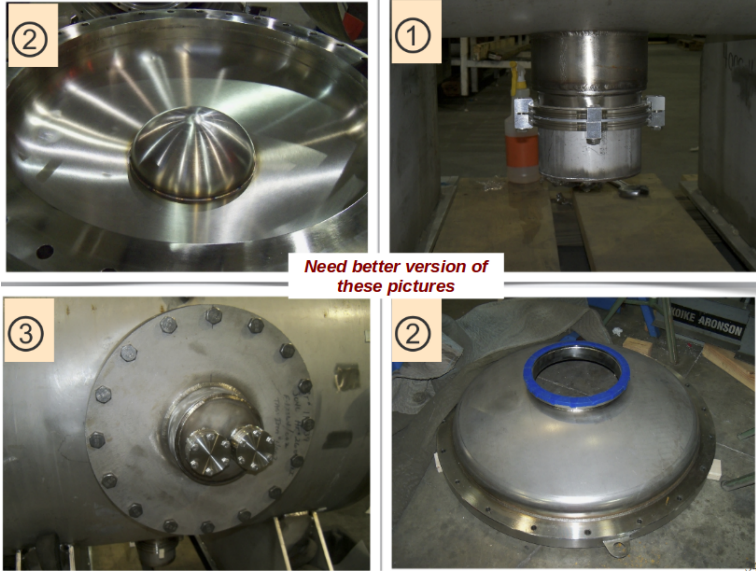


Figure 3.8: Main modifications to the ArgoNeuT cryostat: 1) outlet for connection to the purification system at the bottom of the cryostat; 2) the “beam-window” on the outer endcap and “excluder” which reduces the amount of non-instrumented material before the TPC; 3) the side port to host the light collection system.

1522 the presence of contaminants affects both the basic working principles of a LArTPC,
 1523 as shown in section 2.1.2: electronegative contaminants such as oxygen and water de-
 1524 crease the number of ionization electrons collected on the wires after drifting through
 1525 the volume. In addition, contaminants such as Nitrogen decrease the light yield
 1526 from scintillation light, especially in its slow component. In LArIAT, contaminations
 1527 should not exceed the level of 0.2 parts per billion (ppb). We achieve this level of
 1528 purity in several stages. The specifics required for the commercial argon bought for
 1529 LArIAT are 2 parts per million (ppm) oxygen, 3.5 ppm water, and 10 ppm nitrogen.
 1530 This argon is monitored with the use of commercial gas analyzer. Argon is stored in
 1531 a dewar external to LArIAT hall and filtered before filling the TPC. LArIAT uses a
 1532 filtration system designed for the Liquid Argon Purity Demonstrator (LAPD) [57]:
 1533 half of a 77 liter filter contains a 4A molecular sieve (Sigma-Aldrich [111]) able to re-
 1534 move mainly water, while the other half contains BASF CU-0226 S, a highly dispersed
 1535 copper oxide impregnated on a high surface area alumina, apt to remove mainly oxy-

1536 gen [27]. A single pass of argon in the filter is sufficient to achieve the necessary
1537 purity, unless the filter is saturated. In case the filter saturates, the media needs to
1538 be regenerated by using heated gas; this happened twice during the Run II period¹.
1539 The electron lifetime during the full LArIAT data taking are shown in Figure 2.4.
1540 The filtered argon reaches the inner vessel via a liquid feedthrough which is routed to
1541 the bottom of the cryostat. Argon is not recirculated in the system; rather, it boils
1542 off and vents to the atmosphere. During data taking, we replenish the argon in the
1543 cryostat every 6 hours to keep the TPC high voltage feedthrough and cold electronics
1544 always submerged. In fact, we constantly monitor the level, temperature, and pres-
1545 sure of the argon both in the commercial dewar and inside the cryostat during data
1546 taking.

1547 **3.3.2 LArTPC: Charge Collection**

1548 The LArIAT Liquid Argon Time Projection Chamber is a rectangular box of dimen-
1549 sions 47 cm (drift) x 40 cm (height) x 90 cm (length), containing 170 liters of Liquid
1550 Argon. The LArTPC three major subcomponents are

- 1551 1) the cathode and field cage,
- 1552 2) the wire planes,
- 1553 3) the read-out electronics.

1554 **Cathode and field cage**

1555 A G10 plain sheet with copper metallization on one of the 40 x 90 cm inner surfaces
1556 forms the cathode. A high-voltage feedthrough on the top of the LArIAT cryostat
1557 delivers the high voltage to the cathode; the purpose of the high voltage system

1. We deemed the filter regeneration necessary every time the electron lifetime dropped under 100 μs .

1558 (Figure 3.9) is to drift ionization electrons from the interaction of charged particles
 1559 in the liquid argon to the wire planes. The power supply used in this system is a
 1560 Glassman LX125N16 [71] capable of generating up to -125 kV and 16 mA of current,
 1561 but operated at -23.5kV during LArIAT Run-II. The power supply is connected via
 1562 high voltage cables to a series of filter pots before finally reaching the cathode.

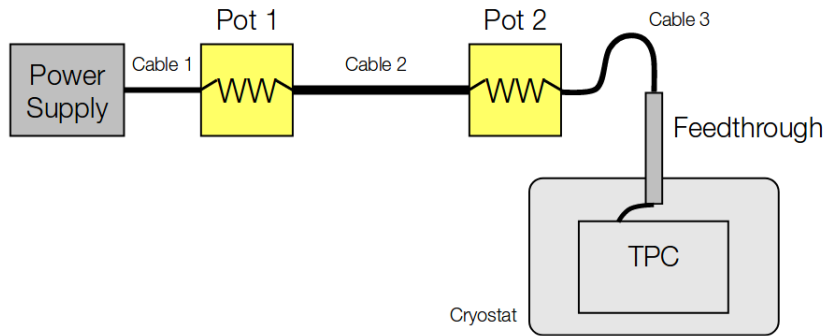


Figure 3.9: Schematic of the LArIAT high voltage system.

1563 The field cage is made of twenty-three parallel copper rings framing the inner
 1564 walls of the G10 TPC structure. A network of voltage-dividing resistors connected to
 1565 the field cage rings steps down the high voltage from the cathode to form a uniform
 1566 electric field. The electric field over the entire TPC drift volume is 486 V/cm, as
 1567 measured in appendix ???. The maximum drift length, i.e. the distance between
 1568 cathode and anode planes, is 47 cm.

1569 **Wire planes**

1570 LArIAT Run-II has three wire planes separated by 4 mm spaces: in order of increasing
 1571 distance from the cathode, they are the shield, the induction and the collection plane.
 1572 The “wire pitch”, i.e., the distance between two adjacent wires in a given plane, is
 1573 4 mm. The shield plane counts 225 parallel wires of equal length oriented vertically.
 1574 This plane is not connected with the read-out electronics; rather it shields the outer
 1575 planes from extremely long induction signals due to the ionization in the whole drift

volume. As the shield plane acts almost like a Faraday cage, the resulting shape of signals in the first instrumented plane (induction) is easier to reconstruct. Both the induction and collection planes count 240 parallel wires of different length oriented at 60° from the vertical with opposite signs. Electrons moving past the induction plane will induce a bipolar pulse on its wires; the drifting electrons will be then collected on the collection plane's wires, forming a unipolar pulse.

The three wire planes and the cathode form three drift volumes, as shown in Figure 3.10. The main drift volume is defined as the region between the cathode plane and the shield plane (C-S). The other two drift regions are those between the shield plane and the induction plane (S-I), and between the induction plane and the collection plane (I-C). The electric field in these regions is chosen to satisfy the charge transparency condition and allow for 100% transmission of the drifting electrons through the shield and the induction planes.

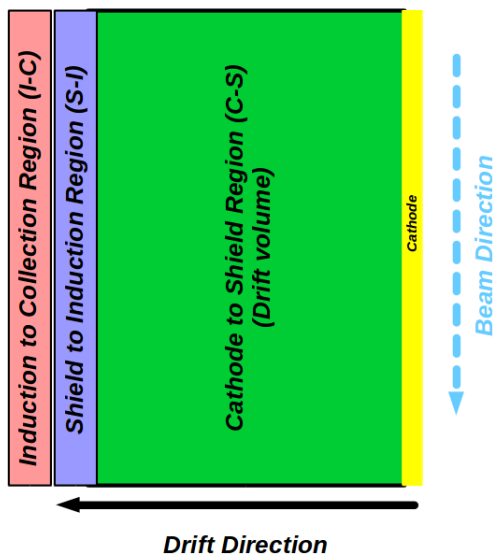


Figure 3.10: Schematic of the three drift regions inside the LArIAT TPC: the main drift volume between the cathode and the shield plane (C-S) in green, the region between the shield plane and the induction plane (S-I) in purple, and the region between the induction plane and the collection plane (I-C) in pink.

Table 3.1 provides the default voltages applied to the cathode and the shield,

1590 induction, and collection plane.

Table 3.1: Cathode and anode planes default voltages

Cathode	Shield	Induction	Collection
-23.17 kV	-298.8 V	-18.5 V	338.5 V

1591 Electronics

1592 Dedicated electronics read the induction and collection plane wires, for a total of
1593 480-channel analog signal path from the TPC wires to the signal digitizers. A digital
1594 control system for the TPC-mounted electronics, a power supply, and a distribution
1595 system complete the front-end system. Figure 3.11 shows a block diagram of the
1596 overall system. The direct readout of the ionization electrons in liquid argon forms
1597 typically small signals on the wires, which need amplification in oder to be processed.
1598 LArIAT performs the amplification stage directly in cold with amplifiers mounted
1599 on the TPC frame inside the liquid argon. The BNL ASICs adopted in LArIAT are
1600 designated as LArASIC, version 4-star and are the same used by the MicroBooNE
1601 experiment [60]. The signal from the ASICs are driven to the other end of the readout
1602 chain, to the CAEN V1740 digitizers [35]. The CAEN V1740 has a 12 bit resolution
1603 and a maximum input range of 2 VDC, resulting in about 180 ADC count for a
1604 crossing MIP.

1605 3.3.3 LArTPC: Light Collection System

1606 The collection of scintillation photons is the second mechanism of particle detection
1607 in argon other than the ionization electrons. Over the course of LArIAT's three years
1608 of data taking, the light collection system changed several times. We describe here
1609 the light collection system for Run II. Two PMTs, a 3-inch diameter Hamamatsu
1610 R-11065 and 2-inch diameter ETL D757KFL [7], as well as three SiPMs arrays (two
1611 Hamamatsu S11828-3344M 4x4 arrays and one single-channel SensL MicroFB-60035)

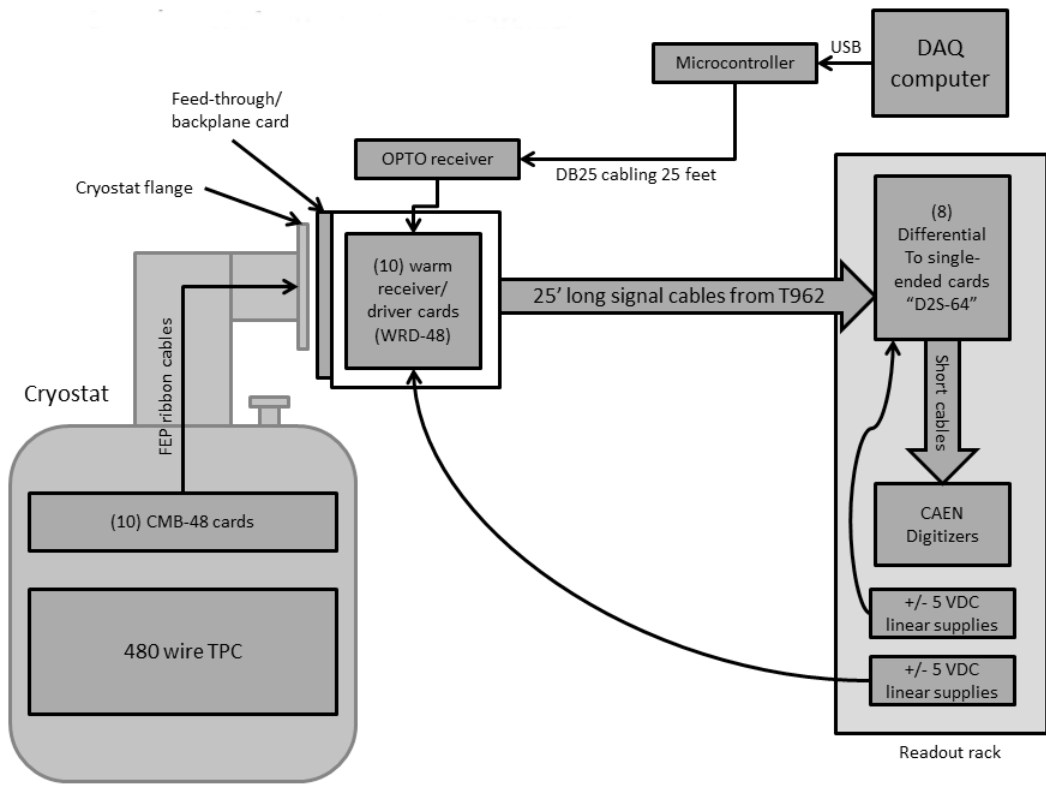


Figure 3.11: Overview of LArIAT Front End electronics.

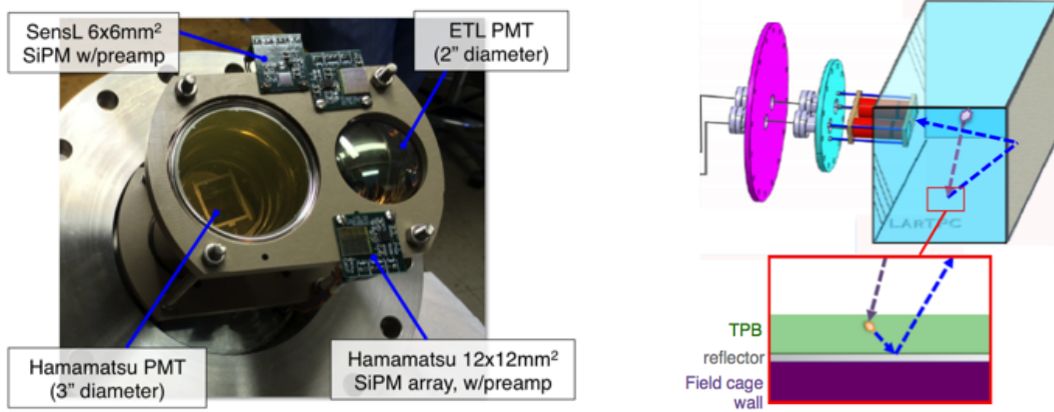


Figure 3.12: LArIAT’s photodetector system for observing LAr scintillation light inside the TPC (left), and a simplified schematic of VUV light being wavelength-shifting along the TPB-coated reflecting foils (right).

1612 are mounted on the PEEK support structure. PEEK screws into an access flange
 1613 as shown in Figure 3.12, on the anode side, leaving approximately 5 cm of clearance
 1614 from the collection plane.

1615 Liquid argon scintillates in vacuum-ultraviolet (VUV) range at 128 nm; since
 1616 cryogenic PMTs are not sensitive to VUV wavelengths, we need to shift the light to a
 1617 range that is visible to the PMTs. In LArIAT, the wavelength shifting is achieved by
 1618 installing highly-reflective 3M VIKUITI dielectric substrate foils coated with a thin
 1619 layer of tetraphenyl-butadiene (TPB) on the four unbiased walls of the TPC. The
 1620 scintillation light interaction with the TPB emits one or more visible photons, which
 1621 are then reflected into the chamber. Thus, the light yield increases and results in
 1622 higher uniformity of light across the TPC active volume, allowing the possibility of
 1623 light-based calorimetry, currently under study.

1624 For Run II, we coated the windows of the ETL PMT and the SensL SiPM with
 1625 a thin layer of TPB. In doing so, some of the VUV scintillation light converts into
 1626 visible right at the sensor faces, keeping information on the direction of the light
 1627 source. Information about the light directionality is hindered for the light reflected
 1628 on foils, as the reflection is uniform in angle.

1629 3.4 Trigger and DAQ

1630 The LArIAT DAQ and trigger system governs the read out of all the many subsystems
1631 forming LArIAT. The CAEN V1495 module [34] and its user-programmable FPGA
1632 are the core of this system. Every 10 ns, this module checks for matches between
1633 sixteen logical inputs and user-defined patterns in the trigger menu; if it finds a match
1634 for two consecutive clock ticks, that trigger fires.

1635 LArIAT receives three logic signals from the Fermilab accelerator complex related
1636 to the beam timing which we use as input triggers: a pulse just before the beam, a
1637 pulse indicating beam-on, and a beam-off pulse.

1638 The beam instruments, the cosmic ray taggers, and the light collection system
1639 provide the other NIM-standard logic pulse inputs to the trigger decision. We auto-
1640 matically log the trigger inputs configuration with the rest of the DAQ configuration
1641 at the beginning of each run.

1642 Fundamental inputs to the trigger card come from the TOF (see section 3.2.3)
1643 and the wire chambers (see section 3.2.2), as activity in these systems points to the
1644 presence of a charged particle in tertiary beam line. In particular, the discriminated
1645 pulses from the TOF PMTs form a NIM logic pulse for the trigger logic. We ask
1646 for a coincidence within a 20 ns window for all the pulses from the PMTs looking at
1647 the same scintillator block and use a delayed coincidence between the upstream and
1648 downstream paddle to inform the trigger decision. In order to form a coincidence
1649 between the upstream and downstream paddles, we delay the upstream paddle coin-
1650 cidence by 20 ns and widen it by 100 ns. The delay and widening are necessary to
1651 account for both lightspeed particles and slower particles (high-mass) to travel the
1652 6.5 m between the upstream and the downstream paddles. For the read out of the
1653 wire chambers, we use a total of sixteen multi-hit TDCs [74], four per chamber: two
1654 TDC per plane (horizontal and vertical), sixty-four wires per TDC. In each TDC, we
1655 keep the logical “OR” for any signal over threshold from the sixty-four wires. We

1656 then require a coincidence between the “OR” for the horizontal TDCs and the “OR”
1657 for the vertical TDCs: with this logic we make sure that at least one horizontal wire
1658 and one vertical wire saw significant signal in one wire chamber. The single logical
1659 pulse from each of the four wire chambers feeds into the first four inputs to the V1495
1660 trigger card. We require a coincidence within 20 ns of at least three logical inputs to
1661 form a trigger.

1662 The cosmic towers (see Section 3.2.5) provide another primary input to the trigger,
1663 in order to capture long tracks from cosmic muons crossing the TPC. We use NIM
1664 modules to require coincidences between one upper and one lower paddle set of any
1665 opposite cosmic towers. The OR all the opposite towers’ coincidences is fed as an
1666 input to the trigger card.

1667 We use the signal from the cryogenic PMTs (see Section 3.3.3) to form several
1668 interesting triggers. The coincidence of signals from all the PMT pulses within \sim 20 ns
1669 is an indication of ionizing radiation in the TPC and forms a trigger input. The
1670 coincidence of two subsequent scintillation logic pulses delayed by a maximum of $7 \mu\text{s}$
1671 forms the Michel electron trigger.

1672 **3.5 Control Systems**

1673 LArIAT is a complex ensemble of systems which needed to be monitored simultane-
1674 ously during data taking. We performed the monitoring of the systems operations
1675 with a slow control system, a DAQ monitoring system and a low level data quality
1676 monitoring described in the following sections.

1677 **Slow Control**

1678 We used the Synoptic Java Web Start framework [19] as a real-time display of subsys-
1679 tem conditions. Synoptic provides a Graphical User Interface that talks to the Fer-

1680 milab Accelerator Control System via the ACNET protocol. Its simple GUI allowed
 1681 us to change the operating parameters and to graph the trends of several variables of
 1682 interest for all of the tertiary beam detectors. Among the most important quantities
 1683 monitored by Synoptic there are the level of argon in both the inner vessel and the
 1684 external dewar, the operating voltages of cathode and wire planes, of the PMTs and
 1685 SiPMs, and of the four wire chambers, as well as the magnet temperatures. Figure
 1686 3.13 shows an example of the monitoring system. LArIAT uses the Accelerator
 1687 Control NETwork system (ACNET) to monitor the beam conditions of the MCcenter
 1688 beamline. For example, the horizontal and vertical position of the beam at the first
 1689 two wire chambers (WC1 and WC2) are shown in 3.14 as seen by the shifter during
 1690 data taking.

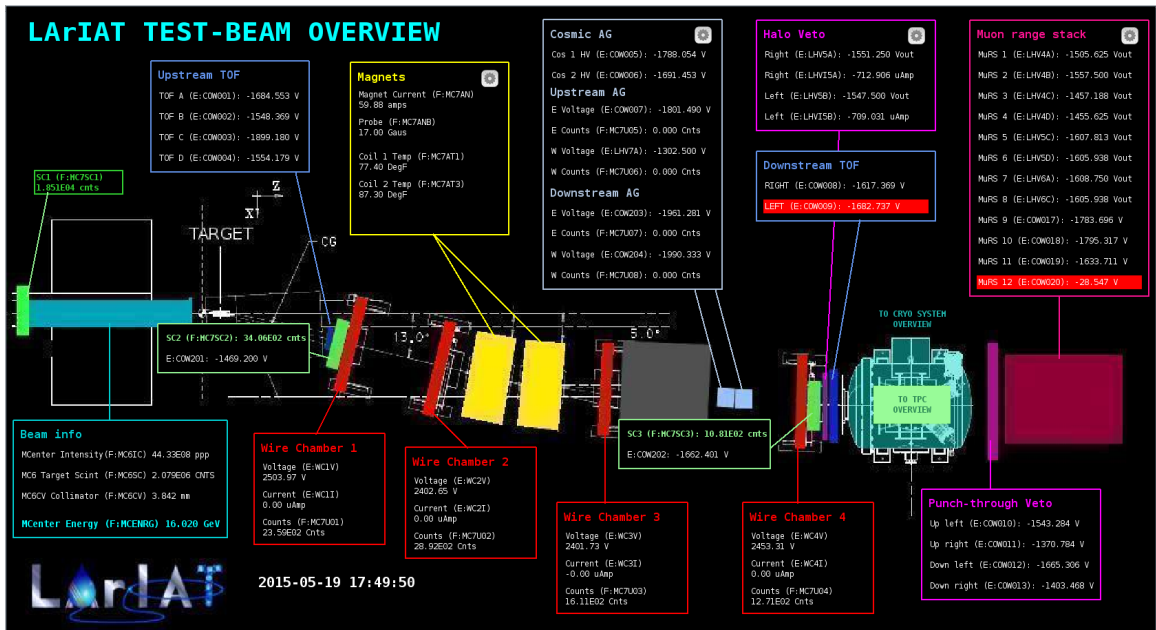


Figure 3.13: Interface of the Synoptic slow control system

1691 DAQ Monitoring

1692 We monitor the data taking and the run time evolution with the Run Status Webpage
 1693 (<http://lariat-wbm.fnal.gov/lariat/run.html>), a webpage updated in real-time. The

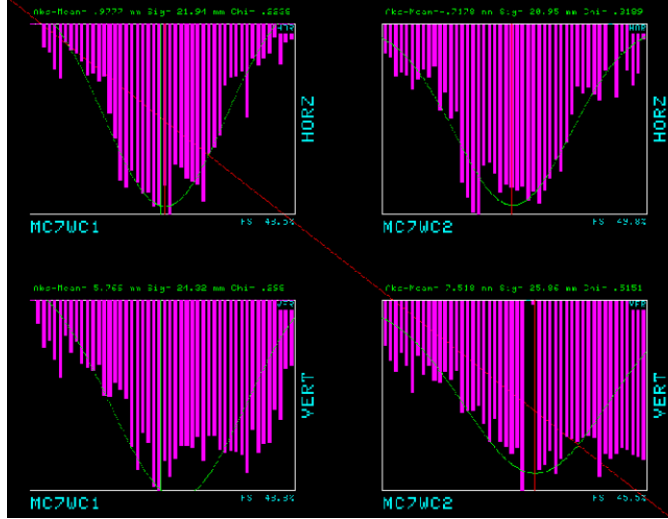


Figure 3.14: Beam position at the upstream wire chambers monitored with ACNET.

1694 page displays, among other information, the total number of triggers in the event,
 1695 the total number of detectors triggered during a beam spill, the trigger patterns, the
 1696 number of times a particular trigger pattern was satisfied during a beam spill, and
 1697 the current time relative to the Fermilab accelerator complex supercycle. A screen
 1698 shot of the page is show in figure 3.15.

1699 Data Quality Monitoring

1700 We employ two systems to ensure the quality of our data during data taking: the
 1701 Near-Real-Time Data Quality Monitoring and the Event Viewer.

1702 The Near-Real-Time Data Quality Monitoring (DQM) is a webpage which receives
 1703 updates from all the VME boards in the trigger system and displays the results of
 1704 a quick analysis of the DAQ stream of raw data on a spill-by-spill basis. The DQM
 1705 allows the shifter to monitor almost in real time (typically with a 2-minute delay)
 1706 a series of low level-quantities and compare them to past collections of beam spills.
 1707 Some of the variables monitored in the DQM are the pedestal mean and RMS on
 1708 CAEN digitizer boards of the TPC wires and PMTs of the beamline detectors, the
 1709 hit occupancy and timing plots on the wire chambers, and number of data fragments

1710 recorded that are used to build a TPC event. Abnormal values for low-level quantity
1711 in the data activates a series of alarms in the DQM; this quick feedback on the DAQ
1712 and beam conditions is fundamental to assure a fast debugging of the detector and a
1713 very efficient data taking during beam uptime.

1714 The online Event Viewer displays a two dimensional representation (Wire vs Time)
1715 of LArIAT TPC events on both the Induction and the Collection planes in near real
1716 time. The raw pulses collected by the DAQ on each wire are plotted as a function
1717 of drift time, resulting in an image of the TPC event easily readable by the shifter.
1718 This tool guarantees a particularly good check of the TPC operation which activate
1719 an immediate feedback for troubleshooting a number of issues. For example, it is
1720 easy for the shifter to spot high occupancy events and request a reduction of the
1721 primary beam intensity, or to spot a decrease of the argon purity which requires the
1722 regeneration of filters, or to catch the presence of electronic noise and reboot the
1723 ASICs. An example of high occupancy event is shown in 3.16.

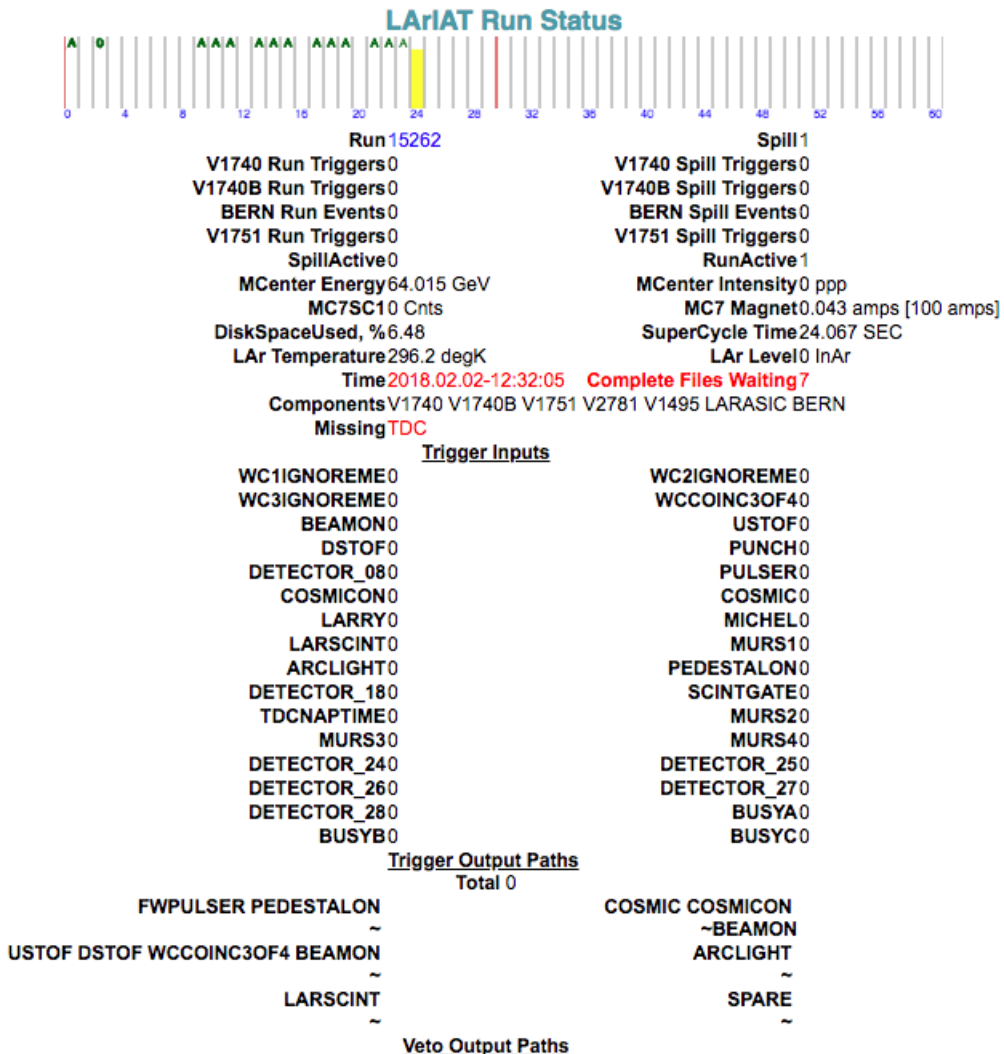


Figure 3.15: Run Status page at LArIAT downtime. At the top the yellow bar displays the current position in the Fermilab supercycle. Interesting information to be monitored by the shifter were the run number and number of spills, time elapsed from data taking (here in red), the energy of the secondary beam and the trigger paths.

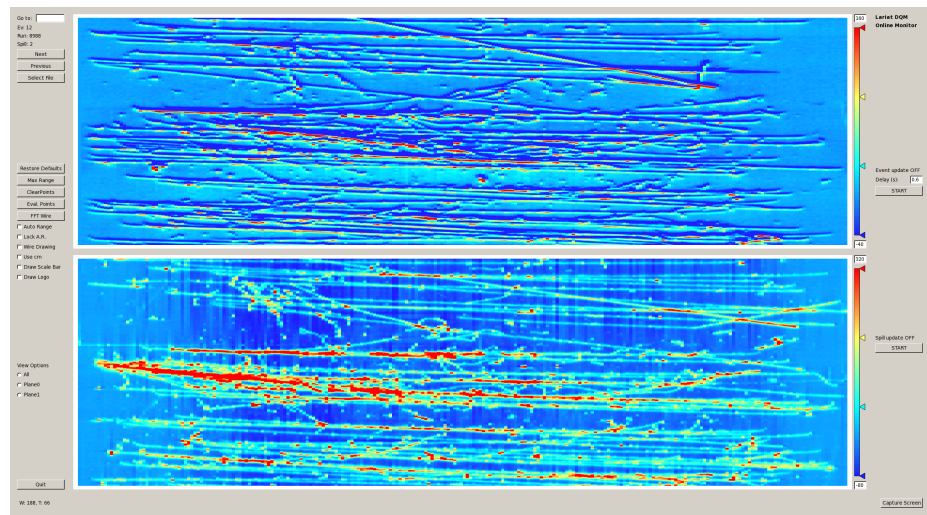


Figure 3.16: High occupancy event display: induction plane (top) and collection plane (bottom).

¹⁷²⁴ **Chapter 4**

¹⁷²⁵ **Total Hadronic Cross Section**

¹⁷²⁶ **Measurement Methodology**

¹⁷²⁷ “Like a lemon to the lime and the bubble to the bee”

¹⁷²⁸ – Eazy-E, 1993 –

¹⁷²⁹ This chapter describes the general procedure employed to measure a total hadronic
¹⁷³⁰ differential cross section in LArIAT. Albeit with small differences, both the (π^- ,Ar)
¹⁷³¹ and (K^+ ,Ar) total hadronic cross section measurements rely on the same procedure.
¹⁷³² We start by selecting the particle of interest using a combination of beamline detectors
¹⁷³³ and TPC information (Section 4.1). We then perform a handshake between the
¹⁷³⁴ beamline information and the TPC tracking to assure the selection of the correct
¹⁷³⁵ TPC track (Section 4.2). Finally, we apply the “thin slice” method and measure the
¹⁷³⁶ “raw” hadronic cross section (Section 4.3). A series of corrections are then evaluated
¹⁷³⁷ to obtain the “true” cross section (Section 4.3.3).

¹⁷³⁸ At the end of this chapter, we show a sanity check of the methodology by applying
¹⁷³⁹ the thin slice method employing only MC truth information and retrieving the Geant4
¹⁷⁴⁰ tabulated cross section for pions and kaons (Section 4.4).

1741 4.1 Event Selection

1742 The measurement of the (π^- ,Ar) and (K^+ ,Ar) total hadronic cross section in LArIAT
1743 starts by selecting the pool of pion or kaon candidates and measuring their momen-
1744 tum. This is done through the series of selections on beamline and TPC information
1745 described in the next sections. The summary of the event selection in data is reported
1746 in Table 4.1.

1747 4.1.1 Selection of Beamline Events

1748 As shown in equation 4.5, we leverage the beamline particle identification and mo-
1749 mentum measurement before entering the TPC as an input to evaluate the kinetic
1750 energy for the hadrons used in the cross sections measurements. Thus, we select the
1751 LArIAT data to keep only events whose wire chamber and time of flight information
1752 is registered (line 1 in Table 4.1). Additionally, we perform a check of the plausi-
1753 bility of the trajectory inside the beamline detectors: given the position of the hits
1754 in the four wire chambers, we make sure the particle's trajectory does not cross any
1755 impenetrable material such as the collimator and the magnets steel (line 2 in Table
1756 4.1).

	Run-II Neg Pol	Run-II Pos Pol
1. Events Reconstructed in Beamline	158396	260810
2. Events with Plausible Trajectory	147468	240954
3. Beamline $\pi^-/\mu^-/e^-$ Candidate	138481	N.A.
4. Beamline K^+ Candidate	N.A	2837
5. Events Surviving Pile Up Filter	108929	2389
6. Events with WC2TPC Match	41757	1081
7. Events Surviving Shower Filter	40841	N.A.
8. Available Events For Cross Section	40841	1081

Table 4.1: Number of data events for Run-II Negative and Positive polarity

1757 **4.1.2 Particle Identification in the Beamline**

1758 In data, the main tool to establish the identity of the hadron of interest is the LArIAT
1759 tertiary beamline, in its function of mass spectrometer. We combine the measurement
1760 of the time of flight, TOF , and the beamline momentum, p_{Beam} , to reconstruct the
1761 invariant mass of the particles in the beamline, m_{Beam} , as follows

$$m_{Beam} = \frac{p_{Beam}}{c} \sqrt{\left(\frac{TOF * c}{l}\right)^2 - 1}, \quad (4.1)$$

1762 where c is the speed of light and l is the length of the particle's trajectory between
1763 the time of flight paddles.

1764 Figure 4.1 shows the mass distribution for the Run II negative polarity runs on
1765 the left and positive polarity runs on the right. We perform the classification of events
1766 into the different samples as follows:

- 1767 • $\pi/\mu/e$: mass $< 350 \text{ MeV}/c^2$
1768 • kaon: $350 \text{ MeV} < \text{mass} < 650 \text{ MeV}/c^2$
1769 • proton: $650 \text{ MeV} < \text{mass} < 3000 \text{ MeV}/c^2$.

1770 Lines 3 and 4 in Table 4.1 show the number of negative $\pi/\mu/e$ and positive K
1771 candidates which pass the mass selection for LArIAT Run-II data.

1772 **4.1.3 TPC Selection: Halo Mitigation**

1773 The secondary beam impinging on LArIAT secondary target produces a plethora of
1774 particles which propagates downstream. The presence of upstream and downstream
1775 collimators greatly abates the number of particles tracing down the LArIAT tertiary
1776 beamline. However, it is possible that more than one particle sneaks into the LArTPC
1777 during its readout time: the TPC readout is triggered by the particle firing the

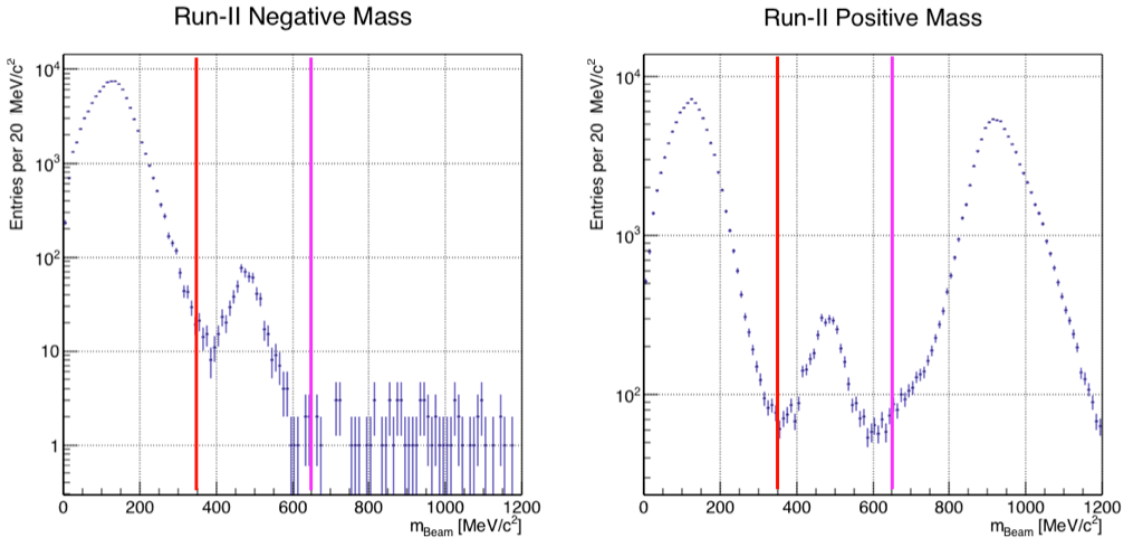


Figure 4.1: Distribution of the beamline mass as calculated according to equation 4.1 for the Run-II events reconstructed in the beamline, negative polarity runs on the left and positive polarity runs on the right. The classification of the events into $\pi^\pm/\mu^\pm/e^\pm$, K^\pm , or (anti)proton is based on these distributions, whose selection cut are represented by the vertical colored lines.

₁₇₇₈ beamline detectors, but particles from the beam halo might be present in the TPC at
₁₇₇₉ the same time. We call “pile up” the additional traces in the TPC. We adjusted the
₁₇₈₀ primary beam intensity between LArIAT Run I and Run II to reduce the presence of
₁₇₈₁ events with high pile up particles in the data sample. For the cross section analyses,
₁₇₈₂ we remove events with more than 4 tracks in the first 14 cm upstream portion of the
₁₇₈₃ TPC from the sample (line 5 in in Table 4.1).

₁₇₈₄ 4.1.4 TPC Selection: Shower Removal

₁₇₈₅ In the case of the (π^-, Ar) cross section, the resolution of beamline mass spectrometer
₁₇₈₆ is not sufficient to select a beam of pure pions. In fact, muons and electrons survive
₁₇₈₇ the selection on the beamline mass. It is important to notice that the composition of
₁₇₈₈ the negative polarity beam is mostly pions, as will be discussed in section 5.2.1. Still,
₁₇₈₉ we devise a selection on the TPC information to mitigate the presence of electrons

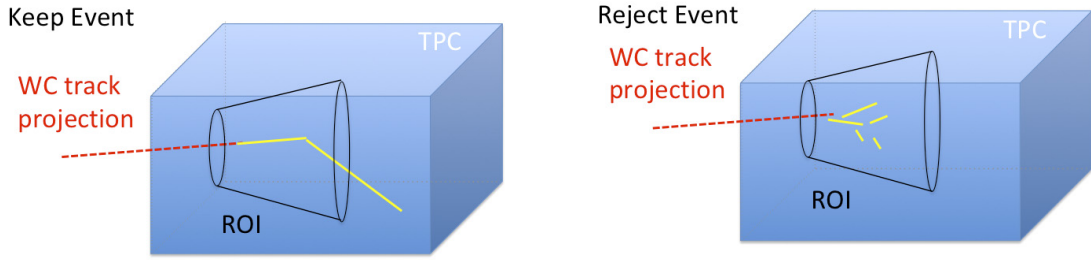


Figure 4.2: Visual rendering of the shower filter. The ROI is a cut cone, with a small radius of 4 cm, a big radius of 10 cm and an height of 42 cm (corresponding to 3 radiation lengths for electrons in Argon).

in the sample used for the pion cross section. The selection relies on the different topologies of a pion and an electron event in the argon: while the former will trace a track inside the TPC active volume, the latter will tend to “shower”, i.e. interact with the medium, producing bremsstrahlung photons which pair convert into several short tracks. In order to remove the shower topology, we create a region of interest (ROI) around the TPC track corresponding to the beamline particle. We look for short tracks contained in the ROI, as depicted in figure 4.4: if more than 5 tracks shorter than 10 cm are in the ROI, we reject the event. Line 7 in Table 4.1 shows the number of events surviving this selection.

4.2 Beamline and TPC Handshake: the Wire Chamber to TPC Match

For each event passing the selection on its beamline information, we need to identify the track inside the TPC corresponding to the particle which triggered the beamline detectors, a procedure we refer to as “WC to TPC match” (WC2TPC for short). In general, the TPC tracking algorithm will reconstruct more than one track in the event, partially due to the fact that hadrons interact in the chamber and partially because of pile up particles during the triggered TPC readout time, as shown in

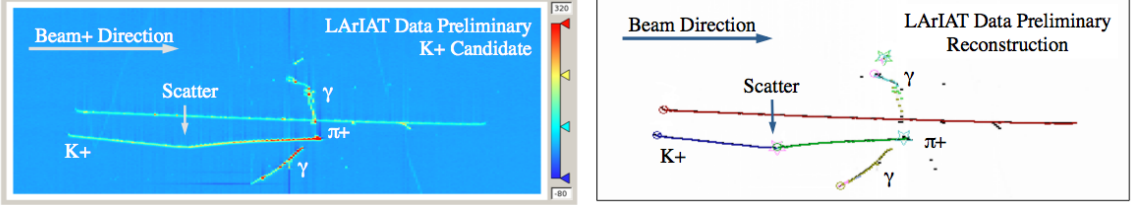


Figure 4.3: Kaon candidate event: on the right, event display showing raw quantities; on the left, event display showing reconstructed tracks. In the reconstructed event display, different colors represent different track objects. A kink is visible in the kaon ionization, signature of a hadronic interaction: the tracking correctly stops at the kink position and two tracks are formed. An additional pile-up track is so present in the event (top track in red).

1807 figure 4.3.

1808 We attempt to uniquely match one wire chamber track to one and only one recon-
 1809 structed TPC track. In order to determine if a match is present, we apply a geomet-
 1810 rical selection on the relative the position of the wire chamber and TPC tracks. We
 1811 start by considering only TPC tracks whose first point is in the first 2 cm upstream
 1812 portion of the TPC for the match. We project the wire chamber track to the TPC
 1813 front face where we define the coordinates of the projected point as x_{FF} and y_{FF} . For
 1814 each considered TPC track, we define ΔX as the difference between the x position of
 1815 the most upstream point of the TPC track and x_{FF} . ΔY is defined analogously. We
 1816 define the radius difference, ΔR , as $\Delta R = \sqrt{\Delta X^2 + \Delta Y^2}$. We define as α the angle
 1817 between the incident WC track and the TPC track in the plane that contains them.
 1818 If $\Delta R < 4$ cm, $\alpha < 8^\circ$, a match between WC-track and TPC track is found. We
 1819 describe how we determine the value for the radius and angular selection in Section
 1820 A.0.1. We discard events with multiple WC2TPC matches. We use only those TPC
 1821 tracks that are matched to WC tracks in the cross section calculation. Line 6 in Table
 1822 4.1 shows the number of events where a unique WC2TPC match was found.

1823 In MC, we mimic the matching between the WC and the TPC track by construct-
 1824 ing a fake WC track using truth information at wire chamber four. We then apply
 1825 the same WC to TPC matching algorithm as in data.

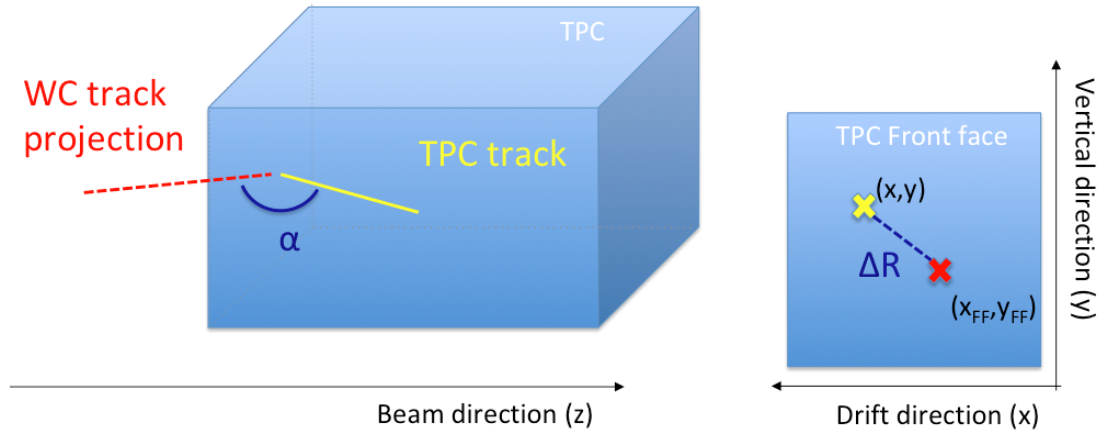


Figure 4.4: Visual rendering of the wire chamber to TPC match.

1826 4.3 The Thin Slice Method

1827 Once we have selected the pool of hadron candidates and we have identified the TPC
1828 track corresponding to the beamline event, we apply the thin slice method to measure
1829 the cross section, as the following sections describe.

1830 4.3.1 Cross Sections on Thin Target

1831 Cross section measurements on a thin target have been the bread and butter of
1832 nuclear and particle experimentalists since the Geiger-Marsden experiments [67]. At
1833 their core, this type of experiments consists in shooting a beam of particles with a
1834 known flux on a thin slab of material and recording the outgoing flux.

1835 In general even in the case of thin target, the target is not a single particle,
1836 but rather a slab of material containing many diffusion centers. The so-called “thin
1837 target” approximation assumes that the target centers are uniformly distributed in
1838 the material and that the target is thin compared to the projectile interaction length,
1839 so that no center of interaction sits in front of another. In this approximation, the
1840 ratio between the number of particles interacting in the target N_{Int} and the number of
1841 incident particles N_{Inc} on the target determines the interaction probability $P_{\text{Interacting}}$,

1842 which is the complementary to one of the survival probability $P_{Survival}$. Equation 4.2

$$P_{Survival} = 1 - P_{Interacting} = 1 - \frac{N_{Int}}{N_{Inc}} = e^{-\sigma_{TOT} n \delta X} \quad (4.2)$$

1843 describes the probability for a particle to survive the thin target. This formula relates
1844 the interaction probability to the total hadronic cross section (σ_{TOT}), the density of
1845 the target centers (n)¹ and the thickness of the target along the incident hadron
1846 direction (δX). If the target is thin compared to the interaction length of the process
1847 considered, we can Taylor expand the exponential function in equation 4.2 and find
1848 a simple proportionality relationship between the cross section and the number of
1849 incident and interacting particles, as shown in equation 4.3:

$$1 - \frac{N_{Int}}{N_{Inc}} = 1 - \sigma_{TOT} n \delta X + O(\delta X^2). \quad (4.3)$$

1850 Solving for the cross section, we find:

$$\sigma_{TOT} = \frac{1}{n \delta X} \frac{N_{Int}}{N_{Inc}}. \quad (4.4)$$

1851 4.3.2 Not-so-Thin Target: Slicing the Argon

1852 The interaction length of pions and kaons in argon is expected to be of the order
1853 of 50 cm for pions and 100 cm for kaons. Thus, the LArIAT TPC, with its 90 cm
1854 of length, is not a thin target. However, the fine-grained tracking of the LArIAT
1855 LArTPC allows us to treat the argon volume as a sequence of many adjacent thin
1856 targets.

1857 As described in Chapter 3, LArIAT wire planes consist of 240 wires each. The
1858 wires are oriented at +/- 60° from the vertical direction at 4 mm spacing, while the

1. The scattering center density in the target, n , relates to the argon density ρ , the Avogadro number N_A and the argon molar mass m_A as $n = \frac{\rho N_A}{m_A}$.

beam direction is oriented 3 degrees off the z axis in the XZ plane. The wires collect
 signals proportional to the energy loss of the hadron along its path in a $\delta X = 4$
 $\text{mm}/(\sin(60^\circ)\cos(3^\circ)) \approx 4.7$ mm slab of liquid argon. Thus, one can think to slice
 the TPC into many thin targets of $\delta X = 4.7$ mm thickness along the direction of the
 incident particle, making a measurement at each wire along the path.

Considering each slice j a “thin target”, we can apply the cross section calculation
 from Equation 4.4 iteratively, evaluating the kinetic energy of the hadron as it enters
 each slice, E_j^{kin} . For each WC2TPC matched particle, the energy of the hadron
 entering the TPC is known thanks to the momentum and mass determination by the
 tertiary beamline,

$$E_{FrontFace}^{kin} = \sqrt{p_{Beam}^2 - m_{Beam}^2} - m_{Beam} - E_{loss}, \quad (4.5)$$

where E_{loss} is a correction for the energy loss in the uninstrumented material between
 the beamline and the TPC front face. The energy of the hadron at each slab is
 determined by subtracting the energy released by the particle in the previous slabs.
 For example, at the j^{th} point of a track, the kinetic energy will be

$$E_j^{kin} = E_{FrontFace}^{kin} - \sum_{i < j} E_{Dep,i}, \quad (4.6)$$

where $E_{Dep,i}$ is the energy deposited at each argon slice before the j^{th} point as measured
 by the calorimetry associated with the tracking.

If the particle enters a slice, it contributes to $N_{Inc}(E^{kin})$ in the energy bin corresponding
 to its kinetic energy in that slice. If it interacts in the slice, it also contributes
 to $N_{Int}(E^{kin})$ in the appropriate energy bin. The cross section as a function of kinetic
 energy, $\sigma_{TOT}(E^{kin})$ will then be proportional to the ratio $\frac{N_{Int}(E^{kin})}{N_{Inc}(E^{kin})}$.

Our goal is to measure the total interaction cross section, independently from the
 topology of the interaction. Thus, we determine that a hadron interacted simply by

	min	max
X	1 cm	46 cm
Y	-15 cm	15 cm
Z	0 cm	86 cm

Table 4.2: Fiducial volume boundaries used to determine cross section interaction point.

requiring that the last point of the WC2TPC matched track lies inside the fiducial volume, whose boundaries are defined in Table 4.2. If the TPC track stops within the fiducial volume, its last point will be the interaction point; if the track crosses the boundaries of the fiducial volume, the track will be considered “through going” and no interaction point will be found. The only points of the hadronic candidate track considered to fill the N_{Inc}) and N_{Inc} plots are the ones contained in the fiducial volume.

4.3.3 Corrections to the Raw Cross Section

Equation 4.4 is a prescription for measuring the cross section in case of a pure beam of the hadron of interest and 100% efficiency in the determination of the interaction point. For example, if LArIAT had a beam of pure pions and were 100% efficient in determining the interaction point within the TPC, the pion cross section in each energy bin would be given by

$$\sigma_{TOT}^{\pi^-}(E_i) = \frac{1}{n\delta X} \frac{N_{\text{Int}}^{\pi^-}(E_i)}{N_{\text{Inc}}^{\pi^-}(E_i)}. \quad (4.7)$$

Unfortunately, this is not the case. In fact, the selection used to isolate pions in the LArIAT beam allows for the presence of some muons and electrons as background, while the kaon selection allows for a small percentage of protons (see Section 5.2.1). Also, the LArIAT TPC is not 100% efficient in determining the interaction point. Therefore we need to apply two corrections evaluated on the MC in order to

1899 extract the true cross section from LArIAT data: the background subtraction and
 1900 the efficiency correction. Still using the pion case as example, we estimate the pion
 1901 cross section in each energy bin changing Equation 4.7 into

$$\sigma_{TOT}^{\pi^-}(E_i) = \frac{1}{n\delta X} \frac{N_{Int}^{\pi^-}(E_i)}{N_{Inc}^{\pi^-}(E_i)} = \frac{1}{n\delta X} \frac{\epsilon^{Inc}(E_i)[N_{Int}^{TOT}(E_i) - B_{Int}(E_i)]}{\epsilon^{Int}(E_i)[N_{Inc}^{TOT}(E_i) - B_{Inc}(E_i)]}, \quad (4.8)$$

1902 where $N_{Int}^{TOT}(E_i)$ and $N_{Inc}^{TOT}(E_i)$ is the measured content of the interacting and
 1903 incident histograms for events that pass the event selection, $B_{Int}(E_i)$ and $B_{Inc}(E_i)$
 1904 represent the contributions from the background to the interacting and incident his-
 1905 tograms respectively, and $\epsilon^{Int}(E_i)$ and $\epsilon^{Inc}(E_i)$ are the efficiency corrections for said
 1906 histograms.

1907 As we will show in section 5.3, the background subtraction for the interacting
 1908 and incident histograms can be translated into a corresponding relative pion content
 1909 $C_{Interacting}^{\pi MC}(E_i)$ and $C_{Incident}^{\pi MC}(E_i)$ and the cross section re-written as follows

$$\sigma_{TOT}^{\pi^-}(E_i) = \frac{1}{n\delta X} \frac{\epsilon^{Inc}(E_i)}{\epsilon^{Int}(E_i)} \frac{C_{Int}^{\pi MC}(E_i)}{C_{Inc}^{\pi MC}(E_i)} \frac{N_{Int}^{TOT}(E_i)}{N_{Inc}^{TOT}(E_i)}. \quad (4.9)$$

1910 4.4 Procedure testing with truth quantities

1911 The (π^-, Ar) and (K^+, Ar) total hadronic cross section implemented in Geant4 can be
 1912 used as a tool to validate the measurement methodology. We describe here a closure
 1913 test done on Monte Carlo to prove that the methodology of slicing the TPC retrieves
 1914 the underlying cross section distribution implemented in Geant4 within the statistical
 1915 uncertainty.

1916 For pions and kaons in the considered energy range, the Geant4 inelastic model
 1917 adopted is “BertiniCascade”; the pion elastic cross sections are tabulated from on
 1918 Chips, while the kaon elastic cross sections are tabulated on Gheisha and Chips.

1919 For the validation test, we fire a sample of pions and a sample of kaons inside the

1920 LArIAT TPC active volume using the Data Driven Monte Carlo (see section 5.2.2).
1921 We apply the thin-sliced method using only true quantities to calculate the hadron
1922 kinetic energy at each slab in order to decouple reconstruction effects from possible
1923 issues with the methodology. For each slab of 4.7 mm length along the path of the
1924 hadron, we integrate the true energy deposition as given by the Geant4 transportation
1925 model. Then, we recursively subtracted it from the hadron kinetic energy at the TPC
1926 front face to evaluate the kinetic energy at each slab until the true interaction point is
1927 reached. Since the MC is a pure beam of the hadron of interest and truth information
1928 is used to retrieve the interaction point, no correction is applied. Doing so, we obtain
1929 the true interacting and incident distributions for the considered hadron, from which
1930 we derive the true MC cross section as a function of the hadron true kinetic energy.

1931 Figure 4.5 shows the total hadronic cross section for argon implemented in Geant4
1932 10.03.p1 (solid lines) overlaid with the true MC cross section as obtained with the
1933 sliced TPC method (markers) for pions on the left and kaons on the right; the total
1934 cross section is shown in green, the elastic cross section in blue and the inelastic
1935 cross section in red. The nice agreement with the Geant4 distribution and the cross
1936 section obtained with the sliced TPC method gives us confidence in the validity of
1937 the methodology.

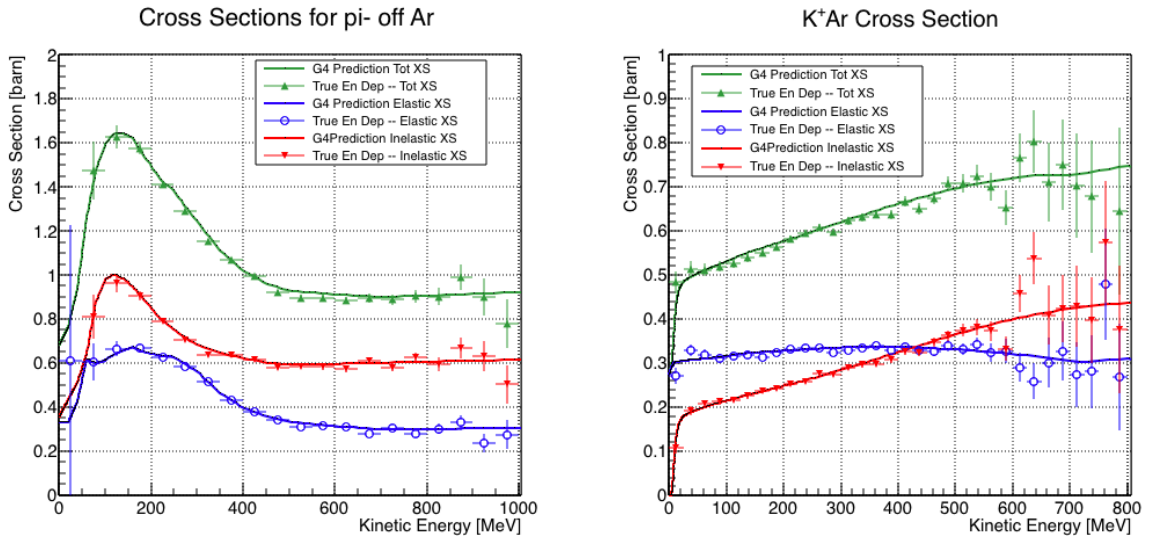


Figure 4.5: Hadronic cross sections for (π^- ,Ar) on the left and (K^+ ,Ar) on the right as implemented in Geant4 10.03.p1 (solid lines) overlaid the true MC cross section as obtained with the sliced TPC method (markers). The total cross section is shown in green, the elastic cross section in blue and the inelastic cross section in red.

¹⁹³⁸ **Chapter 5**

¹⁹³⁹ **Data and MC preparation for the**
¹⁹⁴⁰ **Cross Section Measurements**

¹⁹⁴¹ “*Il dolce non lo mangi mai, ma qualche volta ti rifai.*
¹⁹⁴² *Abbracciami*”
¹⁹⁴³ – Pietro Ciampi, 1971 –

¹⁹⁴⁴ This chapter describes the work done on the data and Monte Carlo samples in
¹⁹⁴⁵ preparation for the cross section analyses. This entails the choice of the datasets
¹⁹⁴⁶ and the production of the information needed to construct the Monte Carlo Simula-
¹⁹⁴⁷ tion (Section 5.1), the construction and use of said Monte Carlo simulation (section
¹⁹⁴⁸ 5.2), the study of backgrounds for the pion cross section (Section 5.3), the study of
¹⁹⁴⁹ the energy loss between WC4 and TPC (Section 5.4), the study of the tracking in the
¹⁹⁵⁰ TPC (Section 5.5), and study of the calorimetry response (Section 5.6).

¹⁹⁵¹ **5.1 Cross Section Analyses Data Sets**

¹⁹⁵² We choose LArIAT Run-II as the data period for the (π^- ,Ar) and (K^+ ,Ar) total
¹⁹⁵³ hadronic cross section analyses. Data taking for the this period started on 03/15/2016

1954 and ended on 07/31/2016. Since we are interested in beamline and TPC information,
1955 we ask basic requirements on the operational status of the time of flight, wire chambers
1956 and TPC to form the good run list for this period, which we informally call “lovely
1957 runs”.

1958 The subset of lovely runs chosen for the (π^-, Ar) total hadronic cross section
1959 analysis includes only the -60A and -100A magnet configurations in negative polarity,
1960 even if LArIAT explored several other beamline configurations during Run-II. The -
1961 60A and -100A combined data set accounts for approximately 90% of the total Run-II
1962 negative polarity runs. The choice of the main two beamline settings limits the need
1963 for the production of many different MC sets and related corrections, still maintaining
1964 a high number of events.

1965 Similarly, the subset of lovely runs chosen for the (K^+, Ar) total hadronic cross
1966 section analysis includes only the +60A and +100A magnet configurations in positive
1967 polarity. It should be noted that kaons are extremely rare in the +60A sample, thus
1968 the data sample for the (K^+, Ar) cross section after the mass selection is about 90%
1969 +100A runs, as shown in Table 5.1.

1970 For the first measurements in LArIAT that uses both beamline and TPC infor-
1971 mation, we choose strict requirements on the reconstruction of the WC tracks, the
1972 so-called “Picky Track” sample (see Section 3.2.2). This choice presents two ad-
1973 vantages: the uncertainty on the momentum reconstruction for the “Picky Tracks”
1974 sample is smaller compared to the “High Yield” sample, and the comparison with
1975 the beamline MC results is straightforward. A possible future update and cross check
1976 of these analysis would be the use of the High Yield sample, where the statistics is
1977 about three times higher.

1978 The breakdown of beamline events as a function of the magnets settings is shown
1979 in Table 5.1. The choice of the data sets determines the production of beamline MC
1980 and serves as basis for the production of Data Driven MC, as shown in the next

1981 sections.

1982 **5.2 Construction of a Monte Carlo Simulation for** 1983 **LArIAT**

1984 For the simulation of LArIAT events and for the simulation of the datasets' particle
1985 make up, we use a combination of two MC generators: the G4Beamline Monte Carlo
1986 and the Data Driven single particle Monte Carlo (DDMC). We use the G4Beamline
1987 MC to simulate the particle transportation in the beamline and calculate the particle
1988 composition of the beam just after the fourth Wire Chamber (WC4). In order to
1989 simulate the beamline particles after WC4 and in the TPC, we use the DDMC.

1990 **5.2.1 G4Beamline**

1991 G4Beamline simulates the beam collision with the LArIAT secondary target, the
1992 energy deposited by the particles in the LArIAT beamline detectors, and the action
1993 of the LArIAT magnets, effectively accounting for particle transportation through the
1994 beamline from the LArIAT target until “Big Disk”, a fictional, void detector located
1995 just before the LArIAT cryostat. At the moment of this writing, G4Beamline does
1996 not simulated the responses of the beamline detectors. It is possible to interrogate the
1997 truth level information of the simulated particles in several points of the geometry.
1998 In order to ease the handshake between G4Beamline and the DDMC, we ask for
1999 the beam composition just after WC4. Since LArIAT data are taken under different

	I = 60 A	I = 100 A	Total
Data Events after $\pi/\mu/e$ Mass Selection	67068	71413	138481
Data Events after K Mass Selection	274	2563	2837

Table 5.1: Number of data events which fit the $\pi/\mu/e$ or K mass hypothesis as a function of magnet settings.

beam conditions, we need to simulate separately the beam composition according to the magnets' settings and the secondary beam intensity with G4Beamline. For the pion cross section analysis the relevant beam conditions are secondary beam energy of 64 GeV, negative polarity magnet with current of 100 A and 60 A. For the kaon cross section analysis the relevant beam conditions is a secondary beam energy of 64 GeV, positive polarity magnet with current of 100 A.

Beam Composition for Negative Pion Cross Section

Even if pions are by far the biggest beam component in negative polarity runs, the LArIAT tertiary beam is not a pure pion beam. While useful to discriminate between pions, kaons, and protons, the beamline detectors are not sensitive enough to discriminate among the lighter particles in the beam: electrons, muons and pions fall under the same mass hypothesis. Thus, we need to assess the contamination from beamline particles other than pions in the event selections used for the pion cross section analysis and correct for its effects. The first step of this process is assessing the percentage of electrons and muons in the $\pi/\mu/e$ beamline candidates via the G4Beamline MC. Since the beamline composition is a function of the magnet settings, we simulate separately events for magnet current of -60A and -100A. Figure 5.1 shows the momentum predictions from G4Beamline overlaid with data for the 60A runs (left) and for the 100A runs (right). The predictions for electrons, muons and pions have been staggered and their sum is area normalized to data. Albeit not perfect, these plots show a reasonable agreement between the momentum shapes in data and MC. We attribute the difference in shape to a two approximations performed in the MC. Firstly, G4Beamline lacks the simulation of the WC efficiency which is momentum dependent and leads to enhance the number events in the center of the momentum distribution. Secondly, G4Beamline stop tracking pions and their products if they decay in after WC1; in data, pion decays in flight can still create a

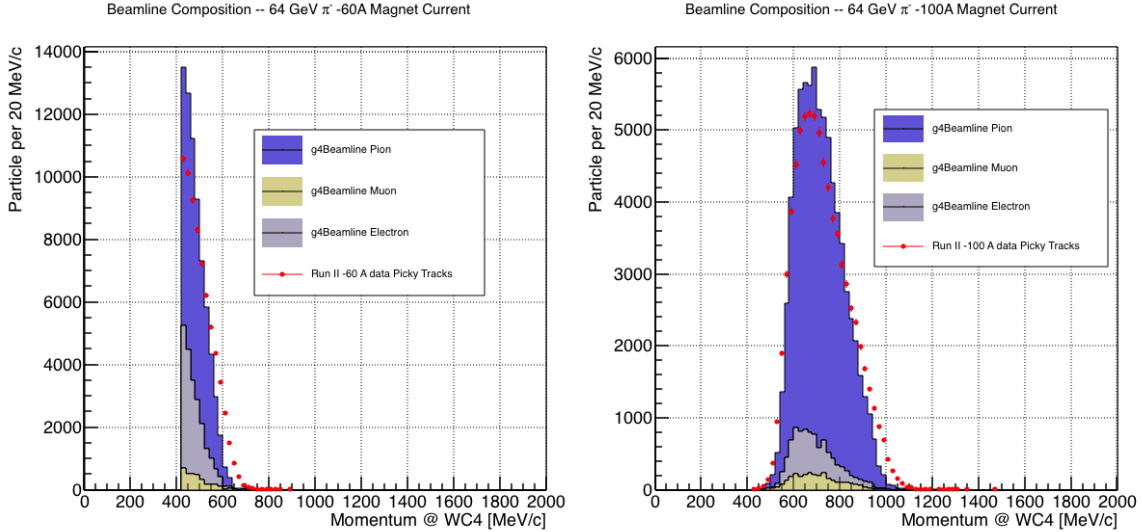


Figure 5.1: Beam composition for the -60A runs (left) and -100A runs (right). The solid blue plot represents the simulated pion content, the yellow plot represents the simulated muon content and the grey plot represents the simulated electron content. The plots are area normalized to the number of data events, shown in red.

	I = -60 A	I = -100 A
G4Pions	68.8 %	87.4 %
G4Muons	4.6 %	3.7 %
G4Electrons	26.6 %	8.9 %

Table 5.2: Simulated beamline composition per magnet settings

2026 trigger if the produced muon travels thought the beamline detectors. In the pion cross
 2027 section analysis, these differences between data and G4Beamline are accounted for as
 2028 a systematic uncertainty related to the beam composition (see Section 6.2.1).

2029 Table 5.2 shows the beam composition per magnet setting after the mass selection
 2030 according to the G4Beamline simulation.

2031 The estimated beam composition is used as a basis to estimate the background
 2032 contamination in the (π^-, Ar) cross section measurement, whose full treatment is
 2033 described in section 5.3.

2034 **Beam Composition for Positive Kaon Cross Section**

2035 In the positive polarity runs, the tertiary beam composition is mainly pions and
2036 protons. The left side of Figure 5.2 shows the predictions for the momentum spectra
2037 for the 100A positive runs according to G4Beamline (solid colors) overlaid with data
2038 (black points). Since the LArIAT beamline detectors can discriminate between kaons
2039 and other particles, we do not rely on the G4Beamline simulation to estimate the
2040 beamline contamination in the pool of kaon candidates (as in the case of the pion
2041 cross section), but rather we use a data driven approach. The basic idea of this data
2042 driven approach is to estimate the bleed over from high and low mass peaks under
2043 the kaon peak by fitting the tails of the $\pi/\mu/e$ and proton mass distributions, as
2044 shown in Figure 5.2 right side. Since the shape of the tails is unknown, the estimate
2045 is done multiple times varying the range and shape for reasonable functions. For
2046 example, to estimate the proton content under the kaon peak, we start by fitting the
2047 left tail of the proton mass distribution with a gaussian function between $650 \text{ MeV}/c^2$
2048 and $750 \text{ MeV}/c^2$. We extend the fit function under the kaon peak and integrate the
2049 extended fit function between $350-650 \text{ MeV}/c^2$. We integrate the mass histogram
2050 in the same range and calculate the proton contamination as the ratio between the
2051 two integrals. We repeat this procedure for several fit shapes (gaussian, linear and
2052 exponential functions) and tail ranges. Finally, we calculate the contamination as
2053 the weighted average of single estimates, where the weights are calculated to be the
2054 $1./|1 - \chi^2|$ of the tail fits. The procedure is repeated for lighter particles mass peak
2055 independently. With 12 iterations of this method we find a proton contamination of
2056 $5.0 \pm 2.0 \%$ and a contamination from the lighter particles of $0.2 \pm 0.5 \%$. The
2057 estimate of the proton background is currently not used in the kaon cross section
2058 analysis, but it is a fundamental step to retrieve the true kaon cross section which
2059 will be implemented in the further development of the analysis.

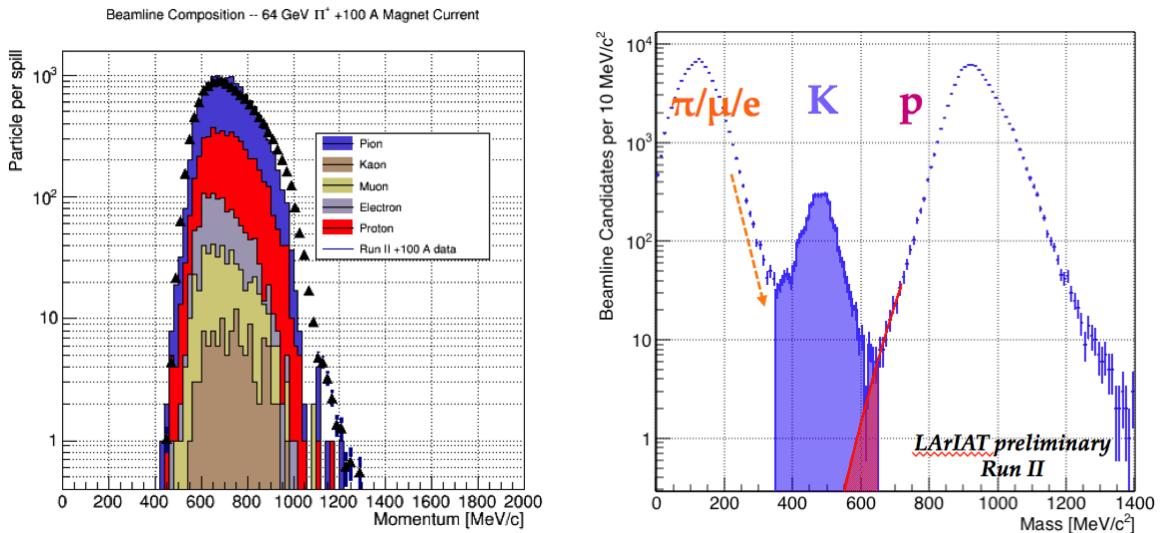


Figure 5.2: *Left:* Beam composition for the +100A runs after WC4 (no mass selection applied). The solid colors represent the contributions from the G4Beamline simulated particles: blue plot represents the simulated pion content, the yellow plot represents the simulated muon content and the grey plot represents the simulated positron content, the red the proton content and the mustard the kaon content. The plots are area normalized to the number of data events, shown in black. *Right:* Mass distribution for the Run-II positive runs, where the area under the kaon mass peak is highlighted in purple. The area under the extension of a possible fit for the proton tail is highlighted in red.

2060 **5.2.2 Data Driven MC**

2061 The Data Driven single particle Monte Carlo (DDMC) is a single particle gun which
2062 simulates the particle transportation from WC4 into the TPC leveraging on the beam-
2063 line data information. The DDMC uses the data momentum and position at WC4
2064 to derive the event generation: a general sketch of the DDMC workflow is shown in
2065 Figure 5.3.

2066 When producing a DDMC sample, beamline data from a particular running pe-
2067 riod and/or running condition are selected first. For example, data for the negative
2068 60A runs and for the negative 100A runs inform the event generation stage of two
2069 different DDMC samples. Figure 5.4 schematically shows the data quantities of in-
2070 terest leveraged from data: the momentum (P_x, P_y, P_z) and position (X, Y) at WC4.
2071 For each data event, we obtain the particle position (X, Y) at WC4 directly from the
2072 data measurement; we calculate the components of the momentum using the beam-
2073 line measurement of the momentum magnitude in conjunction with the hits on WC3
2074 and WC4 to determine the direction of the momentum vector, as described in section
2075 3.2.2. The momentum and position of the selected data form a 5-dimensional tuple,
2076 which we sample thousands of times through a 5-dimensional hit-or-miss sampling
2077 procedure to generate the MC events. This sampling generates MC events with the
2078 same momentum and position distributions as data, with the additional benefit of
2079 accounting for the correlations between the P_x, P_y, P_z, X, Y variables. As an example,
2080 the results of the DDMC generation compared to data for the kaon +100A sample
2081 are shown in figure 5.5 for the P_z, X and Y distributions; as expected, MC and data
2082 agree within the statistical uncertainty by construction. A LArSoft simulation mod-
2083 ule then launches single particle MC from $z = -100$ cm (the location of the WC4)
2084 using the generated events. The particles are free to decay and interact in their path
2085 from WC4 to the TPC according to the Geant4 simulation.

2086 Using the DDMC technique ensures that the MC and data particles have very

2087 similar momentum, position and angular distributions at WC4 and allows us to use
 2088 the MC sample in several occasions: to estimate the background contamination to
 2089 the pion cross section (see Section 5.3), to calibrate the energy loss upstream of the
 2090 TPC (see Section 5.4), or to study the tracking and the calorimetric performance
 2091 (sections 5.5 and 5.6). A small caveat is in order here: the DDMC is a single particle
 2092 Monte Carlo, which means that the beam pile-up is not simulated.

2093 We generate six samples for the pion cross section measurement: three samples
 2094 of ~ 330000 pions, muons and electrons to simulate the negative 60A runs, and three
 2095 samples of ~ 340000 pions, muons and electrons for the negative 100A runs. We
 2096 generate a sample of 195000 kaons for the kaon cross section analysis.

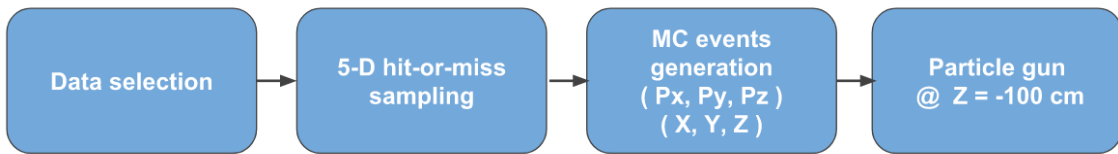


Figure 5.3: Workflow for Data Driven single particle Monte Carlo production.

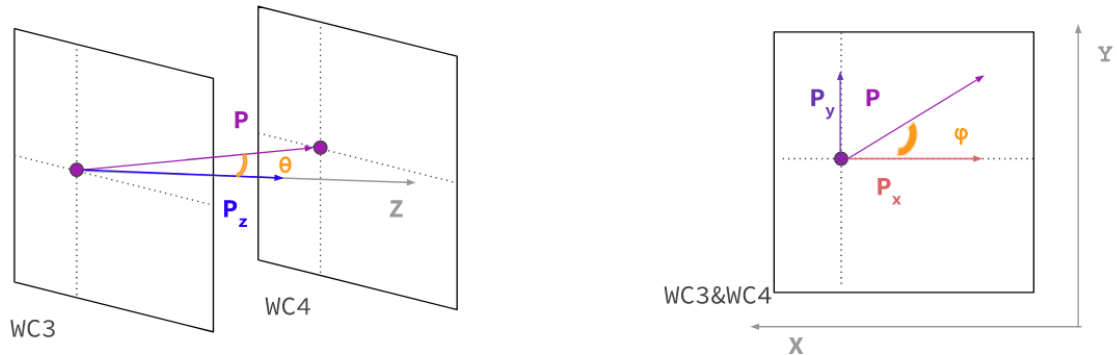


Figure 5.4: Scheme of the quantities of interest for the DDMC event generation:
 P_x, P_y, P_z, X, Y at WC4.

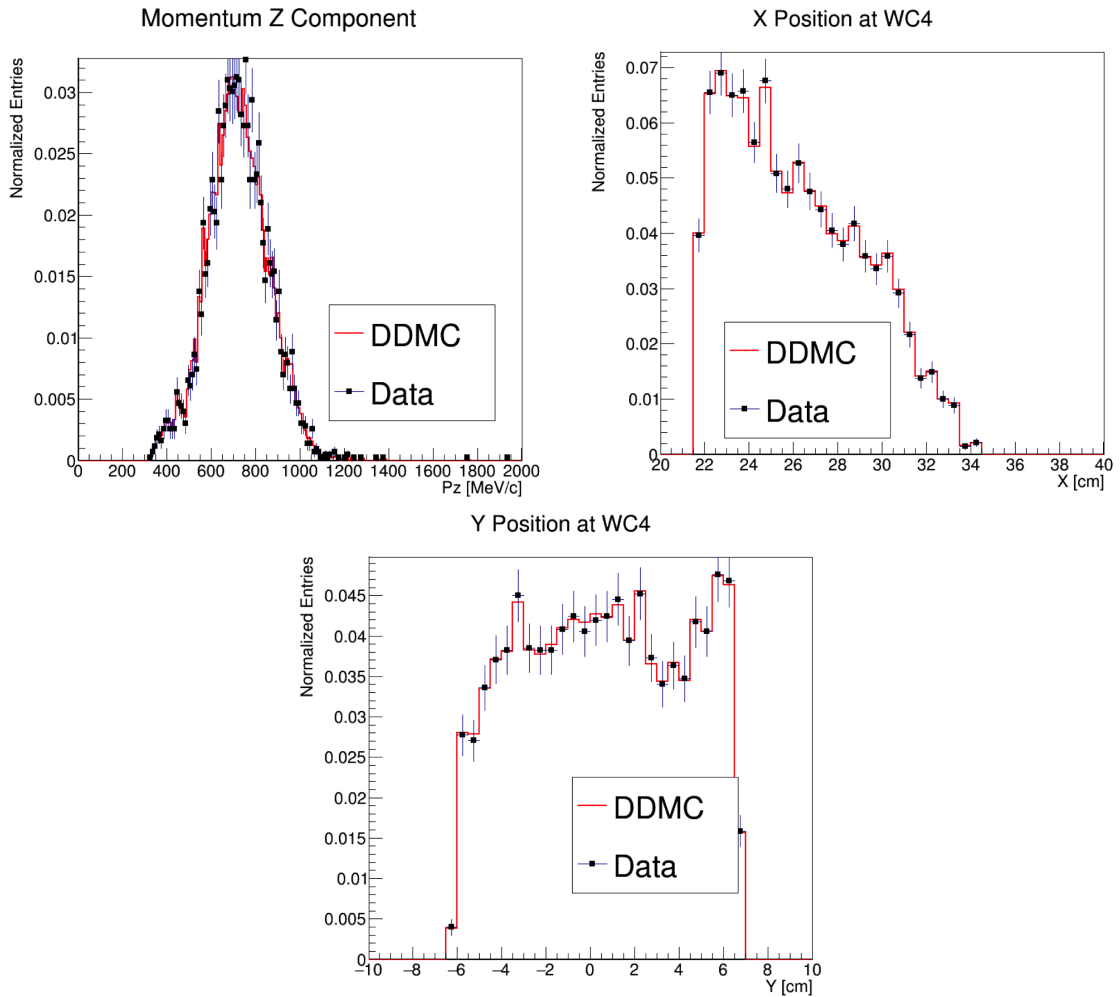


Figure 5.5: Comparison between generated quantities and data distributions for the 100A kaon sample: Z component of the momentum at WC4 (top left), X position at Wire Chamber 4 (top right), Y position at Wire Chamber 4 (bottom).

2097 **5.3 Estimate of Backgrounds in the Pion Cross**
2098 **Section**

2099 We use the beamline simulation and the DDMC simulation to estimate the back-
2100 ground in the total hadronic pion cross section. Two categories of background exists
2101 for the negative pion cross section measurement: the one related to the pion interac-
2102 tion in the chamber, discussed in Section 5.3.1 and the one related to the beamline
2103 contamination, discussed in Section 5.3.2.

2104 **5.3.1 Background from Pion Capture and Decay**

2105 Our goal is to measure the total hadronic cross section for negative pions in argon.
2106 Since pion capture can be classified as an electromagnetic process and pion decay is a
2107 weak process, capture and decay represent unwanted interactions. We present here a
2108 study of capture and decay in Monte Carlo and the solution we adopted to mitigate
2109 their occurrence in the data sample.

2110 For this MC study, we use a sample of MC pions generated according to the
2111 $-60A$ beam profile with the DDMC (see Section 5.2.2). It is important to notice
2112 that capture occurs predominantly at rest, while decay may occur both in flight and
2113 at rest. Thus, we can highly mitigate capture and decay at rest by removing pions
2114 which would release all their energy in the TPC and stop. This translates into a
2115 momentum selection, where we keep only events whose WC momentum is above a
2116 certain threshold. Figure 5.6 shows the true momentum distribution for the primary
2117 pions¹ that arrive to the TPC (pink), that capture (green) or decay (blue) inside the
2118 TPC, on a linear scale (left) and on a log scale (right) vertical axis.

1. We use here the Geant4 denomination “primary” to indicate that the pion considered does not undergo interactions modifying its energy before getting to the TPC. In fact, not every pion shot from wire chamber four will arrive to the TPC as primary, some will decay or interact before the TPC.

2119 In order to choose the selection value for the wire chamber momentum, it is
2120 beneficial to estimate the ratio of events which capture or decay that survive the
2121 selection in MC as a function of the momentum threshold, and compare it with the
2122 survival ratio for all the 60A events. This is done in figure 5.7. We define the survival
2123 ratio simply as the number of events surviving the true momentum selection divided
2124 by the number of events of that category. We calculate the survival ratio separately
2125 for the three event categories explained above: total (pink), capture (green) and decay
2126 (blue). Selecting pions with momentum greater than 420 MeV/c reduces the capture
2127 events by 99% while maintaining about 80% of the 60A data sample and almost
2128 the entire 100A sample. Figure 5.8 shows the ratio of events which end their life in
2129 capture (green) or decay (blue) over the total number of events as a function of
2130 the true momentum at wire chamber four. This ratio is slightly dependent on the
2131 inelastic cross section implemented in Geant4, as we are able to register a pion capture
2132 (or decay) only if it did not interact inelastically in the TPC. We choose a momentum
2133 threshold of 420 MeV/c because the percentage of capture events drops below 1% and
2134 the percentage of decays is never above 2% for momenta greater than 420 MeV/c.
2135 After the momentum selection, we evaluate the contribution of capture and decay to
2136 be a negligibly small background to the cross section measurement compared to the
2137 background related to the beamline which we will address in the next section.

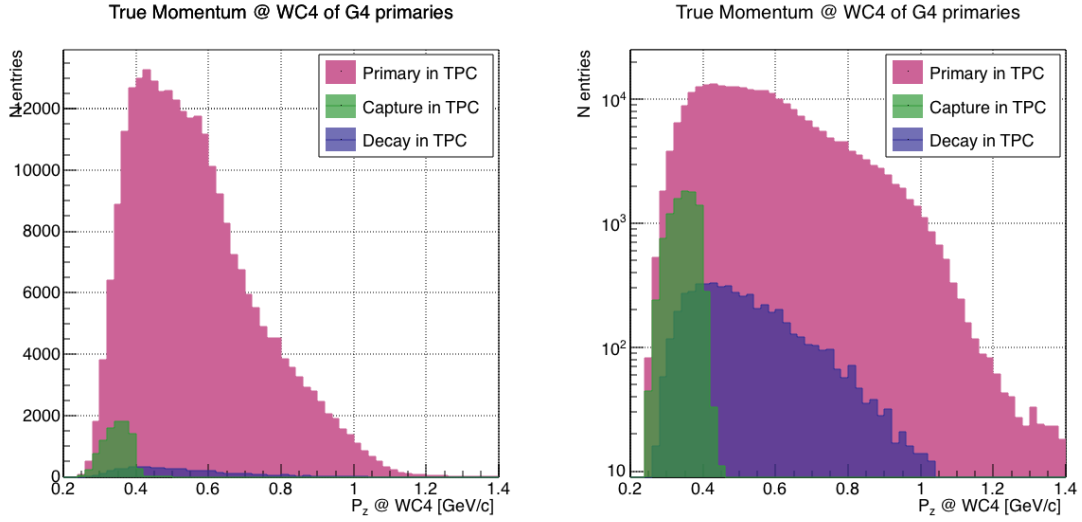


Figure 5.6: True momentum distribution at wire chamber 4 for every simulated pion arriving in the TPC (pink), ending its life in capture (green) or in decay (blue) in the TPC, linear vertical axis on the left, logarithmic on the right.

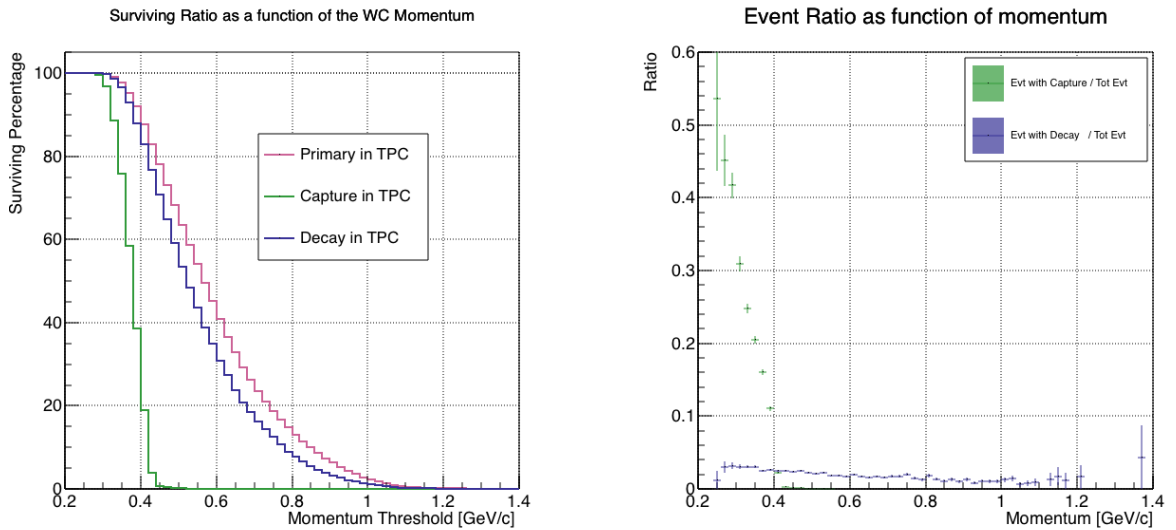


Figure 5.7: Survival ratio as a function of selection threshold on true momentum at wire chamber four for every simulated pion arriving in the TPC (pink), capture (green) or in decay (blue).

Figure 5.8: Ratio between the capture (green) and decay (blue) events over the total number of events as a function of the true momentum at wire chamber four.

2138 **5.3.2 Contributions from the Beamline Background**

2139 We define beamline background every TPC track matched to the WC track which is
2140 not a primary pion. Potentially, there are 4 different types of beamline background:

2141 1) electrons,

2142 2) muons,

2143 3) secondaries from pion events,

2144 4) matched pile up events.

2145 The first step to quantify the effect of the beamline background on the pion cross
2146 section is to estimate what percentage of events used in the cross section calculation
2147 is not a primary pion. We start by noting that the last type of background, the
2148 “matched pile up” events, is a negligible fraction, because of the definition of the
2149 WC2TPC match: we deem the probability of a single match with a halo particle in
2150 the absence of a beamline particle² negligibly small. As shown in Section 5.2.1, we
2151 use G4Beamline to estimate the percentage of pions, muons and electrons at WC4,
2152 obtaining the composition shown in Table 5.2. The next step is to simulate those
2153 pions, muons and electrons from WC4 to the TPC with the DDMC and evaluate their
2154 contribution to the cross section. To do so, we start by simulating the same number
2155 of electrons, muons and pions with the DDMC and we apply the same selection chain
2156 (i.e. track multiplicity rejection, WC2TPC acceptance and shower rejection) on the
2157 three samples. The number of events per particle species surviving this selection is
2158 shown on table 5.3. In order to reproduce the closest make up of the beam to data,
2159 we weight each event of a given particle species according to the estimated beam
2160 composition. In case of 60A runs, for example, the weights are 0.688 for pions, 0.046
2161 for muons and 0.266 for electrons.

2. Events with multiple WC2TPC matches are always rejected.

	Magnet Current -60A			Magnet Current -100 A		
	MC π^-	MC μ^-	MC e^-	MC π^-	MC μ^-	MC e^-
Total Initial events	334500	334500	334500	344500	344500	344500
After Multiplicity Rejection	330668	333420	198065	326576	344208	201380
After WC2TPC Selection	218239	296333	91139	230418	300228	98834
Evts After Shower Rejection	208063	288914	20293	219882	293585	17780
Selection Survival Rate	62.3%	86.6%	6.1%	63.8%	85.5%	5.2%
Beam Composition @WC4	68.8%	4.6 %	26.6 %	87.4 %	3.7 %	8.9 %
Beam Composition @TPC FF	88.5%	8.2%	3.3 %	94.0%	5.3%	0.7%

Table 5.3: MC selection flow per particle species.

2162 It should be noted that pions may interact hadronically in the steel or in the
 2163 non-instrumented argon upstream to the TPC front face while travelling the length
 2164 of between WC4 and the TPC. Or, they could decay in flight between WC4 and the
 2165 TPC. One of the interaction products can leak into the TPC and be matched with the
 2166 WC track, contributing to the pool of events used for the cross section calculation. We
 2167 call this type of particles “secondaries” from pion events, with a terminology inspired
 2168 by Geant4. We estimate the number of secondaries using the DDMC pion sample.
 2169 The percentage of secondaries is given by the number of matched WC2TPC tracks
 2170 whose corresponding particle is not flagged as primary by Geant4. The secondary to
 2171 pion ratio is 4.9% in the 60A sample and 4.3% in the 100A sample.

2172 We evaluate the beamline background contribution to the cross section by pro-
 2173 ducing the interacting and incident histograms for the events surviving the selection,
 2174 staggering the contributions for each particle species, as shown in Figure 5.9. From
 2175 those histograms, we are able to evaluate the contribution of pions and beamline
 2176 backgrounds to each bin of the interacting and incident histograms separately and
 2177 obtain the relative pion content. The relative pion content in each bin for the inter-
 2178 acting and incident histograms represents the correction applied to data. We take

here the interacting histogram as example, noting that the derivation of the correction for the incident histogram is identical. The number of entries in each bin of the interacting plot (Figure 5.9 left) is $N_{\text{Int}}^{\text{TOT}}(E_i)$, equal to the sum of the pions and beamline backgrounds in that bin, namely

$$N_{\text{Int}}^{\text{TOT}}(E_i) = N_{\text{Int}}^{\pi}(E_i) + \underbrace{N_{\text{Int}}^{\mu}(E_i) + N_{\text{Int}}^e(E_i) + N_{\text{Int}}^{\text{Secondary}}(E_i)}_{B_{\text{Int}}(E_i)}. \quad (5.1)$$

Thus, the relative pion content to each bin in MC can be calculated as follows

$$C_{\text{Int}}^{\pi MC}(E_i) = \frac{N_{\text{Int}}^{\pi MC}}{N_{\text{Int}}^{\text{TOTMC}}(E_i)} = \frac{N_{\text{Int}}^{\text{TOTMC}}(E_i) - B_{\text{Int}}^{MC}(E_i)}{N_{\text{Int}}^{\text{TOTMC}}(E_i)}. \quad (5.2)$$

In order to evaluate the pion content of each bin in data, we scale the measured bin by the corresponding relative pion content found in MC, as follows

$$N_{\text{Int}}^{\pi RecoData} = N_{\text{Int}}^{\text{TOTData}}(E_i) - B_{\text{Int}}^{\text{Data}}(E_i) = C_{\text{Int}}^{\pi MC}(E_i)N_{\text{Int}}^{\text{TOTData}}(E_i). \quad (5.3)$$

The pion content is evaluated separately in the interacting and incident histograms. Their ratio determines a correction to the measured raw cross section. For example, the measured raw cross section of a sample with enhanced muons content will tend to be lower than the raw cross section of a muon free sample. This is because most of the muons will cross the TPC without stopping, thus contributing almost exclusively to the incident histogram, forcing the pion content to be lower in the incident histogram than in the interacting; thus, the correction will tend to enhance the cross section.

2194 5.4 Estimate of Energy Loss before the TPC

2195 The beamline particles travel a path from where their momentum is measured in
2196 the beamline until they are tracked again inside the TPC. In the LArIAT geometry,
2197 a particle leaving the WC4 will encounter the materials listed in Table 5.4 before
2198 being registered again. The energy lost by the particle in this non-instrumented
2199 material modifies the particle's kinetic energy and directly affects the cross section
2200 measurement, as shown in equation 4.5.

Material	density [g/cm ³]	width [cm]
Fiberglass laminate (G10)	1.7	1.28
Liquid Argon	1.4	3.20
Stainless Steel	7.7	0.23
Titanium	4.5	0.04
Air	$1.2 \cdot 10^{-3}$	89.43
Plastic Scintillator	1.03	1.20 (+ 1.30)

Table 5.4: LArIAT material budget from WC4 to the TPC Front Face.

We derive an estimate of the energy loss between the beamline momentum measurement and the TPC (E_{loss}) from the pion and kaon DDMC samples, since this quantity is not measurable directly on data. The E_{loss} distribution for the 60A and 100A pion sample is shown in figure 5.10, left and right respectively. The E_{loss} distribution for the whole kaon sample is shown in figure 5.11. A clear double peaked structure is visible, which is due to the particles either missing or hitting the HALO paddle: a schematic rendering of this occurrence is shown in figure 5.12. The kinematic at WC4 determines the trajectory of a particle and whether or not it will hit the halo paddle. In figure 5.13 , we plot the true horizontal component of the momentum P_x versus the true X position at WC4 for pions missing the halo paddle (left) and for pions hitting the halo paddle (right) for the -60A MC simulation runs – analogous plots are obtained with the -100A pion simulation and with the kaon simulation. These distributions can be separated drawing a line in this position-momentum space.

We use a logistic regression [13] as a classifier to find the best separating line, shown in both plots as the red line. We classify as “hitting the halo paddle” all pions whose P_x and X are such that

$$P_x + 0.02 * X - 0.4 < 0$$

and as “missing the halo paddle” all pions whose P_x and X are such that

$$P_x + 0.02 * X - 0.4 > 0,$$

where the coefficients of the line are empirically found by the logistic regression estimation. Overall, this simple method classifies in the right category (hit or miss) about 86% of the pion events. In MC, we assign $E_{loss} = 32 \pm 4$ MeV for pion events classified as “hitting the halo paddle”; we assign $E_{loss} = 24 \pm 3$ MeV for pion events classified as “missing the halo paddle”. We apply the same classifier on data.

A scan of the simulated geometry showed an excess of 3 cm of uninstrumented argon compared with the surveyed detector geometry. We account for this difference by assigning in data $E_{loss} = 24 \pm 6$ MeV for pion events classified as “hitting the halo paddle” and $E_{loss} = 17 \pm 6$ MeV for pion events classified as “missing the halo paddle”, where the uncertainty is derived as the standard deviation of the double peaked distribution.

The summary of the values for used for E_{Loss} for the pion sample is listed in table 5.5 with the analogous results for the study on the kaon case.

	E_{loss} [MeV]	
	Hitting Halo	Missing Halo
Pion MC	32 ± 4	24 ± 3
Pion Data	25 ± 6	17 ± 6
Kaon MC	38 ± 6	31 ± 5
Kaon Data	26 ± 7	22 ± 7

Table 5.5: Energy loss for pions and kaons.

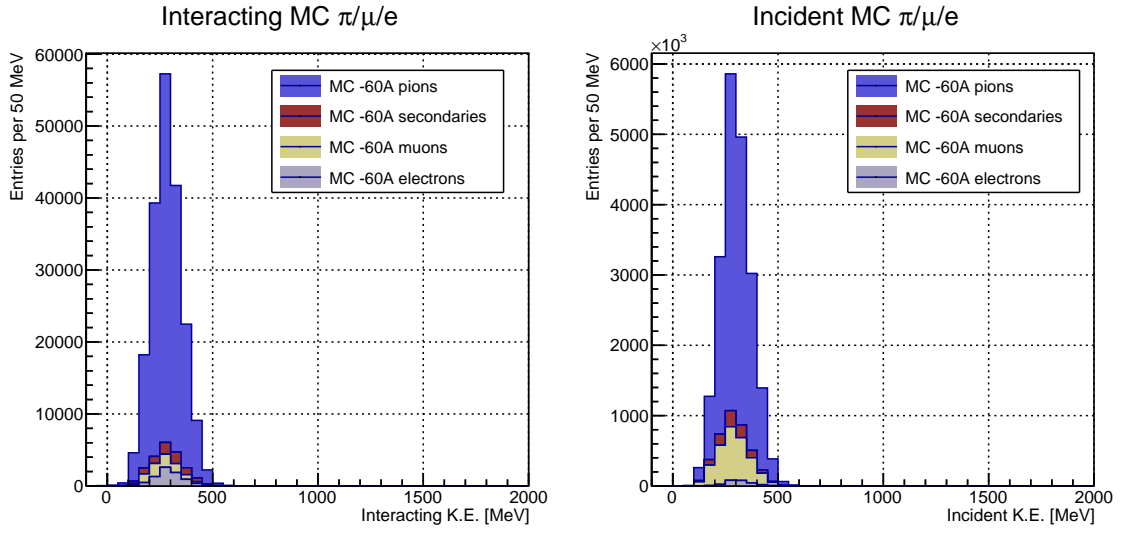


Figure 5.9: Left: staggered contributions to the interacting kinetic energy distribution for electron (grey), muons (yellow) and pion (blue) in the 60A simulation sample. Right: staggered contributions to the incident kinetic energy distribution for electron (grey), muons (yellow) and pion (blue) in the 60A simulation sample.

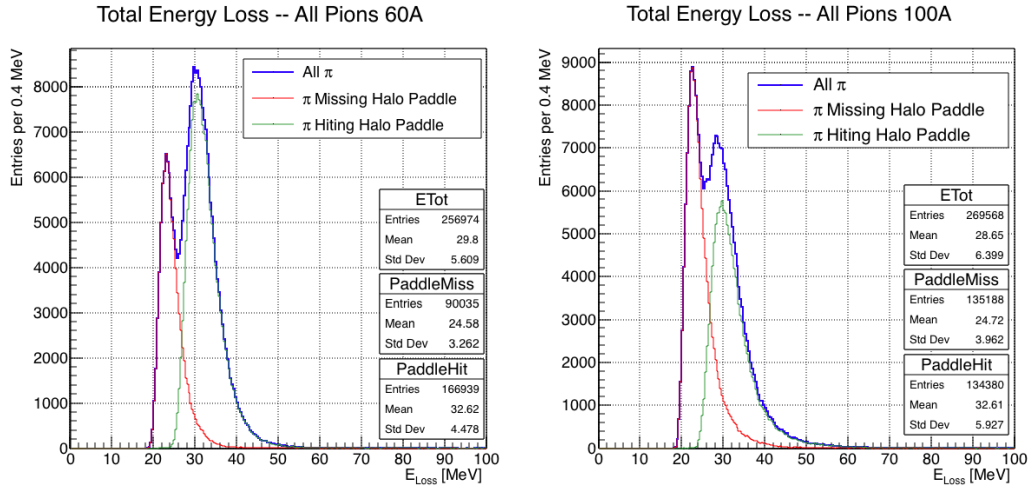


Figure 5.10: True energy loss between WC4 and the TPC front face according to the MC simulation of negative pions of the 60A runs (left) and of the 100A runs (right). The distribution for the whole data sample is shown in blue, the distribution for the pions missing the halo is shown in red, and the distribution for the pions hitting the halo is shown in green.

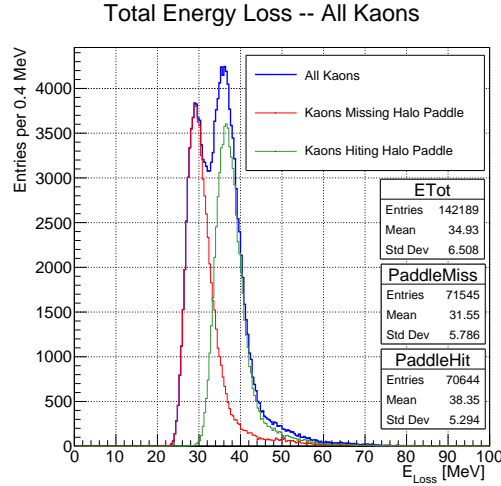


Figure 5.11: True energy loss between WC4 and the TPC front face according to the MC simulation of positive kaons in the 60A and 100A combined sample. The distribution for the whole data sample is shown in blue, the distribution for the kaons missing the halo is shown in red, and the distribution for the kaons hitting the halo is shown in green.

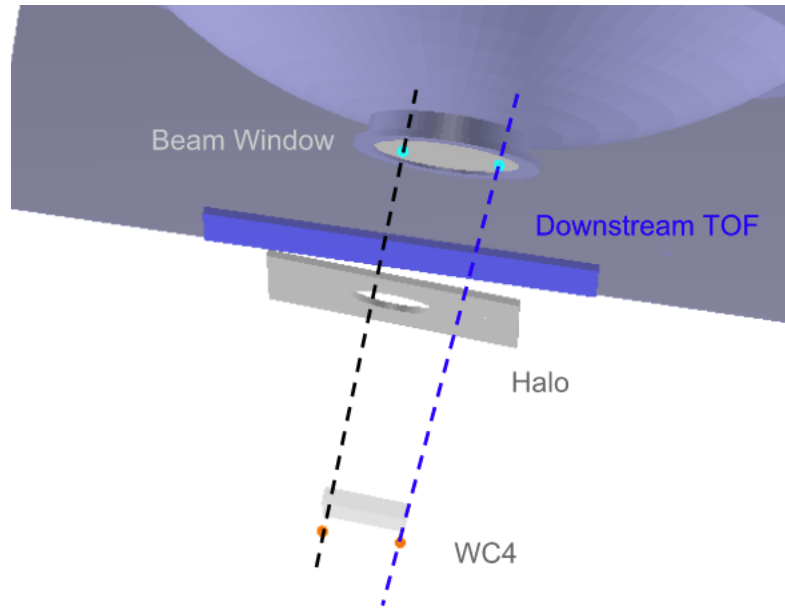


Figure 5.12: Schematic rendering of the particle path between WC4 and the TPC front face. The paddle with the hollow central circle represents the Halo paddle. We illustrate two possible trajectories: in black, a trajectory that miss the paddle and goes through the hole in the Halo, in blue a trajectory that hits the Halo paddle and goes through the scintillation material.

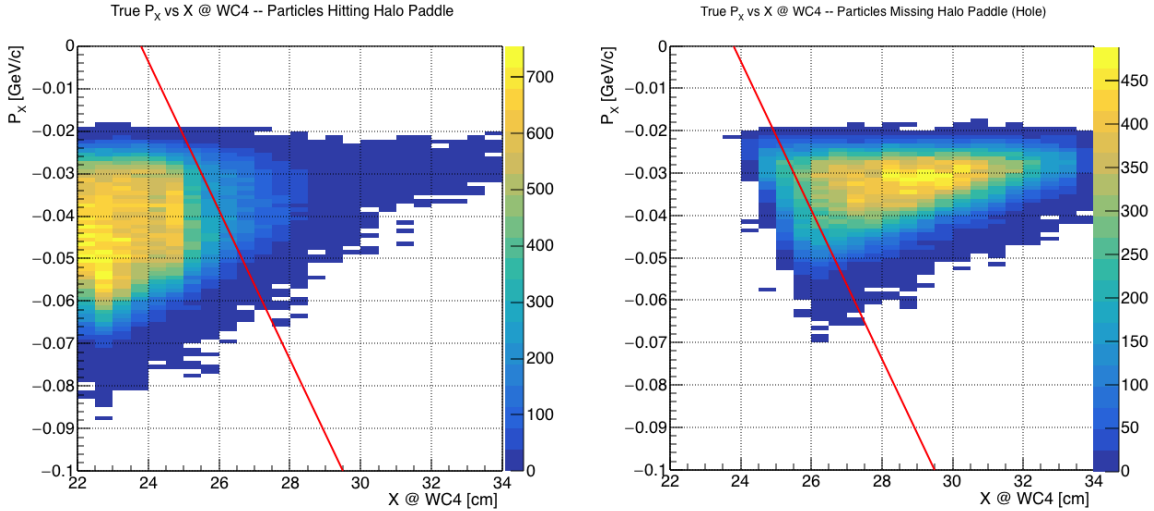


Figure 5.13: Horizontal component of the true momentum vs the horizontal position at WC4 for MC simulated pions of the 60A runs. The plot on the left shows the distribution for pion that miss the halo paddle and the plot on the right shows the distributions for pions that hit the halo. The form of the classifier is overlaid to both plots (red line).

2214 5.5 Tracking Studies

2215 The tracking of hadrons in the TPC determines both the beamline to TPC hand-
2216 shake and the identification of the interaction point within the TPC. Thus, it plays
2217 a fundamental role in the cross section measurements. We performed several studies
2218 geared towards the optimization of the package for tracking in the TPC. In particular,
2219 we studied a suitable set of parameters for the WC2TPC match and we optimized
2220 the clustering algorithm to maximize the efficiency of finding the interaction point on
2221 MC. Given the technical nature of these studies, we report them in Appendix A. We
2222 report here the evaluation of the angular resolution of the tracking algorithm in data
2223 and MC, due to its implication on the physics measurement.

2224 5.5.1 Angular Resolution

2225 Scope of this study is to understand and compare the tracking performances and
2226 angular resolution of the TPC tracking on data and MC. We use the angular resolution

2227 of the tracking to determine the value of smallest angle that we can reconstruct with
2228 a non-zero efficiency, effectively determining a selection on the angular distribution
2229 of the cross section measurement due to the tracking performance.

2230 We start by selecting all the WC2TPC matched tracks used for the cross section
2231 analysis. These tracks can contain from a minimum of 3 3D-space points to a maxi-
2232 mum of 240 3D-space points. We fit a line to all the 3D-space points associated with
2233 the track. For each track we calculate the average distance between each point in
2234 space and the fit line as follows

$$\bar{d} = \frac{\sum_i^N d_i}{N}, \quad (5.4)$$

2235 where N is the number of 3D-space points of the track and d_i is the distance of the
2236 i -th space point to the line fit. Several tests to compare the goodness of fit between
2237 data and MC have been considered. We decided to use \bar{d} for its straightforward
2238 interpretation. The \bar{d} distribution for data and MC is shown in Figure 5.16 for pions
2239 and in Figure 5.18 for kaons and shows a relatively good agreement between data and
2240 MC.

2241 A visual representation of the procedure used to evaluate the angular resolution
2242 is shown in Figure 5.14. For each track, we order the space points according to their
2243 Z position along the positive beam direction (panel a) and we split them in two sets:
2244 the first set contains all the points belonging to the first half of the track and the
2245 second set contains all the points belonging the second half of the track. We remove
2246 the last four points in the first set and the first four points in the second set, so to
2247 have a gap in the middle of the original track (panel b). We fit the first and the second
2248 set of points with two lines (panel c). We then calculate the angle between the fit of
2249 the first and second half α (panel d). The angle α determines the spatial resolution
2250 of the tracking. The distributions for data and MC for α are given in Figure 5.17 for
2251 pions and in Figure 5.19 for kaons. The mean of the data and MC angular resolution
2252 are reported in Table tab:AngRes for pions and kaons in data and MC.

2253 Interaction angles smaller than the angle resolution are indistinguishable for the
 2254 reconstruction. Therefore, we assess our ability to measure the cross section to be
 2255 limited to interaction angles greater than 5.0 deg. More accurate studies of the angular
 2256 resolution as a function of the kinetic energy and track length, albeit interesting, are
 2257 left for an improvement of the analysis.

2258 It is beneficial to take a moment to describe the definition of interaction angle.
 2259 In case of elastic scattering, the definition is straightforward: the interaction angle is
 2260 the angle between the incoming and outgoing hadron, i.e.

$$\theta = \cos^{-1} \left(\frac{\vec{p}_{\text{incoming}} \cdot \vec{p}_{\text{outgoing}}}{|\vec{p}_{\text{incoming}}| |\vec{p}_{\text{outgoing}}|} \right). \quad (5.5)$$

2261 In case of inelastic scattering, the presence of several topologies requires a more
 2262 complex definition, as shown in figure 5.15. We define the scattering angle as the
 2263 biggest of the angles between the incoming hadron and the visible daughters, where
 2264 the visible daughters are charged particles that travel more than 0.47 cm in the
 2265 detector (see panel a); in case all the daughters are invisible, the angle is assigned
 2266 to be 90 deg (see panel b). We chose this working definition of scattering angle
 2267 for inelastic scattering keeping in mind how our tracking reconstruction works: the
 2268 tracking will stop correctly if none of the daughters are visible in the detector and it
 2269 is likely to stop correctly if multiple daughters form an interaction vertex. The only
 2270 “dangerous” case is the production of one charged daughter plus neutrals, which we
 2271 can study with this working definition of scattering angle (see panel c).

2272 We can see the effects of the angular resolution on the cross section by plotting the
 2273 true Geant4 cross section for interaction angles greater than a minimum interaction

	Data	MC
Pions	$\bar{\alpha}_{Data} = (5.0 \pm 4.5) \text{ deg}$	$\bar{\alpha}_{MC} = (4.5 \pm 3.9) \text{ deg}$
Kaons	$\bar{\alpha}_{Data} = (4.3 \pm 3.7) \text{ deg}$	$\bar{\alpha}_{MC} = (4.4 \pm 3.6) \text{ deg}$

Table 5.6: Angular resolution for Pion and Kaon tracking in both data and MC.

angle. Figure 5.20 shows the true Geant4 cross section for interaction angles greater than 0 deg (green), 4.5 deg (red), 5.0 deg (blue) and 9.0 deg (yellow). A small 0.5 deg systematic shift between the mean of the data and MC angular resolution is present.

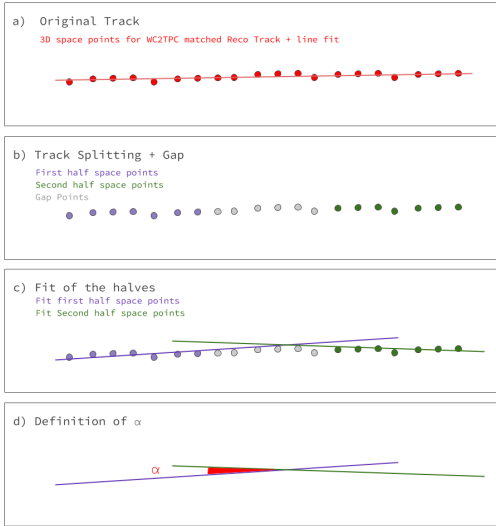


Figure 5.14: A visual representation of the procedure used to evaluate the angular resolution.

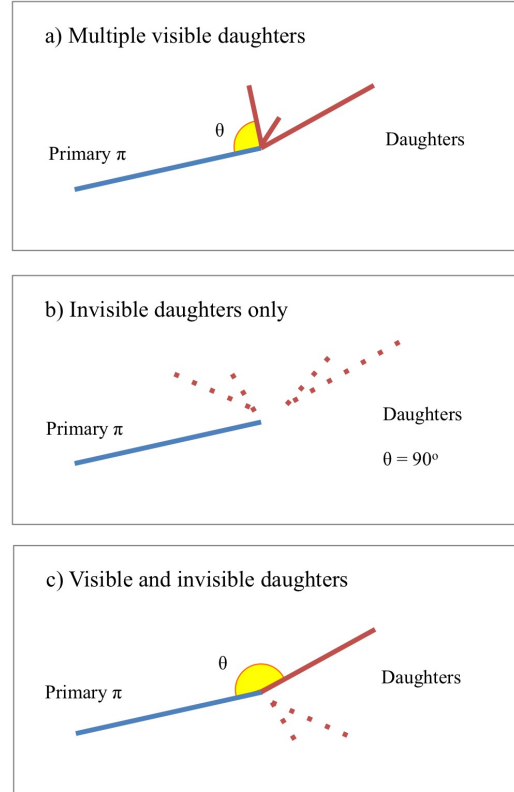


Figure 5.15: A visual representation of the scattering angle definition in case of inelastic scattering.

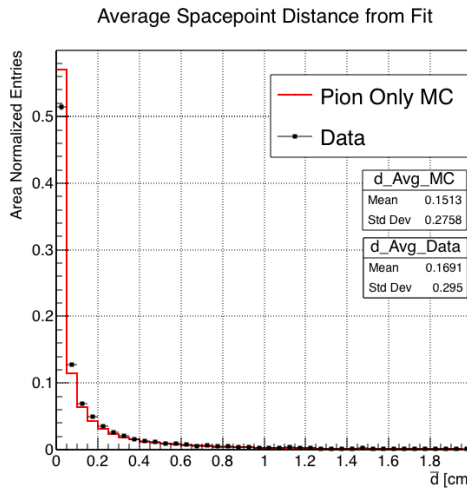


Figure 5.16: Distributions of the average distance between each 3D point in space and the fit line, \bar{d} for the data used in the pion cross section analysis and the pion only DDMC. The distributions are area normalized.

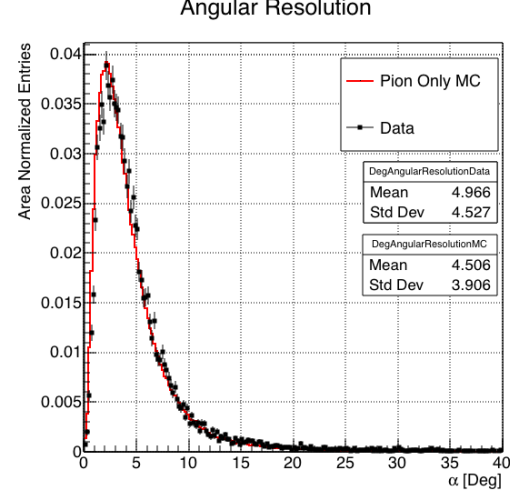


Figure 5.17: Distributions of angular resolution α for data used in the pion cross section analysis and pion only DDMC. The distributions are area normalized.

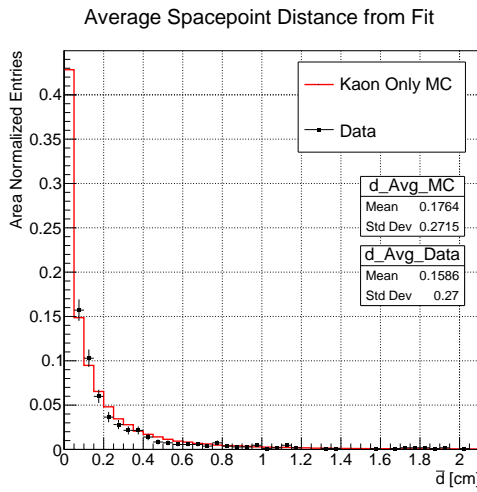


Figure 5.18: Distributions of the average distance between each 3D point in space and the fit line, \bar{d} for the data used in the kaon cross section analysis and the kaon only DDMC. The distributions are area normalized.

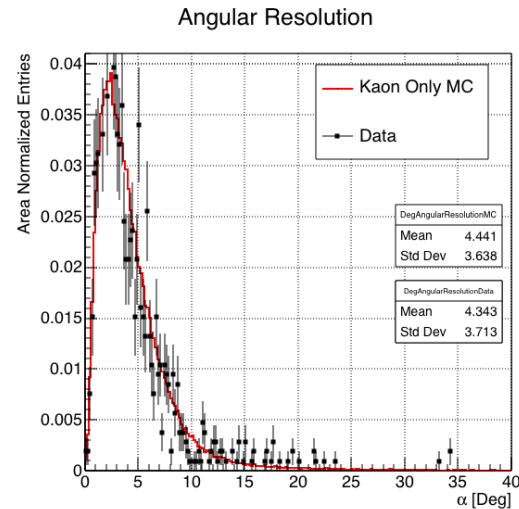


Figure 5.19: Distributions of angular resolution α for data used in the kaon cross section analysis and kaon only DDMC. The distributions are area normalized.

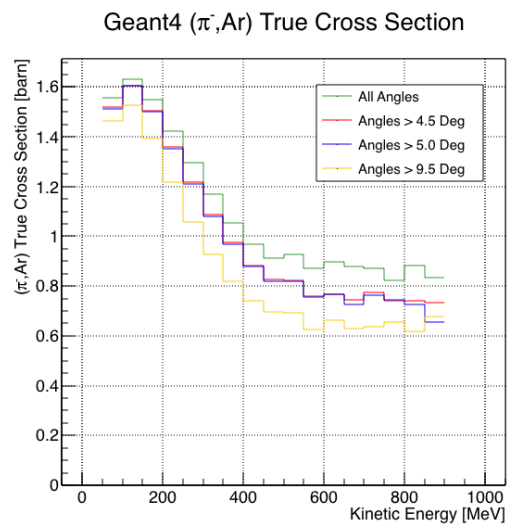


Figure 5.20: True (π^- , Ar) cross section for interaction angles greater than 0 deg (green), 4.5 deg (red), 5.0 deg (blue) and 9.0 deg (yellow).

2277 5.6 Calorimetry Studies

2278 The measured kinetic energy of a hadron candidate at each argon slab determines
2279 which bins of the interacting and incident histograms a selected event is going to fill.
2280 Thus, the energy measurement provided by the LArTPC is fundamental for the cross
2281 section analysis. In Appendix B, we describe how we calibrate the TPC calorimetric
2282 response. In the following section, we describe how we measure the kinetic energy of
2283 the hadrons in the TPC.

2284 5.6.1 Kinetic Energy Measurement

2285 In this section, we define the measurement on the kinetic energy and determine the
2286 related uncertainty. We will propagate this uncertainty into the cross section mea-
2287 surement, as discussed in Section 6.1.2 for the pion cross section and in Section ??
2288 for the kaon cross section.

2289 The kinetic energy of a hadron at the j^{th} slice of argon in the TPC is given by

$$KE_j = \sqrt{p_{\text{Beam}}^2 + m_{\text{Beam}}^2} - m_{\text{Beam}} - E_{\text{Loss}} - E_{\text{FF-j}}, \quad (5.6)$$

2290 where p_{Beam} is the momentum measured by the beamline detectors, m_{Beam} is the
2291 mass of the hadron as reported in the PDG, E_{Loss} is the energy loss between the
2292 beamline and the TPC, and $E_{\text{FF-j}}$ is the energy that the hadron deposited from the
2293 TPC front face until the j^{th} slice. The uncertainty on KE_j is then given by

$$\delta KE_j = \sqrt{\delta p_{\text{Beam}}^2 + \delta E_{\text{Loss}}^2 + \delta E_{\text{dep FF-j}}^2}, \quad (5.7)$$

2294 where we have dropped the uncertainty on the mass, since it is orders of magnitude
2295 smaller than the other uncertainties. We assume the relative uncertainty on p_{Beam} to
2296 be 2%, and the uncertainty on the energy loss upstream to be 7 MeV, as calculated

2297 in Section 5.4. We describe the estimate of the uncertainty on $E_{\text{FF},j}$ in the rest of
2298 this section.

2299 The energy deposited by the hadron from the TPC front face until the j^{th} slice is
2300 the sum of the measured energy deposited in each previous slabs E_i , i.e.

$$E_{\text{FF},j} = \sum_{i < j} E_i, \quad (5.8)$$

2301 where E_i is measured in each slab as the product of the stopping power, dE/dX_i ,
2302 and the track pitch, Pitch_i , for that point. If we assume conservatively that the
2303 measurements of E_i are not independent from one another, the uncertainty on $E_{\text{FF},j}$
2304 becomes

$$\delta E_{\text{FF},j} = (j - 1)\delta E_i, \quad (5.9)$$

2305 where δE_i is the uncertainty on the energy loss in one slab of argon.

2306 The left side of Figure 5.21 shows the distribution of the energy deposited in each
2307 slab of argon, for the 60A negative pion dataset in black and for the pion only MC
2308 in blue. The analogous plot for the -100A negative pion data set is show on the right
2309 side of Figure 5.21. The distributions are fitted with a landau displayed in red for
2310 data and in teal for MC. The uncertainty on E_i is given by the width of the Landau
2311 fit to the data. A small systematic uncertainty is given by a 1.0% difference between
2312 the most probable value of the landau fits in data and MC.

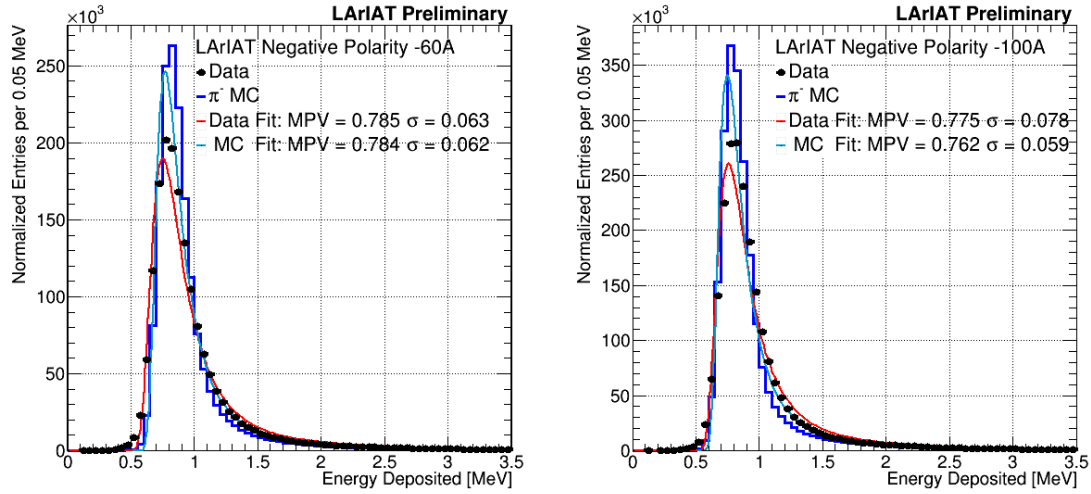


Figure 5.21: Energy deposited E_i in a single slab of argon for the pion -60A runs (left) and -100A runs (right). The data is shown in black, the MC in blue. The distributions are fitted with a landau displayed in red for data and in teal for MC.

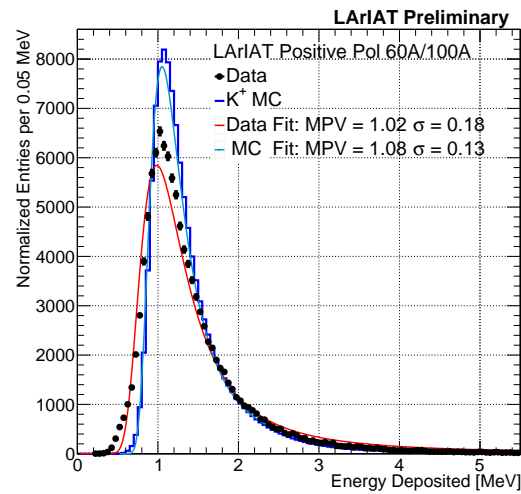


Figure 5.22: Energy deposited E_i in a single slab of argon for the kaons of the +60A runs and +100A runs. The data is shown in black, the MC in blue. The distributions are fitted with a landau displayed in red for data and in teal for MC.

2313 **Chapter 6**

2314 **Negative Pion Cross Section**

2315 **Measurement**

2316 “*Y ella es flama que se eleva, Y es un pájaro a volar.*

2317 *En la noche que se incendia, estrella de oscuridad*
2318 *que busca entre la tiniebla, la dulce hoguera del beso.”*

2319 – Lila Downs, 2002 –

2320 In this chapter, we show the result of the thin slice method to measure the (π^- -
2321 Ar) total hadronic cross section. In Section 6.1, we start by measuring the raw
2322 cross section, i.e. the cross section obtained exclusively using data reconstruction,
2323 without any additional corrections. In Section 6.2, we apply a statistical subtraction
2324 of the background contributions based on simulation and a correction for detection
2325 inefficiency. The final results are presented in Section 6.3.

2326 **6.1 Raw Cross Section**

2327 We measure the raw (π^- -Ar) total hadronic cross section as a function of the kinetic
2328 energy in the two chosen data sets, the -60A and -100A negative runs. As we will

clarify in Section 6.2, the corrections to the raw cross section depend on the beam conditions and need to be calculated independently for the two datasets. Thus, we present here the measurement of the raw cross section on the two datasets separately.

As stated in section 4.3.2, the raw cross section is given by the equation 4.4

$$\sigma_{TOT}(E_i) = \frac{1}{n\delta X} \frac{N_{Int}^{TOT}(E_i)}{N_{Inc}^{TOT}(E_i)}, \quad (6.1)$$

where N_{Int}^{TOT} is the measured number of particles interacting at kinetic energy E_i , N_{Inc}^{TOT} is the measured number of particles incident on an argon slice at kinetic energy E_i , n is the density of the target centers and δX is the thickness of the argon slice. The density of the target centers and the slab thickness are $n = 0.021 \cdot 10^{24} \text{ cm}^{-3}$ and $\delta X = 0.47 \text{ cm}$, respectively.

Figure 6.1 shows the distribution of N_{Int}^{TOT} as a function of the kinetic energy for the 60A dataset on the left and for the 100A dataset on the right. The data central points are represented by black dots, the statistical uncertainty is shown in black, while the systematic uncertainty is shown in red. Data is displayed over the N_{Int}^{TOT} distribution obtained with a MC mixed sample of pions, muon and electrons (additional details on the composition will be provided in Section ??). The contribution from the simulated pions is shown in blue, the one from secondaries in red, the one from muons in yellow and the ones from electrons in gray. The simulated pion's and backgrounds' contributions are stacked; the sum of the integrals from each particle species is normalized to the integral of the data.

Figure 6.2 shows the distribution of N_{Inc}^{TOT} for the 60A dataset on the left and for the 100A dataset on the right. Data is displayed over the MC. The same color scheme and normalization procedure is used for both the interacting and incident histograms.

Figure 6.3 shows the raw cross section for the 60A dataset on the left and for the 100A dataset on the right, statistical uncertainty in black and systematic uncertainty

2353 in red. The raw data cross section is overlaid to the reconstructed cross section for
 2354 the MC mixed sample, displayed in azure. Since the background contributions and
 2355 the detector effects for the 60A and 100A sample are different, it is premature to
 2356 compare the raw cross sections obtained from the two samples at this point.

2357 We describe the calculation of the statistical uncertainty for the interacting, in-
 2358 cident and cross section distributions in Section 6.1.1; we describe the procedure to
 2359 calculate the corresponding systematics uncertainty on Section 6.1.2.

2360 6.1.1 Statistical Uncertainty

2361 The statistical uncertainty for a given kinetic energy bin of the cross section is cal-
 2362 culated by error propagation from the statistical uncertainty on $N_{\text{Inc}}^{\text{TOT}}$ and $N_{\text{Int}}^{\text{TOT}}$
 2363 correspondent bin. Since the number of incident particles in each energy bin is given
 2364 by a simple counting, we assume that $N_{\text{Inc}}^{\text{TOT}}$ is distributed as a poissonian with mean
 2365 and variance equal to $N_{\text{Inc}}^{\text{TOT}}$ in each bin. On the other hand, $N_{\text{Int}}^{\text{TOT}}$ follows a bino-
 2366 mial distribution: a particle in a given energy bin might or might not interact. The
 2367 variance for the binomial is given by

$$\text{Var}[N_{\text{Int}}^{\text{TOT}}] = \mathcal{N}P_{\text{Interacting}}(1 - P_{\text{Interacting}}). \quad (6.2)$$

2368 Since the interaction probability $P_{\text{Interacting}}$ is $\frac{N_{\text{Int}}^{\text{TOT}}}{N_{\text{Inc}}^{\text{TOT}}}$ and the number of tries \mathcal{N} is
 2369 $N_{\text{Inc}}^{\text{TOT}}$, equation 6.2 translates into

$$\text{Var}[N_{\text{Int}}^{\text{TOT}}] = N_{\text{Inc}}^{\text{TOT}} \frac{N_{\text{Int}}^{\text{TOT}}}{N_{\text{Inc}}^{\text{TOT}}} \left(1 - \frac{N_{\text{Int}}^{\text{TOT}}}{N_{\text{Inc}}^{\text{TOT}}}\right) = N_{\text{Int}}^{\text{TOT}} \left(1 - \frac{N_{\text{Int}}^{\text{TOT}}}{N_{\text{Inc}}^{\text{TOT}}}\right). \quad (6.3)$$

2370 $N_{\text{Inc}}^{\text{TOT}}$ and $N_{\text{Int}}^{\text{TOT}}$ are not independent. The statistical uncertainty on the cross
 2371 section is thus calculated as

$$\delta\sigma_{\text{TOT}}(E) = \sigma_{\text{TOT}}(E) \left(\frac{\delta N_{\text{Int}}^{\text{TOT}}}{N_{\text{Int}}^{\text{TOT}}} + \frac{\delta N_{\text{Inc}}^{\text{TOT}}}{N_{\text{Inc}}^{\text{TOT}}} \right) \quad (6.4)$$

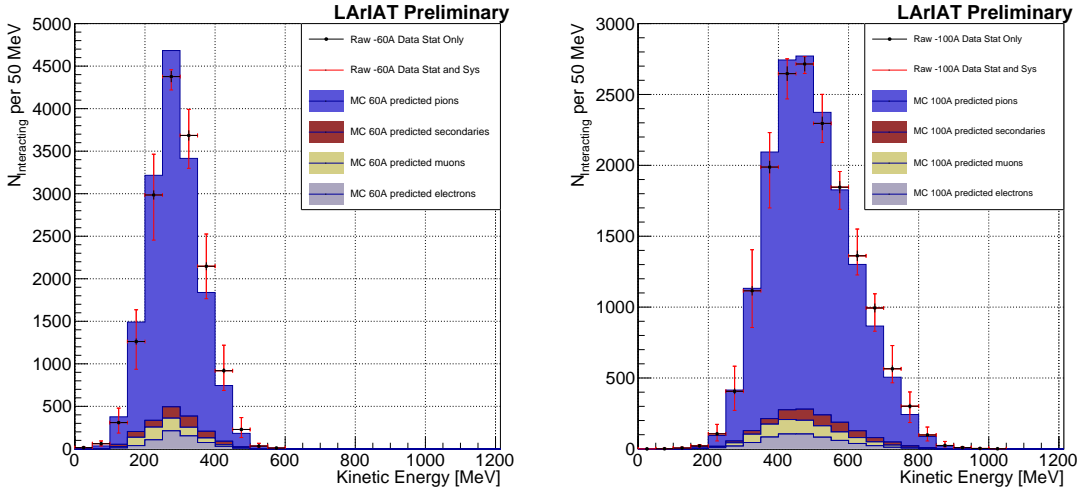


Figure 6.1: Raw number of interacting pion candidates as a function of the reconstructed kinetic energy for the 60A runs (left) and for the 100A runs (right). The statistical uncertainties are shown in black, the systematic uncertainties in red.

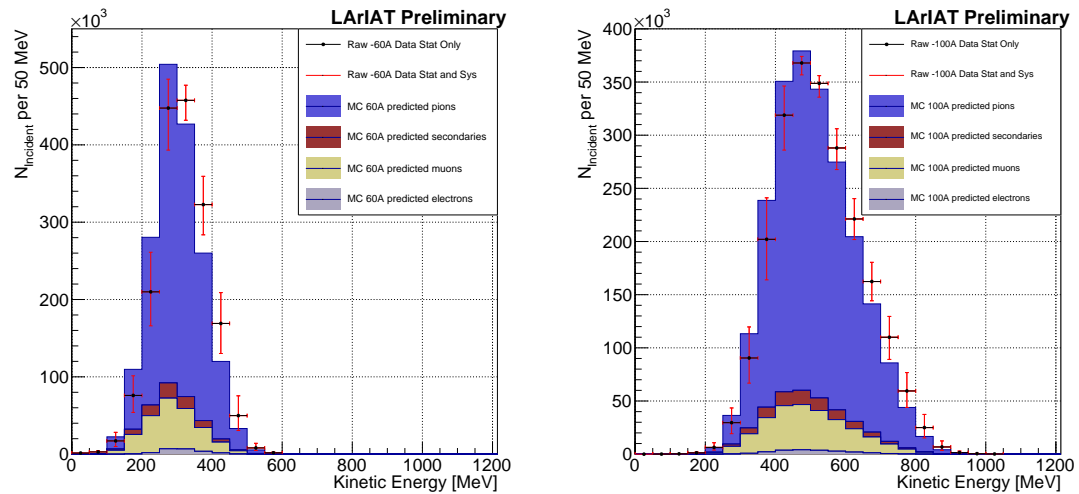


Figure 6.2: Raw number of incident pion candidates as a function of the reconstructed kinetic energy for the 60A runs (left) and for the 100A runs (right). The statistical uncertainty is shown in black, the systematic uncertainties in red.

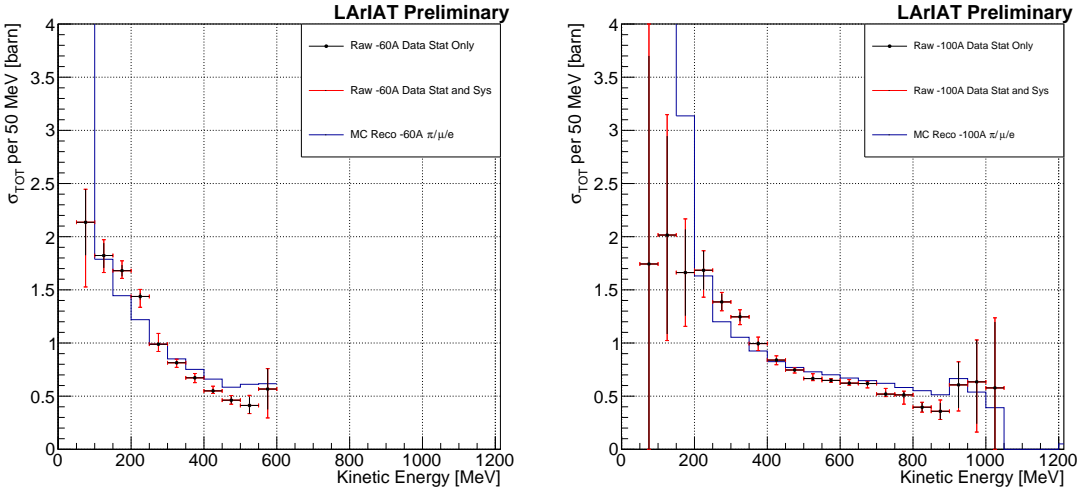


Figure 6.3: Raw (π^- -Ar) total hadronic cross section for the 60A runs (left) and for the 100A runs (right). The statistical uncertainty is shown in black, the systematic uncertainties in red. The raw cross section obtained with a MC mixed sample of pions, muon and electrons in the percentage predicted by G4Beamline is shown in azure.

2372 where:

$$\delta N_{\text{Inc}}^{\text{TOT}} = \sqrt{N_{\text{Inc}}^{\text{TOT}}} \quad (6.5)$$

$$\delta N_{\text{Int}}^{\text{TOT}} = \sqrt{N_{\text{Int}}^{\text{TOT}} \left(1 - \frac{N_{\text{Int}}^{\text{TOT}}}{N_{\text{Inc}}^{\text{TOT}}}\right)}. \quad (6.6)$$

2373 6.1.2 Treatment of Systematics

2374 The only systematic effect considered in the measurement of the raw cross section
 2375 results from the propagation of the uncertainty associate with the measurement of
 2376 the kinetic energy at each argon slab. As shown in Section 5.6.1, the uncertainty on
 2377 the kinetic energy of a pion candidate at the j^{th} slab of argon is given by

$$\delta KE_j = \sqrt{\delta p_{\text{Beam}}^2 + \delta E_{\text{Loss}}^2 + \delta E_{\text{dep FF-j}}^2} \quad (6.7)$$

$$= \sqrt{(2\% p_{\text{Beam}})^2 + (6 \text{ [MeV]})^2 + (j - 1)^2 (\sim 0.08 \text{ [MeV]})^2}. \quad (6.8)$$

2378 We propagate this uncertainty by varying the energy measurement KE_j at each
 2379 argon slab. We measure $N_{\text{Inc}}^{\text{TOT}}$, $N_{\text{Int}}^{\text{TOT}}$ and the cross section in three cases: first
 2380 assigning the measured KE_j at each kinetic energy sampling, then assigning $KE_j +$
 2381 δKE_j , and finally assigning $KE_j - \delta KE_j$. The difference between the values obtained
 2382 using the KE_j sampling and the maximum and minimum values in each kinetic energy
 2383 bin determines the systematic uncertainty.

2384 **6.2 Corrections to the Raw Cross Section**

2385 As described in section 4.3.3, we need to apply a background correction and an
 2386 efficiency correction in order to derive the true pion cross section from the raw cross
 2387 section. The true cross section is given in equation 4.9,

$$\sigma_{\text{TOT}}^{\pi^-}(E_i) = \frac{1}{n\delta X} \frac{\epsilon^{\text{Inc}}(E_i)}{\epsilon^{\text{Int}}(E_i)} \frac{C_{\text{Int}}^{\pi MC}(E_i)}{C_{\text{Inc}}^{\pi MC}(E_i)} \frac{N_{\text{Int}}^{\text{TOT}}(E_i)}{N_{\text{Inc}}^{\text{TOT}}(E_i)}. \quad (4.9)$$

2388 Section 6.2.1 describes the evaluation of pion content in the interacting and inci-
 2389 dent histograms, ($C_{\text{Int}}^{\pi MC}(E_i)$ and $C_{\text{Inc}}^{\pi MC}(E_i)$) and the propagation to the cross section
 2390 measurement of the relative systematic uncertainties.

2391 Section 6.2.2 describes the procedure employed to obtain the efficiency corrections
 2392 $\epsilon^{\text{Int}}(E_i)$ and $\epsilon^{\text{Inc}}(E_i)$ and the propagation to the cross section measurement of the
 2393 relative uncertainties.

2394 **6.2.1 Background subtraction**

2395 We use the procedure described in 5.3.2 to evaluate the relative pion content in
 2396 the interacting histogram $C_{\text{Int}}^{\pi MC}(E_i)$ and the relative pion content in the incident
 2397 $C_{\text{Inc}}^{\pi MC}(E_i)$. We start by evaluating the relative pion content assuming the beamline
 2398 composition simulated by G4Beamline, whose pion, muon and electron percentages
 2399 per beam condition are reported again in the first line of Table 6.1. The left side of

2400 Figure 6.4 shows the MC estimated relative pion content for the interacting histogram
2401 as function of kinetic energy for the 60A runs (top) and 100A runs (bottom). The
2402 right side of the same figure shows the MC estimated relative pion content for the
2403 incident histogram as function of kinetic energy for the 60A runs (top) and 100A
2404 runs (bottom). In Figure 6.4 the central curves displayed in light blue are obtained
2405 using the beamline composition as predicted by G4Beamline: these are the correction
2406 curves for the relative pion content applied to data.

2407 So, the question now becomes: how well do we know the beamline composition?
2408 In absence of additional data constraints, we take a 100% systematic uncertainty on
2409 the electron content, reported in lines 3 and 4 of Table 6.1. The effect of doubling or
2410 halving the electron percentage in the beam on the pion relative content is displayed
2411 in red in Figure 6.4. We reserve a slightly different treatment for the muon content.
2412 Since G4Beamline tracks only particles which cross all the wire chambers, pion events
2413 that decay in flight from WC1 to WC4 are not recorded by G4Beamline. Pion decays
2414 in the beamline could be trigger the beamline detectors in data, if the produced muon
2415 proceeds in the beamline. Thus, we take the G4Beamline prediction for muons as a
2416 lower bound in the composition: the effect of doubling the muon content (line 2 in
2417 Table 6.1) is shown in blue on Figure 6.4. A future study of data from additional
2418 beamline detectors such as the Aerogel Chernkov detectors [43] or the muon range
2419 stack (see Section 3.2.4) has the potential of a narrowing the systematics uncertainty
2420 coming from the beamline composition.

2421 We propagate the uncertainty on the beamline composition as a systematic un-
2422 certainty to the cross section by varying the beam composition for all the cases listed
2423 in Table 6.1 and evaluating variation of obtained data cross sections in each bin. This
2424 systematic uncertainty is summed in quadrature with the statistical uncertainty and
2425 the systematic uncertainty related to the kinetic energy measurement.

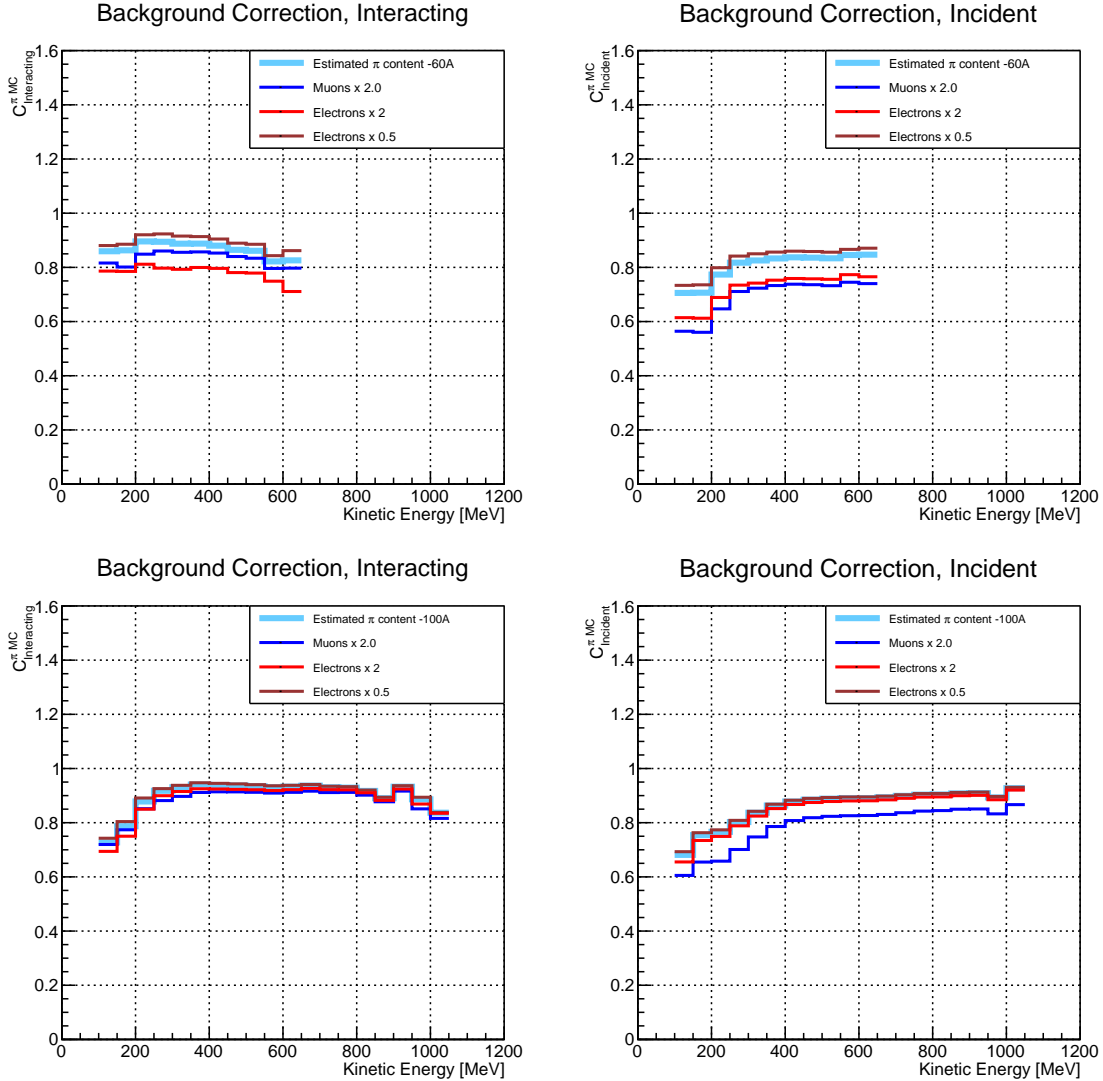


Figure 6.4: *Left:* MC estimated relative pion content for interacting histogram a function of kinetic energy for the 60A runs (top) and 100A runs (bottom), predicted background content in azure and muon and electron content variation in blue and red. *Right:* MC estimated relative pion content for incident histogram a function of kinetic energy for the 60A runs (top) and 100A (bottom), predicted background content in azure and muon and electron content variation in blue and red

2426 6.2.2 Efficiency Correction

2427 The interaction point for a track used in the total hadronic cross section analysis
2428 is defined to be the last point of the WC2TPC matched track which lies inside the
2429 fiducial volume. This definition is independent from the topology of the interaction.
2430 If the TPC track stops within the fiducial volume, its last point will be the interaction
2431 point, no matter what the products of the interaction look like; if the track crosses the
2432 boundaries of the fiducial volume, the track will be considered “through going” and no
2433 interaction point will be found. Given this definition, it is evident that we rely on the
2434 tracking algorithm to discern where the interaction occurred in the TPC and correctly
2435 stop the tracking. The tracking algorithm has an intrinsic angle resolution as shown
2436 in section 5.5.1, which limits its efficiency, especially in the case of elastic scattering
2437 occurring at low angles. Thus, we need to apply an efficiency correction to data in order
2438 to retrieve the true cross section. The efficiency correction is evaluated separately for
2439 the interacting and incident histograms, namely ϵ_i^{int} and ϵ_i^{inc} , and propagated to the
2440 cross section as shown in equation 4.9.

2441 Efficiency Correction: Procedure

2442 We describe here the procedure to calculate the efficiency correction taking the in-
2443 teracting histogram as example and noting that the procedure is identical for the
2444 incident histogram.

2445 We derive the correction on a set of pure pion MC, calculating its value bin by
2446 bin as the ratio between the true bin content and the correspondent reconstructed
2447 bin content. The correction is then applied to the relevant bin in data. In formulae,
2448 the efficiency correction is calculated to be

$$\epsilon^{\text{Int}}(E_i) = \frac{N_{\text{Interacting}}^{\pi \text{ Reco MC}}(E_i)}{N_{\text{Interacting}}^{\pi \text{ True MC}}(E_i)}, \quad (6.9)$$

2449 where $N_{\text{Int}}^{\pi \text{ True MC}}(E_i)$ is the content of the i -th bin in for the true interacting
 2450 histogram, and $N_{\text{Int}}^{\pi \text{ Reco MC}}(E_i)$ is the content of the i -th bin in for the reconstructed
 2451 interacting histogram. The correction is applied to data as follows

$$N_{\text{Int}}^{\pi \text{ True Data}}(E_i) = \frac{N_{\text{Int}}^{\pi \text{ Reco Data}}(E_i)}{\epsilon^{\text{Int}}(E_i)} = N_{\text{Int}}^{\pi \text{ Reco Data}}(E_i) \frac{N_{\text{Int}}^{\pi \text{ True MC}}(E_i)}{N_{\text{Int}}^{\pi \text{ Reco MC}}(E_i)}. \quad (6.10)$$

2452 where $N_{\text{Int}}^{\pi \text{ Reco Data}}(E_i)$ is the background subtracted bin content of the i -th bin in
 2453 for the reconstructed interacting histogram for data, i.e.

$$N_{\text{Int}}^{\pi \text{ Reco Data}}(E_i) = N_{\text{Int}}^{\text{TOT Data}}(E_i) - B_{\text{Int}}^{\text{Data}}(E_i) = C_{\text{Int}}^{\pi \text{ MC}}(E_i) N_{\text{Int}}^{\text{TOT Data}}(E_i). \quad (6.11)$$

2454 In section 5.5.1, we estimated the angular resolution for data and MC to be
 2455 $\bar{\alpha}_{\text{Data}} = (5.0 \pm 4.5)$ deg and $\bar{\alpha}_{\text{MC}} = (4.5 \pm 3.9)$ deg, respectively. Most interaction
 2456 angles smaller than the angular resolution will thus be indistinguishable for the re-
 2457 construction. Thus, we claim we are able to measure the cross section for interaction
 2458 angles greater than 5.0 deg. Geant4 simulates interactions at all angles, as shown in
 2459 figure 6.7. In order to calculate the efficiency correction, we select events which have
 2460 an interaction angle greater than a given α_{res} to construct the true interacting and
 2461 incident histograms (the denominator of the efficiency correction). The systematics
 2462 on the efficiency correction is estimated by varying the value of α_{res} between 0 deg
 2463 and 4.5 deg and propagating the uncertainty on the cross section.

2464 Figure 6.5 shows $\epsilon^{\text{Int}}(E_i)$ in the left side and $\epsilon^{\text{Inc}}(E_i)$ on the right as a function of
 2465 the kinetic energy for the 60A runs and their systematic uncertainty. Similarly, figure
 2466 6.6 shows $\epsilon^{\text{Int}}(E_i)$ in the left side and $\epsilon^{\text{Inc}}(E_i)$ on the right as a function of the kinetic
 2467 energy for the 100A runs and their systematic uncertainty.

	Magnet Current -60A			Magnet Current -100 A		
	MC π^-	MC μ^-	MC e^-	MC π^-	MC μ^-	MC e^-
Expected Composition	68.8 %	4.6 %	26.6 %	87.4 %	3.7 %	8.9 %
Composition 2x Muons	64.2 %	9.2 %	26.6 %	83.7 %	7.4 %	8.9 %
Composition 2x Electrons	42.2 %	4.6 %	53.2 %	78.5 %	3.7 %	17.8 %
Composition 0.5x Electrons	82.1 %	4.6 %	13.3 %	91.9 %	3.7 %	4.4 %

Table 6.1: Beam composition variation for the study of systematics due to beam contamination.

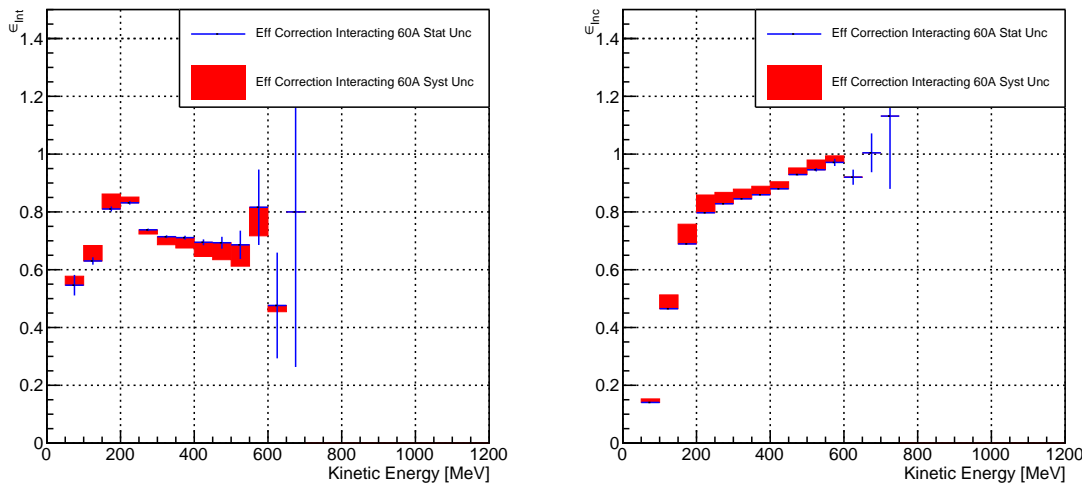


Figure 6.5: *Left:* Efficiency correction on the 60A interacting histogram, statistical uncertainty in blue, systematic uncertainty in red. *Right:* Efficiency correction on the 60A incident histogram, statistical uncertainty in blue, systematic uncertainty in red.

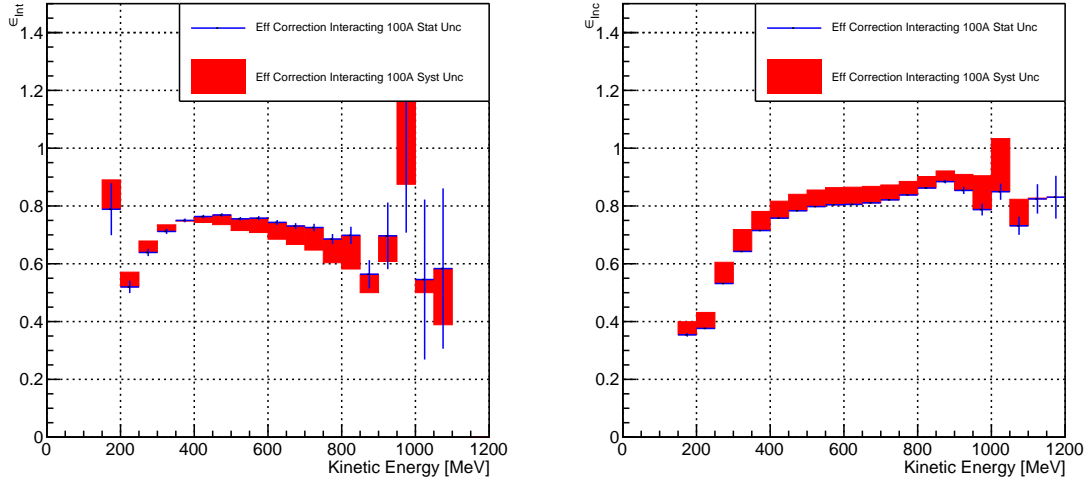


Figure 6.6: *Left*: Efficiency correction on the 100A interacting histogram, statistical uncertainty in blue, systematic uncertainty in red. *Right*: Efficiency correction on the 100A incident histogram, statistical uncertainty in blue, systematic uncertainty in red.

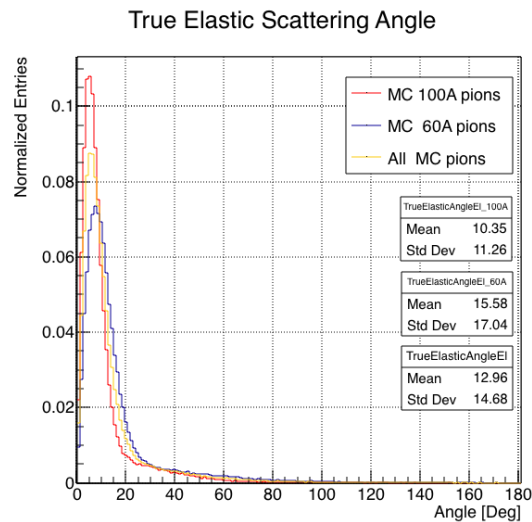


Figure 6.7: Distribution of the true scattering angle for a pion elastic scattering off the argon nucleus as simulated by Geant4.

2468 6.3 Results

2469 Figure 6.8 show the measurement of the (π^- -Ar) total hadronic cross section for
2470 scattering angles greater than 5° , as the result of the background subtraction and
2471 efficiency correction to the raw cross section. The top left plot is the measurement
2472 obtained on the 60A data, statistical uncertainty in black and systematic uncertainty
2473 in red. The top right plot is the measurement obtained on the 100A data, statistical
2474 uncertainty in black and systematic uncertainty in blue. The bottom plot shows the
2475 two measurements overlaid. In all three plot, the Geant4 prediction for the total
2476 hadronic cross section for angle scattering greater than 5° is displayed in green.

2477 The systematic uncertainty on the cross section is the sum in quadrature of the
2478 statistical uncertainty, the systematic uncertainty related to the kinetic energy mea-
2479 surement, the systematic uncertainty related to the beam composition and the sys-
2480 tematic uncertainty related to the efficiency correction.

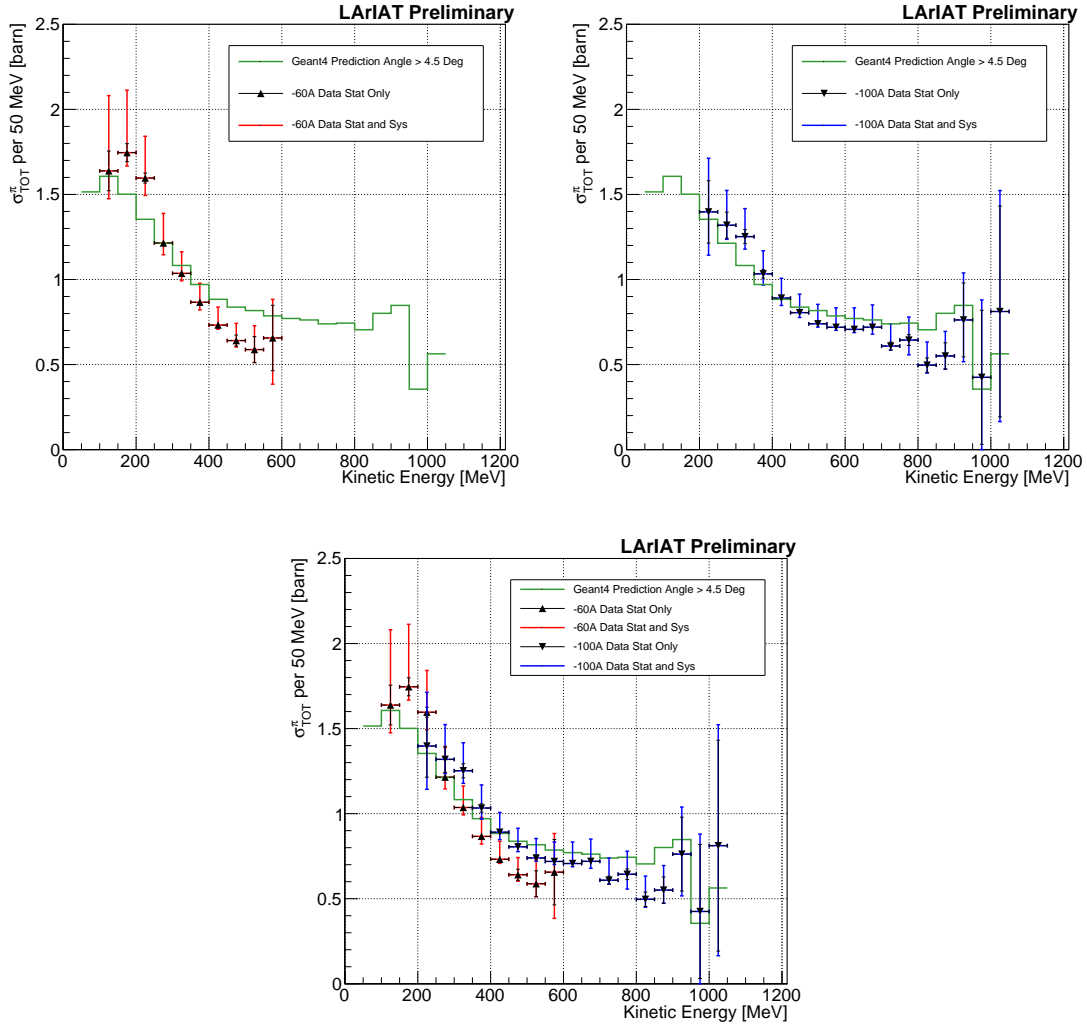


Figure 6.8: *Top Left:* (π^- -Ar) total hadronic cross section for scattering angles greater than 5° measured in the 60A sample, statistical uncertainty in black and systematic uncertainty in red. The Geant4 prediction for the total hadronic cross section for angle scattering greater than 5° is displayed in green.

Top Right: (π^- -Ar) total hadronic cross section for scattering angles greater than 5° measured in the 100A sample, statistical uncertainty in black and systematic uncertainty in blue. The Geant4 prediction for the total hadronic cross section for angle scattering greater than 5° is displayed in green.

Bottom: (π^- -Ar) total hadronic cross section measurements in the 60A and 100A samples overlaid with the Geant4 prediction (green).

2481 **Chapter 7**

2482 **Positive Kaon Cross Section**
2483 **Measurement**

2484 “Beat-up little seagull, on a marble stair
2485 Tryin’ to find the ocean, lookin’ everywhere.”
2486 – Nina Simone, 1978 –

2487 In this chapter, we show the result of the thin slice method to measure the (K^+ -
2488 Ar) total hadronic cross section. In Section 7.1, we start by measuring the raw
2489 cross section. In Section 7.2, we apply a statistical subtraction of the background
2490 contributions based on simulation and a correction for detection inefficiency. The
2491 final results are presented in Section 7.3.

2492 **7.1 Raw Cross Section**

2493 We measure the raw (K^+ -Ar) total hadronic cross section as a function of the kinetic
2494 energy in the combined +60A and +100A dataset.

2495 Similar to the pion case, the raw cross section is given by the equation 4.4

$$\sigma_{TOT}(E_i) = \frac{1}{n\delta X} \frac{N_{Int}^{TOT}(E_i)}{N_{Inc}^{TOT}(E_i)}, \quad (7.1)$$

2496 where N_{Int}^{TOT} is the measured number of particles interacting at kinetic energy E_i ,
2497 N_{Inc}^{TOT} is the measured number of particles incident on an argon slice at kinetic energy
2498 E_i , n is the density of the target centers and δX is the thickness of the argon slice.
2499 The density of the target centers and the slab thickness are $n = 0.021 \cdot 10^{24} \text{ cm}^{-3}$ and
2500 $\delta X = 0.47 \text{ cm}$, respectively.

2501 As in the case of pions, kaons might decay or interact between WC4 and the TPC
2502 front face. Some of the interaction products may be wrongly matched to the WC
2503 track, forming the “secondary” particle’s background in the kaon sample. We estimate
2504 the effect of the contamination of secondaries through the DDMC kaon sample. Figure
2505 7.1 shows the distribution of N_{Int}^{TOT} as a function of the kinetic energy. The data
2506 central points are represented by black dots, the statistical uncertainty is shown in
2507 black, while the systematic uncertainty is shown in red. Data is displayed over the
2508 N_{Int}^{TOT} distribution obtained with a DDMC sample of kaons shot from WC4. The
2509 contribution from the simulated kaons which interact hadronically is shown in pink,
2510 the contributions from kaon decay is shown in orange and the one from secondaries
2511 in red. The simulated kaon’s and secondaries’ contributions are stacked; the sum of
2512 their integrals is normalized to the integral of the data.

2513 Figure 7.2 shows the distribution of N_{Inc}^{TOT} . Data is displayed over the MC. For the
2514 N_{Inc}^{TOT} distribution we do not make a distinction between kaons that decay or interact
2515 hadronically because any kaon independently from its final interaction contributes
2516 to the flux of incident particles at given kinetic energy. The same normalization
2517 procedure is used for both the interacting and incident histograms.

2518 Figure 7.3 shows the raw cross section, statistical uncertainty in black and system-

atic uncertainty in red. The raw data cross section is overlaid to the reconstructed cross section for the MC mixed sample, displayed in azure. We calculate the statistical uncertainty for the interacting, incident and cross section distributions in a similar fashion to the pion case as described in Section 6.1.1.

As in the pion case, the only systematic effect considered in the measurement of the raw cross section results from the propagation of the uncertainty associate with the measurement of the kinetic energy at each argon slab. For kaons, the uncertainty on the kinetic energy of a candidate at the j^{th} slab of argon is given by

$$\delta KE_j = \sqrt{\delta p_{Beam}^2 + \delta E_{Loss}^2 + \delta E_{dep\ FF-j}^2} \quad (7.2)$$

$$= \sqrt{(2\% p_{Beam})^2 + (7\text{ [MeV]})^2 + (j - 1)^2(\sim 0.18\text{ [MeV]})^2}. \quad (7.3)$$

We propagate this uncertainty by varying the energy measurement KE_j at each argon slab. We measure N_{Inc}^{TOT} , N_{Int}^{TOT} and the cross section in three cases: first assigning the measured KE_j at each kinetic energy sampling, then assigning $KE_j + \delta KE_j$, and finally assigning $KE_j - \delta KE_j$. The difference between the values obtained using the KE_j sampling and the maximum and minimum values in each kinetic energy bin determines the systematic uncertainty.

7.2 Corrections to the Raw Cross Section

As described in section 4.3.3, we need to apply a background correction and an efficiency correction in order to derive the true Kaon cross section from the raw cross section. The true cross section is given in equation 4.9,

$$\sigma_{TOT}^{K^+}(E_i) = \frac{1}{n\delta X} \frac{\epsilon^{Inc}(E_i)}{\epsilon^{Int}(E_i)} \frac{C_{Int}^{KMC}(E_i)}{C_{Inc}^{KMC}(E_i)} \frac{N_{Int}^{TOT}(E_i)}{N_{Inc}^{TOT}(E_i)}. \quad (4.9)$$

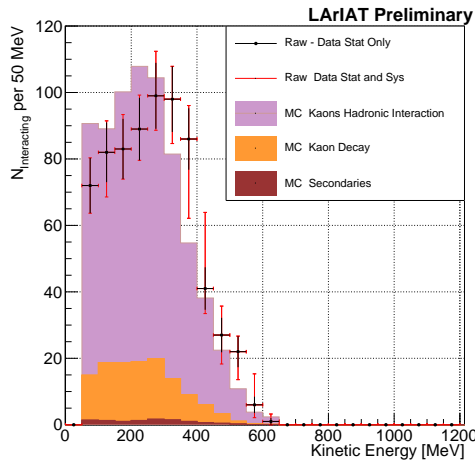


Figure 7.1: Raw number of interacting kaon candidates as a function of the reconstructed kinetic energy. The statistical uncertainties are shown in black, the systematic uncertainties in red.

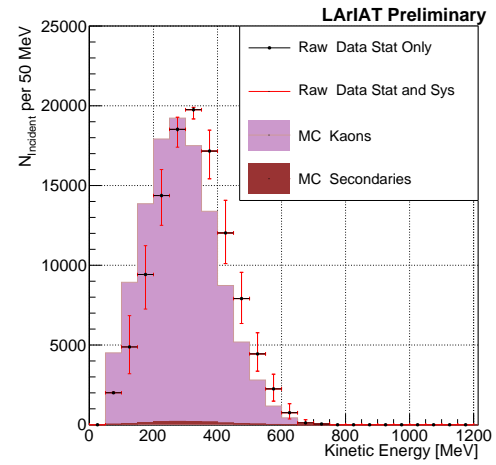


Figure 7.2: Raw number of incident kaon candidates as a function of the reconstructed kinetic energy. The statistical uncertainty is shown in black, the systematic uncertainties in red.

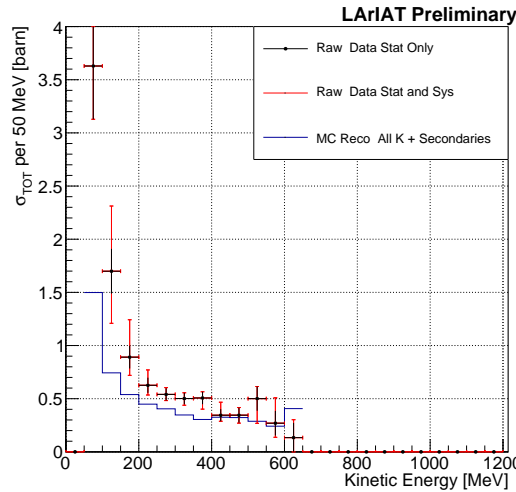


Figure 7.3: Raw (K^+ -Ar) total hadronic cross section. The statistical uncertainty is shown in black, the systematic uncertainties in red. The raw cross section obtained with a MC sample of kaons is shown in blue. For the MC cross section, we include the contributions from secondaries.

2537 Currently, the only background considered for the kaon hadronic cross section
2538 comes from the presence of secondaries. A further development of the analysis will
2539 need to account for the presence of a small proton contamination. Figure 7.4 shows
2540 the relative kaon content for the interacting and incident histograms.

2541 As described in 6.2.2 for the pion case, we derive the correction on a set of pure
2542 kaon MC, calculating its value bin by bin as the ratio between the true bin content
2543 and the correspondent reconstructed bin content. The correction is then applied to
2544 the relevant bin in data. The efficiency correction is evaluated separately for the
2545 interacting and incident histograms, namely ϵ_i^{int} and ϵ_i^{inc} , and propagated to the cross
2546 section as shown in equation 4.9.

2547 In section 5.5.1, we estimated the angular resolution for data and MC to be
2548 $\bar{\alpha}_{\text{Data}} = (4.3 \pm 3.7)$ deg and $\bar{\alpha}_{\text{MC}} = (4.4 \pm 3.6)$ deg, respectively. Most interaction
2549 angles smaller than the angular resolution will thus be indistinguishable for the re-
2550 construction. Thus, we claim we are able to measure the cross section for interaction
2551 angles greater than 4.5 deg. Geant4 simulates interactions at all angles: in order to
2552 calculate the efficiency correction, we select events which have an interaction angle
2553 greater than a α_{res} to construct the true interacting and incident histograms (the de-
2554 nominator of the efficiency correction). The systematics on the efficiency correction
2555 is estimated by varying the value of α_{res} between 0 deg and 4.5 deg and propagating
2556 the uncertainty on the cross section.

2557 Figure 7.5 shows $\epsilon^{\text{Int}}(E_i)$ in the left side and $\epsilon^{\text{Inc}}(E_i)$ on the right as a function of
2558 the kinetic energy for the kaon sample and their systematic uncertainty.

2559 7.3 Results

2560 Figure 7.6 show the measurement of the (K^+ -Ar) total hadronic cross section for
2561 scattering angles greater than 5° , as the result of the background subtraction and

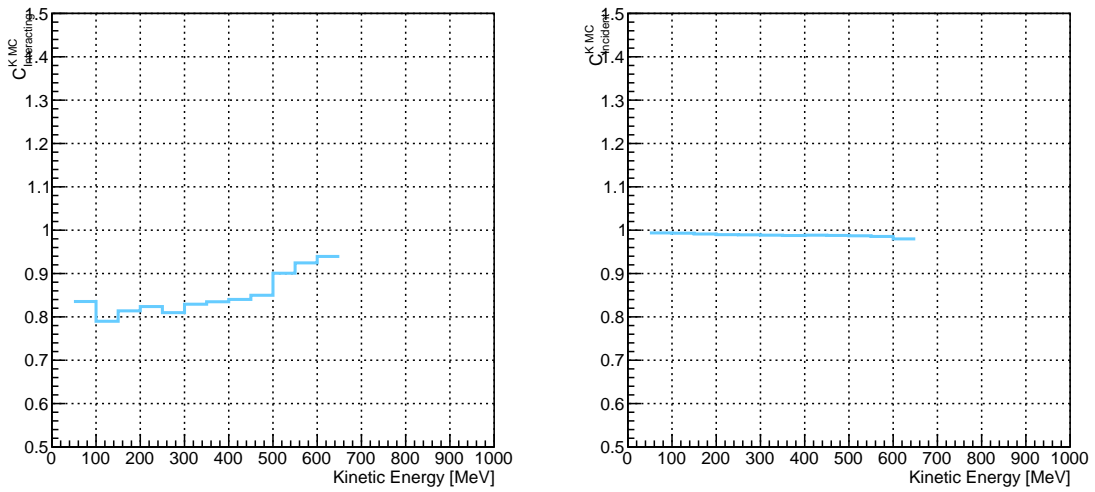


Figure 7.4: *Left:* MC estimated relative kaon content for kaons interacting hadronically as function of kinetic energy. *Right:* MC estimated relative kaon content for incident histogram a function of kinetic energy.

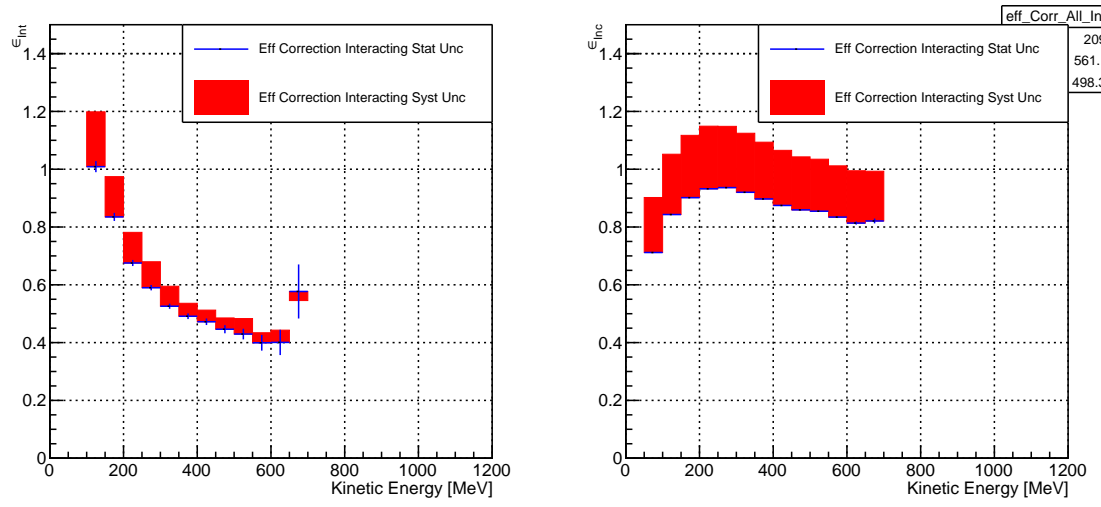


Figure 7.5: *Left:* Efficiency correction on the interacting histogram, statistical uncertainty in blue, systematic uncertainty in red. *Right:* Efficiency correction on the incident histogram, statistical uncertainty in blue, systematic uncertainty in red.

efficiency correction to the raw cross section. The plot shows the measurement obtained on the full dataset, statistical uncertainty in black and systematic uncertainty in red. The Geant4 prediction for the total hadronic cross section for angle scattering greater than 5° is displayed in green.

The systematic uncertainty on the cross section is the sum in quadrature of the statistical uncertainty, the systematic uncertainty related to the kinetic energy measurement and the systematic uncertainty related to the efficiency correction.

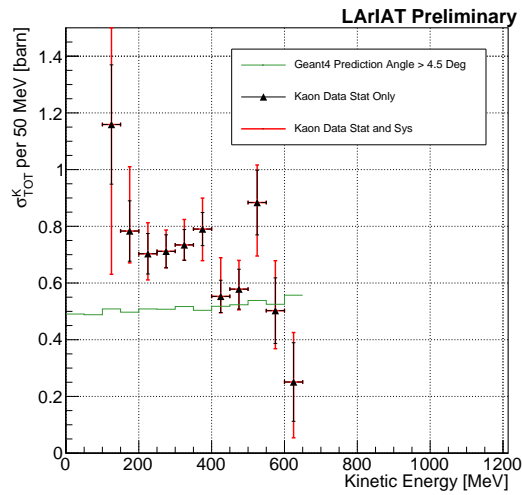


Figure 7.6: (K^+ -Ar) total hadronic cross section for scattering angles greater than 5° measured in the 60A sample, statistical uncertainty in black and systematic uncertainty in red. The Geant4 prediction for the total hadronic cross section for angle scattering greater than 5° is displayed in green.

2569 Chapter 8

2570 Conclusions

2571 **Appendix A**

2572 **Additional Tracking Studies for**
2573 **LArIAT Cross Section Analyses**

2574 In this section, we describe two studies. The first is a justification of the selection
2575 criteria for the beamline handshake with the TPC information. We perform this
2576 study to boost the correct identification of the particles in the TPC associated with
2577 the beamline information, while maintaining sufficient statistics for the cross section
2578 measurement. The second study is an optimization of the tracking algorithm, with
2579 the scope of maximizing the identification of the hadronic interaction point inside the
2580 TPC. These two studies are related, since the optimization of the tracking is per-
2581 formed on TPC tracks which have been matched to the wire chamber track; in turn,
2582 the tracking algorithm for TPC tracks determines the number of reconstructed tracks
2583 in each event used to try the matching with the wire chamber track. Starting with
2584 a sensible tracking reconstruction, we perform the WC2TPC matching optimization
2585 first, then the tracking optimization. The WC2TPC match purity and efficiency are
2586 then calculated again with the optimized tracking.

2587 **A.0.1 Study of WC to TPC Match**

2588 Plots I want in this section:

2589 1. WC2TPC MC DeltaX, DeltaY and α

2590 Scope of this study is assessing the goodness of the wire chamber to TPC match
2591 on Monte Carlo and decide the selection values we will use on data. A word of caution
2592 is necessary here. With this study, we want to minimize pathologies associated with
2593 the presence of the primary hadron itself, e.g. the incorrect association between the
2594 beamline hadron and its decay products inside the TPC. Assessing the contamination
2595 from pile-up¹, albeit related, is beyond the scope of this study.

2596 In MC, we are able to define a correct WC2TPC match using the Geant4 truth
2597 information. We are thus able to count how many times the WC tracks is associated
2598 with the wrong TPC reconstructed track.

2599 We define a correct match if the all following conditions are met:

- 2600 - the length of the true primary Geant4 track in the TPC is greater than 2 cm,
- 2601 - the length of the reconstructed track length is greater than 2 cm,
- 2602 - the Z position of the first reconstructed point is within 2 cm from the TPC
2603 front face
- 2604 - the distance between the reconstructed track and the true entering point is the
2605 minimum compared with all the other reconstructed tracks.

2606 In order to count the wrong matches, we consider all the reconstructed tracks
2607 whose Z position of the first reconstructed point lies within 2 cm from the TPC front
2608 face. Events with true length in TPC < 2 cm are included. Since hadrons are shot

1. We remind the reader that the DDMC is a single particle Monte Carlo, where the beam pile up is not simulated.

2609 100 cm upstream from the TPC front face, the following two scenarios are possible
2610 from a truth standpoint:

2611 [Ta] the primary hadron decays or interact strongly before getting to the TPC,

2612 [Tb] the primary hadron enters the TPC.

2613 As described in Section 4.2, we define a WC2TPC match according to the relative
2614 position of the WC and TPC track parametrized with ΔR and the angle between
2615 them, parametrized with α . Once we choose the selection values r_T and α_T to de-
2616 termine a reconstructed WC2TPC match, the following five scenarios are possible in
2617 the truth to reconstruction interplay :

2618 1) only the correct track is matched

2619 2) only one wrong track is matched

2620 3) the correct track and one (or more) wrong tracks are matched

2621 4) multiple wrong tracks matched.

2622 5) no reconstructed tracks are matched

2623 Since we keep only events with one and only one match, we discard cases 3), 4)
2624 and 5) from the events used in the cross section measurement. For each set of r_T and
2625 α_T selection value, we define purity and efficiency of the selection as follows:

$$\text{Efficiency} = \frac{\text{Number of events correctly matched}}{\text{Number of events with primary in TPC}}, \quad (\text{A.1})$$

$$\text{Purity} = \frac{\text{Number of events correctly matched}}{\text{Total number of matched events}}. \quad (\text{A.2})$$

2626 Figure A.1 shows the efficiency (left) and purity (right) for WC2TPC match as
2627 a function of the radius, r_T , and angle, α_T , selection value. It is apparent how both

efficiency and purity are fairly flat as a function of the radius selection value at a given angle. This is not surprising. Since we are studying a single particle gun Monte Carlo sample, the wrong matches can occur only for mis-tracking of the primary or for association with decay products; decay products will tend to be produced at large angles compared to the primary, but could be fairly close to the in x and y projection of the primary. The radius cut would play a key role in removing pile up events.

For LArIAT cross section measurements, we generally prefer purity over efficiency, since a sample of particles of a pure species will lead to a better measurement. Obviously, purity should be balanced with a sensible efficiency to avoid rejecting the whole sample.

We choose $(\alpha_T, r_T) = (8 \text{ deg}, 4 \text{ cm})$ and get a MC 85% efficiency and 98% purity for the kaon sample and a MC 95% efficiency and 90% purity for the pion sample.

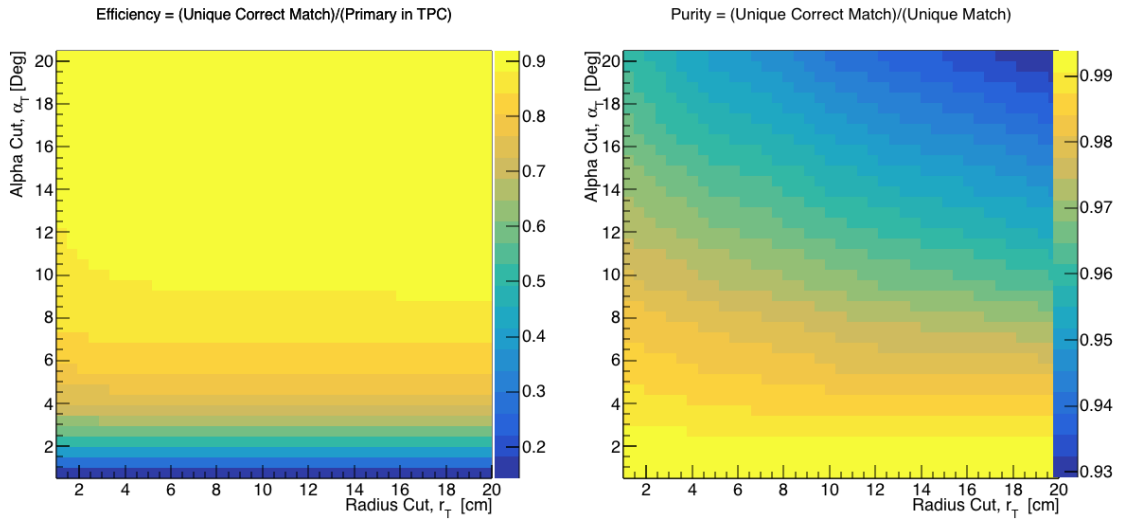


Figure A.1: Efficiency (left) and purity (right) for WC2TPC match as a function of the radius and angle selections for the kaon sample.

2640 A.0.2 Tracking Optimization

2641 **Appendix B**

2642 **Energy Calibration**

2643 Scope of the energy calibration is to identify the factors which convert the charge
2644 collected (dQ) to energy deposited in the chamber (dE). As described in section
2645 2.1.5, this is a multi-step procedure. In LArIAT, we first correct the raw charge by
2646 the electronic noise on the considered wire [104], then by the electron lifetime [105],
2647 and then by the recombination using the ArgoNeut recombination values. Lastly, we
2648 apply overall calibration of the energy, i.e. we determine the “calorimetry constants”
2649 using the procedure described in this section.

2650 We independently determine the calorimetry constants for Data and Monte Carlo
2651 in the LArIAT Run-II Data samples using a parametrization of the stopping power
2652 (a.k.a. energy deposited per unit length, dE/dX) as a function of momentum. This is
2653 done by comparing the stopping power measured on reconstructed quantities against
2654 the Bethe-Bloch theoretical prediction for various particle species (see Equation 2.1).
2655 We obtain the theoretical expectation for the dE/dX most probable value of pions
2656 (π), muons (μ), kaons (K), and protons (p) in the momentum range most relevant
2657 for LArIAT (Figure B.1) using the tables provided by the Particle Data Group [102]
2658 for liquid argon [1].

2659 The basic idea of this calibration technique is to utilize a sample of beamline

2660 events with known particle species and momentum to measure the dE/dX of the
2661 corresponding tracks in the TPC. In particular, we decided to use positive pions as
2662 calibration sample and samples from all the other particle species as cross check. Once
2663 the dE/dX of the positive pion sample has been measured at various momenta, we
2664 tune to calorimetry constants within the reconstruction software to align the measured
2665 values to match the theoretical ones found in Figure B.1.

2666 In data, we start by selecting a sample of beamline positive pion beamline can-
2667 didates without any restriction on their measured momentum¹. We then apply the
2668 WC2TPC match and subtract the energy loss upstream to the TPC front face, de-
2669 termining the momentum at the TPC front face. For each surviving pion candidate,
2670 we measure the dE/dx at each of the first 12 spacepoints associated the 3D recon-
2671 structed track, corresponding to a ~ 5 cm portion. These dE/dX measurements are
2672 then put into a histogram that corresponds to measured momentum of the track.
2673 The dE/dX histograms are sampled every 50 MeV/c in momentum (e.g. 150 MeV/c
2674 $< P < 200$ MeV/c, 200 MeV/c $< P < 250$ /c MeV, etc...). This process of selecting,
2675 sampling, and recording the dE/dX for various momentum bins is repeated over the
2676 entire sample of events, allowing us to collect sufficient statistic in most of the mo-
2677 mentum bins between 150 MeV/c and 1100 MeV/c. On average, pions and muons
2678 only lose ~ 10 MeV in this 5 cm section of the track and protons lose ~ 20 MeV. Thus
2679 choosing 50 MeV/c size bins for our histograms covers the energy spread within those
2680 bins due to energy loss from ionization for all the particle species identifiable in the
2681 beamline. Each 50 MeV/c momentum binned dE/dX histogram is now fit with a
2682 simple Landau function. The most probable value (MPV) and the associated error
2683 on the MPV from the fit are extracted and plotted against the theoretical prediction
2684 Figure B.1. Depending on the outcome of the data-prediction comparison, we modify
2685 the calorimetry constants and we repeat the procedure until a qualitative agreement

1. it should be noted that some muon and position contamination is present in the π^+ sample

2686 is achieved. We perform this tuning for the collection and induction plane separately.
 2687 As a cross check to the calorimetry constants determined using the positive pions,
 2688 we lock the constants and plot the dE/dx versus momentum distribution of all the
 2689 other particle species identifiable in the beamline data ($\pi/\mu/e$, K , p, in both polarities)
 2690 against the corresponding Beth-Bloch prediction. The agreement between data
 2691 from the other particle species and the predictions is the expected result of this cross
 2692 check. The results of the tuning and cross check for Run-II data on the collection
 2693 plane is shown in Figure B.2 negative polarity data on top, positive polarity data on
 2694 the bottom.

2695 In MC, we simulate the corresponding positive pion sample with the DDMC (see
 2696 section 5.2.2) and follow the same steps as in data. More details on the calorimetry
 2697 tuning can be found in [80].

2698 **Add agreement between data and MC for dedx for pions**

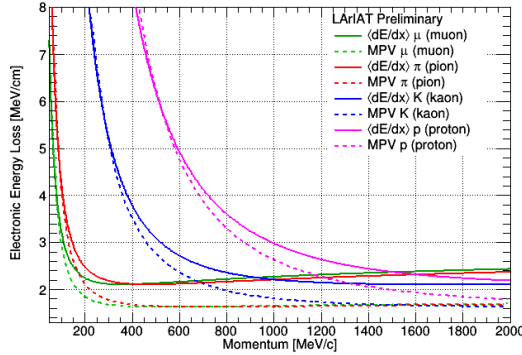


Figure B.1: Stopping power for pions, muons, kaons, and protons in liquid argon over the momentum range most relevant for LArIAT according to the Beth-Bloch equation. The solid lines represent the prediction for the mean energy dE/dX , while the dashed lines are the predictions for the MPV.

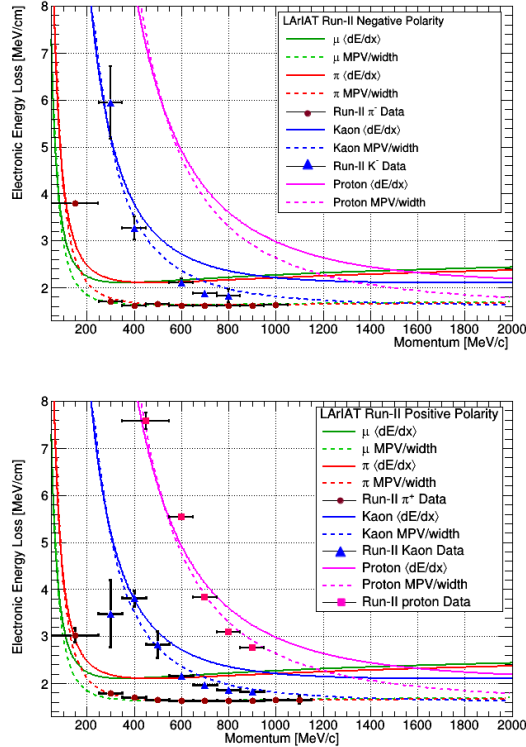


Figure B.2: Stopping power versus Momentum for Run-II negative (top) and positive (bottom) polarity data. We achieve the agreement between the Bethe-Bloch predictions and the distribution obtained with of the positive pions (top plot, red dots) by tuning the calorimetry constants. Once the calorimetry constants are locked in, the agreement between the other particle species and the Bethe-Bloch predictions follows naturally.

Bibliography

- [1] PDG Tables for Liquid Argon. . Technical report.
- [2] Precision electroweak measurements on the Z resonance. *Physics Reports*, 427(5):257 – 454, 2006.
- [3] K. Abe, J. Amey, C. Andreopoulos, M. Antonova, S. Aoki, A. Ariga, D. Autiero, S. Ban, M. Barbi, G. J. Barker, G. Barr, C. Barry, P. Bartet-Friburg, M. Batkiewicz, V. Berardi, S. Berkman, S. Bhadra, S. Bienstock, A. Blondel, S. Bolognesi, S. Bordoni, S. B. Boyd, D. Brailsford, A. Bravar, C. Bronner, M. Buizza Avanzini, R. G. Calland, T. Campbell, S. Cao, S. L. Cartwright, M. G. Catanesi, A. Cervera, C. Checchia, D. Cherdack, N. Chikuma, G. Christodoulou, A. Clifton, J. Coleman, G. Collazuol, D. Coplowe, A. Cudd, A. Dabrowska, G. De Rosa, T. Dealtry, P. F. Denner, S. R. Dennis, C. Densham, D. Dewhurst, F. Di Lodovico, S. Di Luise, S. Dolan, O. Drapier, K. E. Duffy, J. Dumarchez, M. Dziewiecki, S. Emery-Schrenk, A. Ereditato, T. Feusels, A. J. Finch, G. A. Fiorentini, M. Friend, Y. Fujii, D. Fukuda, Y. Fukuda, V. Galymov, A. Garcia, C. Giganti, F. Gizzarelli, T. Golan, M. Gonin, D. R. Hadley, L. Haegel, M. D. Haigh, D. Hansen, J. Harada, M. Hartz, T. Hasegawa, N. C. Hastings, T. Hayashino, Y. Hayato, R. L. Helmer, A. Hillairet, T. Hiraki, A. Hiramoto, S. Hirota, M. Hogan, J. Holeczek, F. Hosomi, K. Huang, A. K. Ichikawa, M. Ikeda, J. Imber, J. Insler, R. A. Intonti, T. Ishida, T. Ishii, E. Iwai, K. Iwamoto, A. Izmaylov, B. Jamieson, M. Jiang, S. Johnson, P. Jonsson,

2720 C. K. Jung, M. Kabirnezhad, A. C. Kaboth, T. Kajita, H. Kakuno, J. Kameda,
2721 D. Karlen, T. Katori, E. Kearns, M. Khabibullin, A. Khotjantsev, H. Kim,
2722 J. Kim, S. King, J. Kisiel, A. Knight, A. Knox, T. Kobayashi, L. Koch, T. Koga,
2723 A. Konaka, K. Kondo, L. L. Kormos, A. Korzenev, Y. Koshio, K. Kowalik,
2724 W. Kropp, Y. Kudenko, R. Kurjata, T. Kutter, J. Lagoda, I. Lamont, M. Lam-
2725 oureux, E. Larkin, P. Lasorak, M. Laveder, M. Lawe, M. Licciardi, T. Lindner,
2726 Z. J. Liptak, R. P. Litchfield, X. Li, A. Longhin, J. P. Lopez, T. Lou, L. Ludovici,
2727 X. Lu, L. Magaletti, K. Mahn, M. Malek, S. Manly, A. D. Marino, J. F. Martin,
2728 P. Martins, S. Martynenko, T. Maruyama, V. Matveev, K. Mavrokordis, W. Y.
2729 Ma, E. Mazzucato, M. McCarthy, N. McCauley, K. S. McFarland, C. McGrew,
2730 A. Mefodiev, C. Metelko, M. Mezzetto, P. Mijakowski, A. Minamino, O. Mi-
2731 neev, S. Mine, A. Missent, M. Miura, S. Moriyama, Th. A. Mueller, J. Myslik,
2732 T. Nakadaira, M. Nakahata, K. G. Nakamura, K. Nakamura, K. D. Nakamura,
2733 Y. Nakanishi, S. Nakayama, T. Nakaya, K. Nakayoshi, C. Nantais, C. Nielsen,
2734 M. Nirko, K. Nishikawa, Y. Nishimura, P. Novella, J. Nowak, H. M. O'Keeffe,
2735 K. Okumura, T. Okusawa, W. Oryszczak, S. M. Oser, T. Ovsyannikova, R. A.
2736 Owen, Y. Oyama, V. Palladino, J. L. Palomino, V. Paolone, N. D. Patel,
2737 P. Paudyal, M. Pavin, D. Payne, J. D. Perkin, Y. Petrov, L. Pickard, L. Pick-
2738 ering, E. S. Pinzon Guerra, C. Pistillo, B. Popov, M. Posiadala-Zezula, J.-M.
2739 Poutissou, R. Poutissou, P. Przewlocki, B. Quilain, T. Radermacher, E. Radi-
2740 cioni, P. N. Ratoff, M. Ravonel, M. A. Rayner, A. Redij, E. Reinherz-Aronis,
2741 C. Riccio, P. A. Rodrigues, E. Rondio, B. Rossi, S. Roth, A. Rubbia, A. Rychter,
2742 K. Sakashita, F. Sánchez, E. Scantamburlo, K. Scholberg, J. Schwehr, M. Scott,
2743 Y. Seiya, T. Sekiguchi, H. Sekiya, D. Sgalaberna, R. Shah, A. Shaikhiev,
2744 F. Shaker, D. Shaw, M. Shiozawa, T. Shirahige, S. Short, M. Smy, J. T.
2745 Sobczyk, H. Sobel, M. Sorel, L. Southwell, J. Steinmann, T. Stewart, P. Stowell,
2746 Y. Suda, S. Suvorov, A. Suzuki, S. Y. Suzuki, Y. Suzuki, R. Tacik, M. Tada,

2747 A. Takeda, Y. Takeuchi, H. K. Tanaka, H. A. Tanaka, D. Terhorst, R. Terri,
2748 T. Thakore, L. F. Thompson, S. Tobayama, W. Toki, T. Tomura, C. Touramani,
2749 nis, T. Tsukamoto, M. Tzanov, Y. Uchida, M. Vagins, Z. Vallari, G. Vasseur,
2750 T. Vladislavljevic, T. Wachala, C. W. Walter, D. Wark, M. O. Wascko, A. We-
2751 ber, R. Wendell, R. J. Wilkes, M. J. Wilking, C. Wilkinson, J. R. Wilson, R. J.
2752 Wilson, C. Wret, Y. Yamada, K. Yamamoto, M. Yamamoto, C. Yanagisawa,
2753 T. Yano, S. Yen, N. Yershov, M. Yokoyama, K. Yoshida, T. Yuan, M. Yu, A. Za-
2754 lewska, J. Zalipska, L. Zambelli, K. Zaremba, M. Ziembicki, E. D. Zimmerman,
2755 M. Zito, and J. Źmuda. Combined analysis of neutrino and antineutrino oscil-
2756 lations at t2k. *Phys. Rev. Lett.*, 118:151801, Apr 2017.

2757 [4] K. Abe, Y. Haga, Y. Hayato, M. Ikeda, K. Iyogi, J. Kameda, Y. Kishimoto,
2758 M. Miura, S. Moriyama, M. Nakahata, T. Nakajima, Y. Nakano, S. Nakayama,
2759 A. Orii, H. Sekiya, M. Shiozawa, A. Takeda, H. Tanaka, T. Tomura, R. A. Wen-
2760 dell, R. Akutsu, T. Irvine, T. Kajita, K. Kaneyuki, Y. Nishimura, E. Richard,
2761 K. Okumura, L. Labarga, P. Fernandez, J. Gustafson, C. Kachulis, E. Kearns,
2762 J. L. Raaf, J. L. Stone, L. R. Sulak, S. Berkman, C. M. Nantais, H. A.
2763 Tanaka, S. Tobayama, M. Goldhaber, W. R. Kropp, S. Mine, P. Weatherly,
2764 M. B. Smy, H. W. Sobel, V. Takhistov, K. S. Ganezer, B. L. Hartfiel, J. Hill,
2765 N. Hong, J. Y. Kim, I. T. Lim, R. G. Park, A. Himmel, Z. Li, E. O’Sullivan,
2766 K. Scholberg, C. W. Walter, T. Wongjirad, T. Ishizuka, S. Tasaka, J. S. Jang,
2767 J. G. Learned, S. Matsuno, S. N. Smith, M. Friend, T. Hasegawa, T. Ishida,
2768 T. Ishii, T. Kobayashi, T. Nakadaira, K. Nakamura, Y. Oyama, K. Sakashita,
2769 T. Sekiguchi, T. Tsukamoto, A. T. Suzuki, Y. Takeuchi, T. Yano, S. V. Cao,
2770 T. Hiraki, S. Hirota, K. Huang, T. Kikawa, A. Minamino, T. Nakaya, K. Suzuki,
2771 Y. Fukuda, K. Choi, Y. Itow, T. Suzuki, P. Mijakowski, K. Frankiewicz, J. Hig-
2772 night, J. Imber, C. K. Jung, X. Li, J. L. Palomino, M. J. Wilking, C. Yanag-
2773 isawa, D. Fukuda, H. Ishino, T. Kayano, A. Kibayashi, Y. Koshio, T. Mori,

- 2774 M. Sakuda, C. Xu, Y. Kuno, R. Tacik, S. B. Kim, H. Okazawa, Y. Choi,
2775 K. Nishijima, M. Koshiba, Y. Totsuka, Y. Suda, M. Yokoyama, C. Bronner,
2776 M. Hartz, K. Martens, Ll. Marti, Y. Suzuki, M. R. Vagins, J. F. Martin, A. Kon-
2777 aka, S. Chen, Y. Zhang, and R. J. Wilkes. Search for proton decay via $p \rightarrow e^+ \pi^0$
2778 and $p \rightarrow \mu^+ \pi^0$ in 0.31 megaton · years exposure of the super-kamiokande water
2779 cherenkov detector. *Phys. Rev. D*, 95:012004, Jan 2017.
- 2780 [5] R Acciarri, C Adams, J Asaadi, B Baller, T Bolton, C Bromberg, F Ca-
2781 vanna, E Church, D Edmunds, A Ereditato, S Farooq, B Fleming, H Greenlee,
2782 G Horton-Smith, C James, E Klein, K Lang, P Laurens, D McKee, R Mehdiyev,
2783 B Page, O Palamara, K Partyka, G Rameika, B Rebel, M Soderberg, J Spitz,
2784 A M Szelc, M Weber, M Wojcik, T Yang, and G P Zeller. A study of electron
2785 recombination using highly ionizing particles in the argoneut liquid argon tpc.
2786 *Journal of Instrumentation*, 8(08):P08005, 2013.
- 2787 [6] R Acciarri, M Antonello, B Baibussinov, M Baldo-Ceolin, P Benetti,
2788 F Calaprice, E Calligarich, M Cambiaghi, N Canci, F Carbonara, F Cavanna,
2789 S Centro, A G Cocco, F Di Pompeo, G Fiorillo, C Galbiati, V Gallo, L Grandi,
2790 G Meng, I Modena, C Montanari, O Palamara, L Pandola, G B Piano Mortari,
2791 F Pietropaolo, G L Raselli, M Roncadelli, M Rossella, C Rubbia, E Segreto,
2792 A M Szelc, S Ventura, and C Vignoli. Effects of nitrogen contamination in
2793 liquid argon. *Journal of Instrumentation*, 5(06):P06003, 2010.
- 2794 [7] R. Acciarri et al. Demonstration and Comparison of Operation of Photomulti-
2795 plier Tubes at Liquid Argon Temperature. *JINST*, 7:P01016, 2012.
- 2796 [8] R. Acciarri et al. Design and Construction of the MicroBooNE Detector. *JINST*,
2797 12(02):P02017, 2017.

- 2798 [9] R. Acciarri et al. First Observation of Low Energy Electron Neutrinos in a
2799 Liquid Argon Time Projection Chamber. *Phys. Rev.*, D95(7):072005, 2017.
2800 [Phys. Rev.D95,072005(2017)].
- 2801 [10] M Adamowski, B Carls, E Dvorak, A Hahn, W Jaskierny, C Johnson, H Jostlein,
2802 C Kendziora, S Lockwitz, B Pahlka, R Plunkett, S Pordes, B Rebel, R Schmitt,
2803 M Stancari, T Tope, E Voirin, and T Yang. The liquid argon purity demon-
2804 strator. *Journal of Instrumentation*, 9(07):P07005, 2014.
- 2805 [11] C. Adams et al. The Long-Baseline Neutrino Experiment: Exploring Funda-
2806 mental Symmetries of the Universe. 2013.
- 2807 [12] P. Adamson, L. Aliaga, D. Ambrose, N. Anfimov, A. Antoshkin, E. Arrieta-
2808 Diaz, K. Augsten, A. Aurisano, C. Backhouse, M. Baird, B. A. Bambah,
2809 K. Bays, B. Behera, S. Bending, R. Bernstein, V. Bhatnagar, B. Bhuyan,
2810 J. Bian, T. Blackburn, A. Bolshakova, C. Bromberg, J. Brown, G. Brunetti,
2811 N. Buchanan, A. Butkevich, V. Bychkov, M. Campbell, E. Catano-Mur, S. Chil-
2812 dress, B. C. Choudhary, B. Chowdhury, T. E. Coan, J. A. B. Coelho, M. Colo,
2813 J. Cooper, L. Corwin, L. Cremonesi, D. Cronin-Hennessy, G. S. Davies, J. P.
2814 Davies, P. F. Derwent, R. Dharmapalan, P. Ding, Z. Djurcic, E. C. Dukes,
2815 H. Duyang, S. Edayath, R. Ehrlich, G. J. Feldman, M. J. Frank, M. Gabrielyan,
2816 H. R. Gallagher, S. Germani, T. Ghosh, A. Giri, R. A. Gomes, M. C. Goodman,
2817 V. Grichine, R. Group, D. Grover, B. Guo, A. Habig, J. Hartnell, R. Hatcher,
2818 A. Hatzikoutelis, K. Heller, A. Himmel, A. Holin, J. Hylen, F. Jediny, M. Judah,
2819 G. K. Kafka, D. Kalra, S. M. S. Kasahara, S. Kasetti, R. Keloth, L. Kolupaeva,
2820 S. Kotelnikov, I. Kourbanis, A. Kreymer, A. Kumar, S. Kurbanov, K. Lang,
2821 W. M. Lee, S. Lin, J. Liu, M. Lokajicek, J. Lozier, S. Luchuk, K. Maan, S. Mag-
2822 ill, W. A. Mann, M. L. Marshak, K. Matera, V. Matveev, D. P. Méndez, M. D.
2823 Messier, H. Meyer, T. Miao, W. H. Miller, S. R. Mishra, R. Mohanta, A. Moren,

- 2824 L. Mualem, M. Muether, S. Mufson, R. Murphy, J. Musser, J. K. Nelson,
2825 R. Nichol, E. Niner, A. Norman, T. Nosek, Y. Oksuzian, A. Olshevskiy, T. Ol-
2826 son, J. Paley, P. Pandey, R. B. Patterson, G. Pawloski, D. Pershey, O. Petrova,
2827 R. Petti, S. Phan-Budd, R. K. Plunkett, R. Poling, B. Potukuchi, C. Principato,
2828 F. Psihas, A. Radovic, R. A. Rameika, B. Rebel, B. Reed, D. Rocco, P. Rojas,
2829 V. Ryabov, K. Sachdev, P. Sail, O. Samoylov, M. C. Sanchez, R. Schroeter,
2830 J. Sepulveda-Quiroz, P. Shanahan, A. Sheshukov, J. Singh, J. Singh, P. Singh,
2831 V. Singh, J. Smolik, N. Solomey, E. Song, A. Sousa, K. Soustruznik, M. Strait,
2832 L. Suter, R. L. Talaga, M. C. Tamsett, P. Tas, R. B. Thayyullathil, J. Thomas,
2833 X. Tian, S. C. Tognini, J. Tripathi, A. Tsaris, J. Urheim, P. Vahle, J. Vasel,
2834 L. Vinton, A. Vold, T. Vrba, B. Wang, M. Wetstein, D. Whittington, S. G. Wo-
2835 jcicki, J. Wolcott, N. Yadav, S. Yang, J. Zalesak, B. Zamorano, and R. Zwaska.
2836 Constraints on oscillation parameters from ν_e appearance and ν_μ disappearance
2837 in nova. *Phys. Rev. Lett.*, 118:231801, Jun 2017.
- 2838 [13] Alan Agresti. *Categorical Data Analysis*. Wiley Series in Probability and Statis-
2839 tics. Wiley, 2013.
- 2840 [14] A. Aguilar-Arevalo et al. Evidence for neutrino oscillations from the observation
2841 of anti-neutrino(electron) appearance in a anti-neutrino(muon) beam. *Phys.*
2842 *Rev.*, D64:112007, 2001.
- 2843 [15] A. A. Aguilar-Arevalo et al. Improved Search for $\bar{\nu}_\mu \rightarrow \bar{\nu}_e$ Oscillations in the
2844 MiniBooNE Experiment. *Phys. Rev. Lett.*, 110:161801, 2013.
- 2845 [16] S. Amoruso et al. Study of electron recombination in liquid argon with the
2846 ICARUS TPC. *Nucl. Instrum. Meth.*, A523:275–286, 2004.
- 2847 [17] C. Anderson et al. The ArgoNeuT Detector in the NuMI Low-Energy beam
2848 line at Fermilab. *JINST*, 7:P10019, 2012.

- 2849 [18] C. Andreopoulos et al. The GENIE Neutrino Monte Carlo Generator. *Nucl.*
2850 *Instrum. Meth.*, A614:87–104, 2010.
- 2851 [19] Timofei Bolshakov Andrey Petrov. Java synoptic toolkit. Technical report,
2852 Sept 2010.
- 2853 [20] M. Antonello, B. Baibussinov, P. Benetti, E. Calligarich, N. Canci, S. Cen-
2854 tro, A. Cesana, K. Cieslik, D. B. Cline, A. G. Cocco, A. Dabrowska, D. De-
2855 qual, A. Dermenev, R. Dolfini, C. Farnese, A. Fava, A. Ferrari, G. Fiorillo,
2856 D. Gibin, S. Gninenko, A. Guglielmi, M. Haranczyk, J. Holeczek, A. Ivashkin,
2857 J. Kisiel, I. Kochanek, J. Lagoda, S. Mania, A. Menegolli, G. Meng, C. Monta-
2858 nari, S. Otwinowski, A. Piazzoli, P. Picchi, F. Pietropaolo, P. Plonski, A. Rap-
2859 poldi, G. L. Raselli, M. Rossella, C. Rubbia, P. Sala, A. Scaramelli, E. Seg-
2860 reto, F. Sergiampietri, D. Stefan, J. Stepaniak, R. Sulej, M. Szarska, M. Ter-
2861 rani, F. Varanini, S. Ventura, C. Vignoli, H. Wang, X. Yang, A. Zalewska,
2862 and K. Zaremba. Precise 3d track reconstruction algorithm for the ICARUS
2863 t600 liquid argon time projection chamber detector. *Advances in High Energy*
2864 *Physics*, 2013:1–16, 2013.
- 2865 [21] M. Antonello et al. A Proposal for a Three Detector Short-Baseline Neutrino
2866 Oscillation Program in the Fermilab Booster Neutrino Beam. 2015.
- 2867 [22] D. Ashery, I. Navon, G. Azuelos, H. K. Walter, H. J. Pfeiffer, and F. W.
2868 Schlepütz. True absorption and scattering of pions on nuclei. *Phys. Rev. C*,
2869 23:2173–2185, May 1981.
- 2870 [23] C. Athanassopoulos et al. Evidence for $\nu(\mu) \rightarrow \nu(e)$ neutrino oscillations
2871 from LSND. *Phys. Rev. Lett.*, 81:1774–1777, 1998.

- 2872 [24] Borut Bajc, Junji Hisano, Takumi Kuwahara, and Yuji Omura. Threshold
2873 corrections to dimension-six proton decay operators in non-minimal {SUSY}
2874 $\text{su}(5)$ {GUTs}. *Nuclear Physics B*, 910:1 – 22, 2016.
- 2875 [25] B. Baller. Trajcluster user guide. Technical report, apr 2016.
- 2876 [26] Gary Barker. Neutrino event reconstruction in a liquid argon TPC. *Journal of*
2877 *Physics: Conference Series*, 308:012015, jul 2011.
- 2878 [27] BASF Corp. 100 Park Avenue, Florham Park, NJ 07932 USA.
- 2879 [28] R. Becker-Szendy, C. B. Bratton, D. R. Cady, D. Casper, R. Claus, M. Crouch,
2880 S. T. Dye, W. Gajewski, M. Goldhaber, T. J. Haines, P. G. Halverson, T. W.
2881 Jones, D. Kielczewska, W. R. Kropp, J. G. Learned, J. M. LoSecco, C. Mc-
2882 Grew, S. Matsuno, J. Matthews, M. S. Mudah, L. Price, F. Reines, J. Schultz,
2883 D. Sinclair, H. W. Sobel, J. L. Stone, L. R. Sulak, R. Svoboda, G. Thornton,
2884 and J. C. van der Velde. Search for proton decay into $e^+ + \pi^0$ in the imb-3
2885 detector. *Phys. Rev. D*, 42:2974–2976, Nov 1990.
- 2886 [29] J B Birks. Scintillations from organic crystals: Specific fluorescence and relative
2887 response to different radiations. *Proceedings of the Physical Society. Section A*,
2888 64(10):874, 1951.
- 2889 [30] A. Bodek and J. L. Ritchie. Further studies of fermi-motion effects in lepton
2890 scattering from nuclear targets. *Phys. Rev. D*, 24:1400–1402, Sep 1981.
- 2891 [31] Mark G. Boulay and A. Hime. Direct WIMP detection using scintillation time
2892 discrimination in liquid argon. 2004.
- 2893 [32] D. V. Bugg, R. S. Gilmore, K. M. Knight, D. C. Salter, G. H. Stafford, E. J. N.
2894 Wilson, J. D. Davies, J. D. Dowell, P. M. Hattersley, R. J. Homer, A. W. O'dell,

- 2895 A. A. Carter, R. J. Tapper, and K. F. Riley. Kaon-nucleon total cross sections
2896 from 0.6 to 2.65 gev/ *c. Phys. Rev.*, 168:1466–1475, Apr 1968.
- 2897 [33] W. M. Burton and B. A. Powell. Fluorescence of tetraphenyl-butadiene in the
2898 vacuum ultraviolet. *Applied Optics*, 12(1):87, jan 1973.
- 2899 [34] CAEN. Caen v1495 data sheet. Technical report, jan 2018.
- 2900 [35] CAEN. Caen v1740 data sheet. Technical report, jan 2018.
- 2901 [36] A. S. Carroll, I. H. Chiang, C. B. Dover, T. F. Kycia, K. K. Li, P. O. Mazur,
2902 D. N. Michael, P. M. Mockett, D. C. Rahm, and R. Rubinstein. Pion-nucleus
2903 total cross sections in the (3,3) resonance region. *Phys. Rev. C*, 14:635–638,
2904 Aug 1976.
- 2905 [37] D. Casper. The nuance neutrino physics simulation, and the future. *Nuclear
2906 Physics B - Proceedings Supplements*, 112(1-3):161–170, nov 2002.
- 2907 [38] F. Cavanna et al. LArIAT: Liquid Argon In A Testbeam. 2014.
- 2908 [39] A. Cervera, A. Donini, M.B. Gavela, J.J. Gomez Cádenas, P. Hernández,
2909 O. Mena, and S. Rigolin. Golden measurements at a neutrino factory. *Nu-
2910 clear Physics B*, 579(1-2):17–55, jul 2000.
- 2911 [40] E. Church. LArSoft: A Software Package for Liquid Argon Time Projection
2912 Drift Chambers. 2013.
- 2913 [41] ATLAS Collaboration. Observation of a new particle in the search for the
2914 standard model higgs boson with the ATLAS detector at the LHC. *Physics
2915 Letters B*, 716(1):1–29, sep 2012.
- 2916 [42] CMS Collaboration. Observation of a new boson at a mass of 125 gev with the
2917 cms experiment at the lhc. *Physics Letters B*, 716(1):30 – 61, 2012.

- 2918 [43] The LArIAT Collaboration. The liquid argon in a testbeam (lariat) experiment.
2919 Technical report, In Preparation 2018.
- 2920 [44] Stefano Dell’Oro, Simone Marcocci, Matteo Viel, and Francesco Vissani. Neu-
2921 trinoless double beta decay: 2015 review. *Advances in High Energy Physics*,
2922 2016:1–37, 2016.
- 2923 [45] S.E. Derenzo, A.R. Kirschbaum, P.H. Eberhard, R.R. Ross, and F.T. Solmitz.
2924 Test of a liquid argon chamber with 20 m rms resolution. *Nuclear Instruments
and Methods*, 122:319 – 327, 1974.
- 2926 [46] Savas Dimopoulos, Stuart Raby, and Frank Wilczek. Proton Decay in Super-
2927 symmetric Models. *Phys. Lett.*, B112:133, 1982.
- 2928 [47] D. Drakoulakos et al. Proposal to perform a high-statistics neutrino scattering
2929 experiment using a fine-grained detector in the NuMI beam. 2004.
- 2930 [48] A Ereditato, C C Hsu, S Janos, I Kreslo, M Messina, C Rudolf von Rohr,
2931 B Rossi, T Strauss, M S Weber, and M Zeller. Design and operation of
2932 argontube: a 5 m long drift liquid argon tpc. *Journal of Instrumentation*,
2933 8(07):P07002, 2013.
- 2934 [49] Torleif Ericson and Wolfram Weise. *Pions and Nuclei (The International Series
of Monographs on Physics)*. Oxford University Press, 1988.
- 2936 [50] A.A. Aguilar-Arevalo et al. The miniboone detector. *Nuclear Instruments and
2937 Methods in Physics Research Section A: Accelerators, Spectrometers, Detectors
2938 and Associated Equipment*, 599(1):28 – 46, 2009.
- 2939 [51] Antonio Bueno et al. Nucleon decay searches with large liquid argon TPC de-
2940 tectors at shallow depths: atmospheric neutrinos and cosmogenic backgrounds.
2941 *Journal of High Energy Physics*, 2007(04):041–041, apr 2007.

- 2942 [52] A.S. Clough et al. Pion-nucleus total cross sections from 88 to 860 MeV. *Nuclear*
2943 *Physics B*, 76(1):15–28, jul 1974.
- 2944 [53] B.W. Allardice et al. Pion reaction cross sections and nuclear sizes. *Nuclear*
2945 *Physics A*, 209(1):1 – 51, 1973.
- 2946 [54] C Athanassopoulos et al. The liquid scintillator neutrino detector and LAMPF
2947 neutrino source. *Nuclear Instruments and Methods in Physics Research Section*
2948 *A: Accelerators, Spectrometers, Detectors and Associated Equipment*, 388(1-
2949 2):149–172, mar 1997.
- 2950 [55] F. Binon et al. Scattering of negative pions on carbon. *Nuclear Physics B*,
2951 17(1):168 – 188, 1970.
- 2952 [56] L. Aliaga et al. Minerva neutrino detector response measured with test beam
2953 data. *Nuclear Instruments and Methods in Physics Research Section A: Ac-*
2954 *celerators, Spectrometers, Detectors and Associated Equipment*, 789:28 – 42,
2955 2015.
- 2956 [57] M Adamowski et al. The liquid argon purity demonstrator. *Journal of Instru-*
2957 *mentation*, 9(07):P07005, 2014.
- 2958 [58] P. Vilain et al. Coherent single charged pion production by neutrinos. *Physics*
2959 *Letters B*, 313(1-2):267–275, aug 1993.
- 2960 [59] R. Acciarri et al. Convolutional neural networks applied to neutrino events
2961 in a liquid argon time projection chamber. *Journal of Instrumentation*,
2962 12(03):P03011, 2017.
- 2963 [60] R. Acciarri et al. Design and construction of the MicroBooNE detector. *Journal*
2964 *of Instrumentation*, 12(02):P02017–P02017, feb 2017.

- 2965 [61] C. E. Aalseth et al.l. DarkSide-20k: A 20 tonne two-phase LAr TPC for direct
2966 dark matter detection at LNGS. *The European Physical Journal Plus*, 133(3),
2967 mar 2018.
- 2968 [62] H Fenker. Standard beam pwc for fermilab. Technical report, Fermi National
2969 Accelerator Lab., Batavia, IL (USA), 1983.
- 2970 [63] H Fesbach. Theoretical nuclear physics: Nuclear reactions. 1992.
- 2971 [64] J. A. Formaggio and G. P. Zeller. From ev to eev: Neutrino cross sections across
2972 energy scales. *Rev. Mod. Phys.*, 84:1307–1341, Sep 2012.
- 2973 [65] E. Friedman et al. K+ nucleus reaction and total cross-sections: New analysis
2974 of transmission experiments. *Phys. Rev.*, C55:1304–1311, 1997.
- 2975 [66] V.M. Gehman, S.R. Seibert, K. Rielage, A. Hime, Y. Sun, D.-M. Mei,
2976 J. Maassen, and D. Moore. Fluorescence efficiency and visible re-emission
2977 spectrum of tetraphenyl butadiene films at extreme ultraviolet wavelengths.
2978 *Nuclear Instruments and Methods in Physics Research Section A: Accelerators,*
2979 *Spectrometers, Detectors and Associated Equipment*, 654(1):116 – 121, 2011.
- 2980 [67] H. Geiger and E. Marsden. On a diffuse reflection of the formula-particles.
2981 *Proceedings of the Royal Society A: Mathematical, Physical and Engineering*
2982 *Sciences*, 82(557):495–500, jul 1909.
- 2983 [68] Howard Georgi and S. L. Glashow. Unity of all elementary-particle forces. *Phys.*
2984 *Rev. Lett.*, 32:438–441, Feb 1974.
- 2985 [69] G. Giacomelli. Introduction to the Workshop “30 years of bubble chamber
2986 physics”. *ArXiv Physics e-prints*, April 2006.
- 2987 [70] D.Y. Wong (editor) G.L. Shaw (Editor). *Pion-nucleon Scattering*. John Wiley
2988 & Sons Inc, 1969.

- 2989 [71] Glassman High Voltage, Inc., Precision Regulated High Voltage DC Power Sup-
2990 ply.
- 2991 [72] D S Gorbunov. Sterile neutrinos and their role in particle physics and cosmology.
2992 *Physics-Uspekhi*, 57(5):503, 2014.
- 2993 [73] C. Green, J. Kowalkowski, M. Paterno, M. Fischler, L. Garren, and Q. Lu. The
2994 Art Framework. *J. Phys. Conf. Ser.*, 396:022020, 2012.
- 2995 [74] S. Hansen, D. Jensen, G. Savage, E. Skup, and A. Soha. Fermilab test beam
2996 multi-wire proportional chamber tracking system upgrade. June 2014. Interna-
2997 tional Conference on Technology and Instrumentation in Particle Physics (TIPP
2998 2014).
- 2999 [75] J. Harada. Non-maximal θ_{23} , large θ_{13} and tri-bimaximal θ_{12} via quark-
3000 lepton complementarity at next-to-leading order. *EPL (Europhysics Letters)*,
3001 103(2):21001, 2013.
- 3002 [76] Peter W. Higgs. Broken symmetries and the masses of gauge bosons. *Physical*
3003 *Review Letters*, 13(16):508–509, oct 1964.
- 3004 [77] P.W. Higgs. Broken symmetries, massless particles and gauge fields. *Physics*
3005 *Letters*, 12(2):132–133, sep 1964.
- 3006 [78] H J Hilke. Time projection chambers. *Reports on Progress in Physics*,
3007 73(11):116201, 2010.
- 3008 [79] N. Ishida, M. Chen, T. Doke, K. Hasuike, A. Hitachi, M. Gaudreau, M. Kase,
3009 Y. Kawada, J. Kikuchi, T. Komiyama, K. Kuwahara, K. Masuda, H. Okada,
3010 Y.H. Qu, M. Suzuki, and T. Takahashi. Attenuation length measurements of
3011 scintillation light in liquid rare gases and their mixtures using an improved
3012 reflection suppresser. *Nuclear Instruments and Methods in Physics Research*

- 3013 *Section A: Accelerators, Spectrometers, Detectors and Associated Equipment*,
3014 384(2-3):380–386, jan 1997.
- 3015 [80] G. Pulliam J. Asaadi, E. Gramellini. Determination of the electron lifetime in
3016 lariat. Technical report, August 2017.
- 3017 [81] George Jaffé. Zur theorie der ionisation in kolonnen. *Annalen der Physik*,
3018 347(12):303–344, 1913.
- 3019 [82] C. Jarlskog. A basis independent formulation of the connection between quark
3020 mass matrices, CP violation and experiment. *Zeitschrift für Physik C Particles
3021 and Fields*, 29(3):491–497, sep 1985.
- 3022 [83] B J P Jones, C S Chiu, J M Conrad, C M Ignarra, T Katori, and M Toups. A
3023 measurement of the absorption of liquid argon scintillation light by dissolved ni-
3024 trogen at the part-per-million level. *Journal of Instrumentation*, 8(07):P07011,
3025 2013.
- 3026 [84] Benjamin J. P. Jones. *Sterile Neutrinos in Cold Climates*. PhD thesis, MIT,
3027 2015.
- 3028 [85] Cezary Juszczak, Jarosław A. Nowak, and Jan T. Sobczyk. Simulations from
3029 a new neutrino event generator. *Nuclear Physics B - Proceedings Supplements*,
3030 159:211–216, sep 2006.
- 3031 [86] D. I. Kazakov. Beyond the standard model: In search of supersymmetry. In
3032 *2000 European School of high-energy physics, Caramulo, Portugal, 20 Aug-2*
3033 *Sep 2000: Proceedings*, pages 125–199, 2000.
- 3034 [87] Dae-Gyu Lee, R. N. Mohapatra, M. K. Parida, and Merostar Rani. Predic-
3035 tions for the proton lifetime in minimal nonsupersymmetric $so(10)$ models: An
3036 update. *Phys. Rev. D*, 51:229–235, Jan 1995.

- 3037 [88] M A Leigui de Oliveira. Expression of Interest for a Full-Scale Detector Engi-
3038 neering Test and Test Beam Calibration of a Single-Phase LAr TPC. Technical
3039 Report CERN-SPSC-2014-027. SPSC-EOI-011, CERN, Geneva, Oct 2014.
- 3040 [89] W. H. Lippincott, K. J. Coakley, D. Gastler, A. Hime, E. Kearns, D. N. McK-
3041 insey, J. A. Nikkel, and L. C. Stonehill. Scintillation time dependence and pulse
3042 shape discrimination in liquid argon. *Phys. Rev. C*, 78:035801, Sep 2008.
- 3043 [90] Jorge L. Lopez and Dimitri V. Nanopoulos. Flipped SU(5): Origins and re-
3044 cent developments. In *15th Johns Hopkins Workshop on Current Problems*
3045 *in Particle Theory: Particle Physics from Underground to Heaven Baltimore,*
3046 *Maryland, August 26-28, 1991*, pages 277–297, 1991.
- 3047 [91] Vincent Lucas and Stuart Raby. Nucleon decay in a realistic so(10) susy gut.
3048 *Phys. Rev. D*, 55:6986–7009, Jun 1997.
- 3049 [92] Ettore Majorana. Teoria simmetrica dell'elettrone e del positrone. *Il Nuovo*
3050 *Cimento*, 14(4):171–184, apr 1937.
- 3051 [93] Hisakazu Minakata and Alexei Yu. Smirnov. Neutrino mixing and quark-lepton
3052 complementarity. *Phys. Rev. D*, 70:073009, Oct 2004.
- 3053 [94] M. Mooney. The microboone experiment and the impact of space charge effects.
3054 2015.
- 3055 [95] E. Morikawa, R. Reininger, P. Gürtler, V. Saile, and P. Laporte. Argon, kryp-
3056 ton, and xenon excimer luminescence: From the dilute gas to the condensed
3057 phase. *The Journal of Chemical Physics*, 91(3):1469–1477, aug 1989.
- 3058 [96] FM Newcomer, S Tedja, R Van Berg, J Van der Spiegel, and HH Williams.
3059 A fast, low power, amplifier-shaper-discriminator for high rate straw tracking
3060 systems. *IEEE Transactions on Nuclear Science*, 40(4):630–636, 1993.

- 3061 [97] Emmy Noether. Invariant variation problems. *Transport Theory and Statistical*
3062 *Physics*, 1(3):186–207, jan 1971.
- 3063 [98] I. Nutini. Study of charged particles interaction processes on ar in the 0.2 - 2.0
3064 GeV energy range through combined information from ionization free charge
3065 and scintillation light. Technical report, jan 2015.
- 3066 [99] D. R. Nygren. The time projection chamber: A new 4π detector for charged
3067 particles. Technical report, 1974.
- 3068 [100] L. Onsager. Initial recombination of ions. *Phys. Rev.*, 54:554–557, Oct 1938.
- 3069 [101] S. Pascoli, S.T. Petcov, and A. Riotto. Leptogenesis and low energy cp-violation
3070 in neutrino physics. *Nuclear Physics B*, 774(1):1 – 52, 2007.
- 3071 [102] C. Patrignani et al. Review of Particle Physics. *Chin. Phys.*, C40(10):100001,
3072 2016.
- 3073 [103] B. Pontecorvo. Neutrino Experiments and the Problem of Conservation of
3074 Leptonic Charge. *Sov. Phys. JETP*, 26:984–988, 1968. [Zh. Eksp. Teor.
3075 Fiz.53,1717(1967)].
- 3076 [104] T. Yang R. Acciarri. Investigation of the non-uniformity observed in the wire
3077 response to charge in lariat run 1. Technical report, February 2017.
- 3078 [105] T. Yang R. Acciarri, M. Stancari. Determination of the electron lifetime in
3079 lariat. Technical report, March 2016.
- 3080 [106] Martti Raidal. Relation between the neutrino and quark mixing angles and
3081 grand unification. *Phys. Rev. Lett.*, 93:161801, Oct 2004.
- 3082 [107] Steve Ritz et al. Building for Discovery: Strategic Plan for U.S. Particle Physics
3083 in the Global Context. 2014.

- 3084 [108] C. Rubbia. The Liquid Argon Time Projection Chamber: A New Concept for
3085 Neutrino Detectors. 1977.
- 3086 [109] L.M. Saunders. Electromagnetic production of pions from nuclei. *Nucl. Phys.*,
3087 *B7*: 293-310(1968).
- 3088 [110] Qaisar Shafi and Zurab Tavartkiladze. Neutrino democracy, fermion mass hier-
3089 archies, and proton decay from 5d su(5). *Phys. Rev. D*, 67:075007, Apr 2003.
- 3090 [111] Sigma-Aldrich, P.O. Box 14508, St. Louis, MO 63178 USA.
- 3091 [112] R. K. Teague and C. J. Pings. Refractive index and the lorentz–lorenz function
3092 for gaseous and liquid argon, including a study of the coexistence curve near the
3093 critical state. *The Journal of Chemical Physics*, 48(11):4973–4984, jun 1968.
- 3094 [113] J. Thomas and D. A. Imel. Recombination of electron-ion pairs in liquid argon
3095 and liquid xenon. *Phys. Rev. A*, 36:614–616, Jul 1987.
- 3096 [114] D.R.O. Morrison N. Rivoire V. Flaminio, W.G. Moorhead. Compilation of
3097 Cross Sections I: π^+ and π^- Induced Reactions. *CERN-HERA*, pages 83–01,
3098 1983.
- 3099 [115] D.R.O. Morrison N. Rivoire V. Flaminio, W.G. Moorhead. Compilation of
3100 Cross Sections II: K^+ and K^- Induced Reactions. *CERN-HERA*, pages 83–02,
3101 1983.
- 3102 [116] Hermann Weyl. Gravitation and the electron. *Proceedings of the National
3103 Academy of Sciences of the United States of America*, 15(4):323–334, 1929.
- 3104 [117] Colin et al Wilkin. A comparison of pi+ and pi- total cross-sections of light
3105 nuclei near the 3-3 resonance. *Nucl. Phys.*, B62:61–85, 1973.
- 3106 [118] D. H. Wright and M. H. Kelsey. The Geant4 Bertini Cascade. *Nucl. Instrum.
3107 Meth.*, A804:175–188, 2015.

- 3108 [119] C. S. Wu, E. Ambler, R. W. Hayward, D. D. Hoppes, and R. P. Hudson.
3109 Experimental test of parity conservation in beta decay. *Phys. Rev.*, 105:1413–
3110 1415, Feb 1957.
- 3111 [120] N Yahlali, L M P Fernandes, K Gonzlez, A N C Garcia, and A Soriano. Imaging
3112 with sipms in noble-gas detectors. *Journal of Instrumentation*, 8(01):C01003,
3113 2013.
- 3114 [121] T. Yanagida. Horizontal symmetry and masses of neutrinos. *Progress of Theo-*
3115 *retical Physics*, 64(3):1103–1105, sep 1980.